A Temporal Deep Learning Approach to Bedfast and Floating Thermokarst Lake Ice Mapping using SAR imagery: Old Crow Flats, Yukon, Canada

by

Maria Shaposhnikova

A thesis
presented to the University of Waterloo
in fulfillment of the
thesis requirement for the degree of
Masters of Science
in
Geography

Waterloo, Ontario, Canada, 2021

© Maria Shaposhnikova 2021

Author's Declaration

I hereby declare that I am the sole author of this thesis. This is a true copy of the thesis, including any required final revisions, as accepted by my examiners.

I understand that my thesis may be made electronically available to the public.

Abstract

Lake ice is a fundamental part of the freshwater processes in cold regions and a sensitive indicator of climate change. As such, in light of the recent climate warming, monitoring of lake ice in arctic and sub-arctic regions is becoming increasingly important. Many shallow arctic lakes and ponds of thermokarst origin freeze to bed in the winter months maintaining the underlying permafrost in its frozen state. However, as air temperatures rise and precipitation increases, less lakes are expected to develop bedfast ice. In fact, a consistent decrease in maximum ice thickness has been observed over the past decades.

Synthetic aperture radar (SAR) offers a unique opportunity to monitor lake ice regimes remotely. Taking advantage of the growing temporal resolution of microwave remote sensing, we proposed applying a temporal deep learning approach to lake ice regime mapping. We employed a combination of Sentinel 1, ERS 1/2, and RADARSAT 1 SAR imagery for the Old Crow Flats (OCF), Yukon, Canada to create an extensive annotated dataset of SAR time-series labeled as either bedfast ice, floating ice, or land, used to train a temporal convolutional neural network (TempCNN). The trained TempCNN, in turn, allowed to automatically map lake ice regimes over a 29-year period (1993-2021). The classified maps aligned well with the available field measurements and Canadian Lake Ice Model (CLIMo) simulated ice thickness. Reaching a mean overall classification accuracy of 95.05%, the temporal deep learning approach was found promising for automated lake ice regime classification. Change detection tools were utilized to determine lake ice regime changes in the OCF over the past 29 years. In the view of significant annual variability, no consistent transition towards more floating lake ice was observed. On the contrary, the overall change indicated an extensive transition to bedfast ice caused by a growing number of catastrophic drainages within the examined time period brought on by climate warming and thermokarst processes.

Acknowledgements

I would like to express my sincere gratitude to my thesis advisor Professor Claude Duguay for providing me with an opportunity to do this research, for his help and advice.

I would like to acknowledge Richard Kelly and Wesley Van Wychen for their participation on my thesis committee.

Lastly, I would like to thank my husband and my family for their endless support and encouragement, and Jenn Hagerman for being a wonderful friend.

Table of Contents

List of Figures vii

List of Tables xi

1 Introduction 1

1.1 Motivation . . . 1

1.2 Research Objectives . . . 3

1.3 Thesis organization . . . 4

2 Background 5

2.1 Thermokarst . . . 5

2.2 Bedfast and floating ice mapping from radar imagery . . . 8

2.2.1 Evolution of radar backscatter . . . 8

2.2.2 Methods for mapping bedfast and floating ice . . . 12

2.3 Deep Learning . . . 17

2.4 Time trends of thermokarst lake ice regimes . . . 22

3 Study Area 25

4 Methodology 29

4.1 SAR imagery and processing . . . 29

4.2 Annotated dataset creation . . . 33

4.3 Temporal Convolutional Neural Network . . . 39
4.3.1 TempCNN . . . 39
4.3.2 TempCNN architecture . . . 40
4.3.3 TempCNN architecture selection . . . 42
4.3.4 TempCNN training and testing . . . 46
4.4 Creation of ice regime maps using TempCNN . . . 47
4.5 Accuracy assessment and comparison with lake ice model simulations . . . 48
4.6 Ice regime change analysis . . . 49

5 Results and Discussion **51**
5.1 TempCNN classification accuracy assessment . . . 51
5.2 Assessment against field observations and lake ice thickness simulations . . . 57
5.3 Ice regime change analysis . . . 66

6 Conclusion **75**
6.1 Concluding remarks . . . 75
6.2 Recommendations for future work . . . 77

References **80**

Appendix **97**

A Supplementary material **98**
A.1 List of all the SAR scenes used in this thesis . . . 98
A.2 All the maps created using TempCNN . . . 134

List of Figures

2.1 General lake ice backscatter (VV, a similar pattern is observed for HH) lifecycle from early October to late April in stages. If by the end of the cycle ice remains floating it is refered to as floating, if the ice grounds, it is refered to as bedfast. Each of the ice regimes is illustrated by an example of one pixel from the study area traced through time. 10

3.1 Old Crow Flats, Yukon, Canada. The background image is an RGB Landsat 8 of May 31, 2020. Most lakes are still ice covered at this time of the year. 28

4.1 An example of an early fall scene used for identifying lake outlines during the labeling process (October 14, 2017, Sentinel 1). The greyscale corresponds to sigma nought (db) values. Lake surfaces appear black, while the surrounding land is grey. 35

4.2 HH and VV seasonal cycles for RADARSAT 1(HH), ERS (VV), and Sentinel 1 by class (each sensor is represented by a sample of 6 randomly selected pixels per graph). 37

4.3 Comparison of the three classes by sensor: Sentinel 1, ERS1/2, RADARSAT 1 (each class is represented by a sample of 100 randomly selected pixels per graph). 38

4.4 The four graphs illustrate application of 1-dimensional (1D) filters to time-series that can be used by convolutional layers of a TempCNN for extraction of temporal features. The red line represents original time-series, while the blue line denotes the filtered time-series. Top-left: simple general curve transformed by a gradient filter; top-right: a more complex curve that resembles floating ice transformed by a gradient filter; bottom-left: a curve resembling floating ice transformed by a low-pass filter; bottom-right: a curve resembling floating ice transformed by a high-pass filter. 41

4.5 Structure of the trained TempCNN. The left portion represents an image stack that serves as an input to the neural network; the middle portion illustrates the composition of the TempCNN including layers, activation functions, and mechanisms for overcoming overfitting; the right portion represents the output created by the neural network that consists of a three-class (floating ice; bedfast ice; land) map, and three probability maps (one for each class). 43

4.6 Temporal cross validation. 64 HP - 64 units convolutional layers filtered using Hodrick-Prescott filter, 64 long - original dataset trained for 45 epochs each (no early stopping). 45

5.1 TempCNN classification output for Sentinel 1, March 2021, OCF, Yukon Canada. 53

5.2 TempCNN classification output for RADARSAT 1, March 2002, OCF, Yukon Canada. 54

5.3 TempCNN classification output for ERS, March 1993, OCF, Yukon Canada. 55

5.4 Matching TempCNN output with lake depths collected in 2000. Horizontal lines indicate CLIMo ice thickness predictions for taiga (0.72 m) and tundra (1.21 m) environments. RADARSAT 1 SAR time-series were used for ice regime classification. 59

5.5 CLIMo simulated ice thickness for OCF (top: simulation of taiga environment; bottom: simulation of tundra environment). 64

5.6 Husky Lake TempCNN predicted ice regime (1993-2021). 65

5.7 Husky Lake water level changes visible on Landsat imagery between summers of 2004 and 2005. 66

5.8 Change detection between 1993 (ERS) and 2021 (Sentinel 1) ice regime maps. Dark blue represents transition from floating to bedfast ice regime; light blue shows transition from bedfast to floating ice regime; green stands for transition from floating ice regime to land. The inset map in the top left corner is a zoomed in view of the area highlighted as a green rectangle on the main map; top right corner - dark blue rectangle; bottom right corner – light blue rectangle. 68

5.9 Netro Lake TempCNN predicted ice regime (1993-2021). 69

5.10 Zelma Lake TempCNN predicted ice regime (1993-2021). 70

5.11 Lake #1: Transition from floating to bedfast ice regime between 2010 and 2018 (left). Water level changes visible on Landsat imagery between summers of 2016 (center) and 2017 (right). 71

5.12 Lake #2: Transition from floating to bedfast ice regime between 2010 and 2018 (left). Water level changes visible on Landsat imagery between summers of 2017 (center) and 2018 (right). 71

5.13 Change detection analysis (top: ice regime transitions; bottom: water and land transitions). The height of each bar in both charts represents the area in km^2 that transitioned between the two ice regimes (top chart) and floating ice regime and land (bottom chart) between two consecutive years of the dataset. 74

A.1 TempCNN classication output for Sentinel 1, March 2021, OCF, Yukon Canada. 135

A.2 TempCNN classication output for Sentinel 1, March 2020, OCF, Yukon Canada. 135

A.3 TempCNN classication output for Sentinel 1, March 2019, OCF, Yukon Canada. 136

A.4 TempCNN classication output for Sentinel 1, March 2018, OCF, Yukon Canada. 136

A.5 TempCNN classication output for ERS, March 2010, OCF, Yukon Canada. 137

A.6 TempCNN classication output for ERS, March 2009, OCF, Yukon Canada. 137

A.7 TempCNN classication output for RADARSAT 1, March 2008, OCF, Yukon Canada. 138

A.8 TempCNN classication output for RADARSAT 1, March 2006, OCF, Yukon Canada. 138

A.9 TempCNN classication output for RADARSAT 1, March 2005, OCF, Yukon Canada. 139

A.10 TempCNN classication output for RADARSAT 1, March 2004, OCF, Yukon Canada. 139

A.11 TempCNN classication output for RADARSAT 1, March 2003, OCF, Yukon Canada. 140

A.12 TempCNN classication output for RADARSAT 1, March 2002, OCF, Yukon Canada. 140
A.13 TempCNN classication output for RADARSAT 1, March 2001, OCF, Yukon Canada. 141
A.14 TempCNN classication output for RADARSAT 1, March 2000, OCF, Yukon Canada. 141
A.15 TempCNN classication output for ERS, March 1996, OCF, Yukon Canada. 142
A.16 TempCNN classication output for ERS, March 1995, OCF, Yukon Canada. 142
A.17 TempCNN classication output for ERS, March 1994, OCF, Yukon Canada. 143
A.18 TempCNN classication output for ERS, March 1993, OCF, Yukon Canada. 143

List of Tables

2.1 Floating and bedfast ice mapping methods: Threshold-based algorithms (Pol. stands for Polarization; I.A. stands for Incidence Angle). 14

2.2 Floating and bedfast ice mapping methods: Region-based classification (Pol. stands for Polarization; I.A. stands for Incidence Angle). 15

2.3 Floating and bedfast ice mapping methods: Special approaches (Pol. stands for Polarization; I.A. stands for Incidence Angle). 16

4.1 Data used in the project (I.A. stands for Incidence Angle). 32

4.2 Date of labeling and number of scenes by year (year (#of scenes), where full indicates # of full coverage scenes of OCF). 33

4.3 Mean, median, IQR. 44

5.1 TempCNN overall classification accuracy (15 experiments). 53

5.2 Field data collected in April 2021 on a small lake located beside the drained basin of Zelma Lake. 61

5.3 Field data collection in the OCF in April 2009. 62

5.4 CLIMo simulated ice thickness for OCF taiga: maximum ice thickness and March 13 ice thickness. Ice thickness value highlighted in red was used for 2000 field data analysis. 63

5.5 CLIMo simulated ice thickness for OCF tundra: maximum ice thickness and March 13 ice thickness. Years highlighted in red had floating ice according to TempCNN. 65

5.6 Inter-annual change in regimes. 73

Chapter 1

Introduction

1.1 Motivation

Lakes are one of the 54 Essential Climate Variables (ECV), as defined by The Global Climate Observing System (GCOS)(Belward et al., 2016). ECVs are a group of interrelated earth and atmospheric parameters which are essential for the understanding and characterization of the current climate and its evolution over time. Each ECV has a number of products associated with it, which have to be continuously monitored in order to have a full grasp of the ECV conditions. Lake ice thickness and ice cover are included in the list of the Lakes ECV products. Sensitivity to air temperatures makes lake ice a robust indicator of climate change (Brown and Duguay, 2010). The spatial extent and duration of ice cover play a significant role in lake surface-atmosphere interactions, which is reflected in regional weather and climate (thermal moderation, lake-induced precipitation) (Rouse et al., 2008).

In the light of the recent climate warming, monitoring of lake ice in arctic and sub-arctic regions is becoming increasingly important. Many shallow arctic lakes and ponds

of thermokarst origin freeze to bed in the winter months with ice thickening, this way maintaining the underlying permafrost in its frozen state. However, with climate warming, less lakes are expected to develop bedfast ice. In fact, a consistent decrease in maximum ice thickness has been observed over the past decades, in turn leading to fewer lakes developing bedfast ice (Surdu et al., 2014). Prolonged periods of liquid water presence may initiate formation of taliks and promote permafrost degradation in the underlying sediment (Arp et al., 2011). The storage of carbon contained in permafrost is estimated to be twice as large as the carbon currently present in the atmosphere in the form of greenhouse gases (Hugelius et al., 2014). Permafrost degradation results in the release of carbon dioxide and methane, potent greenhouse gases, into the atmosphere. Bedfast and floating ice mapping is not only important for emission studies, but also ecological studies, bathymetric mapping, and the determination of freshwater availability for the construction of ice roads (Duguay and Lafleur, 2003; Jeffries et al., 1996; Pointner et al., 2019). Moreover, for northern communities lake ice information can be crucial for determining whether a specific lake provides overwintering habitat for fish and whether liquid water is available for withdrawal (Brown et al., 2010; Tsui et al., 2019).

Given the significance of accurate bedfast lake ice mapping in regions underlain by permafrost, there is a growing need for robust automated techniques to be developed. Owing to the vast number of shallow lakes occupying permafrost regions, satellite remote sensing plays a key role in monitoring the evolution of ice cover. A variety of techniques have been proposed for the mapping of bedfast and floating ice from synthetic aperture radar (SAR). However, none of the existing methods have attempted classifying lake ice regimes from SAR imagery by identifying the best nonlinear function to describe lake ice

backscatter evolution. In this thesis, a classification technique based on the temporal deep learning is proposed to automatically extract useful features from SAR time-series and to create high-quality ice maps. The proposed technique is then applied to perform change detection analysis of the ice regimes of shallow lakes in Old Crow Flats, Yukon, Canada - a wetland of international importance according to the Ramsar Convention held in 1982 (Lynch-Stewart and Associates, 2008).

1.2 Research Objectives

The objectives of this thesis are as follows:

1. To create of an extensive labeled dataset of lake ice regime time-series, which includes three classes: floating ice, bedfast ice, and land. An annotated dataset is necessary to train a deep learning model able to perform automatic classification of SAR image time-series.

2. To apply a temporal deep learning approach (TempCNN) to thermokarst lake ice mapping from SAR imagery. Temporal deep learning has never previously been applied to lake ice mapping from SAR. This method offers an end-to-end classification framework that incorporates automatic feature extraction and classification. The temporal component allows to leverage the distinct life-cycles of lake ice and the surrounding ground backscatter. Therefore, use of a lake mask is not required prior to time-series classification. This is especially beneficial due to the dynamic nature of thermokarst lakes.

3. To generate ice-regime maps for 18 years of data from 1993-2021, based on SAR data availability, which allows to perform a 29-year change detection analysis of lake ice regimes in Old Crow Flats, Yukon, Canada.

1.3 Thesis organization

This thesis consists of six chapters. Chapter 2 contains background information on thermokarst lakes and lake ice, a review of state-of-the-art approaches to floating and bedfast ice mapping from SAR, an overview of uses and methods of temporal deep learning in remote sensing, and a summary of lake ice regime trends observed in sub-Arctic environments. Chapter 3 describes the Old Crow Flats, Yukon, Canada chosen as the study area. Chapter 4 presents the methodology developed in this thesis including the temporal approach used for mapping floating and bedfast ice from SAR using TempCNN. Chapter 5 contains results and their discussion. Finally, Chapter 6 summarizes the key findings of this work identifying limitations and directions for future research.

Chapter 2

Background

2.1 Thermokarst

In the Arctic, the impact of climate warming is especially pronounced owing to the positive feedbacks triggered by rising air temperatures and precipitation (Meredith et al., 2019). Permafrost, or perennially cryotic ground, a significant component of the Arctic cryosphere, is expected to experience widespread thawing by the end of the century initiating strong carbon feedbacks (van Huissteden, 2020). Permafrost soils stretch as far south as the -1°C isotherm and underlay about 19-25% of the Northern Hemisphere (Gruber, 2012). Permafrost is traditionally defined as soil or rock that maintains below 0°C temperature for at least two consecutive years, distinguishing it from seasonally frozen ground, termed active layer (French, 2018). Moving from north to south, along with the thickness of the active layer, a gradient in permafrost zones from continuous (>90% of land is underlain

by permafrost soils), discontinuous (50-90%), sporadic (10-50%), to isolated (<10%) is observed (van Huissteden, 2020). Permafrost soils are rich in organic matter. Permafrost thaw initiates the decomposition of organic matter in the soil by soil fauna and bacteria which results in release of carbon-dioxide and methane - potent greenhouse gases (Hugelius et al., 2014). Although the extent and rate of permafrost warming is largely unknown, ground observations of active layer thickness and temperature as well as permafrost temperatures measured in deep boreholes reveal unambiguous warming trends (van Huissteden, 2020). Being a sub-surface phenomenon, permafrost state is challenging to monitor. Nonetheless, thermokarst landscapes can serve as indicators of the underlying permafrost dynamics.

The term thermokarst can represent both a process and a landform. As a process, it corresponds to thawing of the permanently frozen sediments or melting of ice wedges as a result of the disturbed thermal equilibrium (Jones et al., 2011). Thermokarst lakes are one of the most wide-spread forms of thermokarst common in tundra and boreal lowlands of northern Canada, Alaska, and Russia (Kokelj and Jorgenson, 2013). Thermokarst lakes are extremely dynamic in nature. Being a part of the positive feedback loop, their presence in permafrost regions promotes further degradation of the frozen sediments directly below and adjacent to the lake-bed forming taliks (Brewer, 1958). After the initial permafrost thaw, ground subsidence and lake formation, thermokarst lakes tend to expand laterally by the means of thermal and mechanical erosion. The final stage of the thermokarst lake life-cycle is their drainage, which can occur through a variety of mechanisms, such as shoreline breaching or subsurface infiltration through an open talik among others (Bouchard et al., 2017). A study by Lindgren *et al.* (2016) demonstrates a direct link between permafrost thaw at thermokarst lake margins and the release of carbon stored in permafrost. While

it has been shown that thermokarst lake formation and expansion facilitate the release of organic carbon, drained lake basins, on the other hand, promote peat accumulation which leads to organic carbon sequestration (Jones et al., 2011). Hence, monitoring and quantifying thermokarst lake dynamics is critical for understanding changes in permafrost stability and ecosystem fluxes.

Numerous studies have investigated thermokarst lake dynamics (Jorgenson and Grosse, 2016; Nitze et al., 2017; Swanson, 2019; Wang et al., 2018). For instance, Nitze *et al.* (2017) recently examined decadal scale changes in thermokarst lake surface area and found that while northern Alaska experienced a net loss of lake area due to thermokarst lake expansion being counteracted by catastrophic lake drainages, Central Yakutia, Russia has experienced a remarkable expansion. Lake ice is a significant component of the freshwater processes in cold regions. Moreover, the spatial extent, duration, and thickness of lake ice are highly sensitive to climate change (Brown and Duguay, 2010). Arp *et al.* (2016) indicate a lake ice thinning trend of 0.15 m per decade observed in thermokarst regions, such as northern Alaska, in response to climate warming. The authors also point out that thermokarst lakes whose depth is close to the maximum ice thickness are most sensitive to climate warming and subsequently have the most impact on the underlying permafrost. The lake ice research community has focused its attention on documenting temporal trends and developing observation methods of the following parameters: ice cover concentration, ice extent, ice phenology, ice types, ice thickness and snow on ice, ice surface temperature, and bedfast and floating ice cover (Duguay et al., 2015). The focus of this thesis is on bedfast and floating ice mapping and ice regime changes over time, discussed in the next subsection and subsection 2.4, respectively.

2.2 Bedfast and floating ice mapping from radar imagery

2.2.1 Evolution of radar backscatter

The potential of microwave remote sensing for bedfast and floating ice mapping was first introduced in 1975. Sellmann *et al.* (1975) noticed a characteristic dark and bright pattern of ice on shallow lakes of the Alaskan coastal plain when observing them from X-band Side Looking Airborne Radar (SLAR) data. Smaller lakes often appeared dark, while larger lakes had bright centers and dark fringes. Based on the field knowledge of lake depths and sites of winter water withdrawal, the observed pattern was believed to correspond to floating ice - bright, and bedfast ice- dark. Next followed a multitude of studies that observed the same pattern in X (8-12 GHz), L (0.5-1.5 GHz), and C (4-8 GHz) bands spaceborne synthetic aperture radar (SAR) imagery starting from studies involving C-band VV polarization ERS-1 (European Remote-Sensing Satellite-1) up to the most recent work done with Sentinel-1 and RADARSAT-2 (C-band, mostly at VV and HH polarizations). In fact, the dielectric properties of water and ice display a high contrast in an electromagnetic window between 5-17 GHz making this range sensitive to the presence of liquid water under the ice (Gunn et al., 2015a). As such, SAR active microwave remote sensors are not only able to penetrate clouds and operate independently of solar illumination, which becomes especially relevant in polar regions, but also benefit from distinct backscatter patterns for floating and bedfast ice. Floating ice is characterized by a high backscatter response, originally explained by the double bounce phenomenon caused by the presence of tubular bubbles in the ice (Jeffries et al., 2005b). In addition, as indicated by Grunblatt

and Atwood (2014), the ice-water interface is marked by a high dielectric discontinuity, in contrast to bedfast ice which presents a very dark SAR signature. The low dielectric contrast between the ice and the underlying sediments results in signal transmission or absorption by lakebeds (Grunblatt and Atwood, 2014; Jeffries et al., 2005b). The temporal evolution of backscatter from open water in the fall to the ice break-up in the spring can be summarized into the following five stages (Duguay and Lafleur, 2003):

1. Although open water generally appears dark in SAR imagery due to the specular reflection away from the sensor, in Arctic and sub-Arctic regions lake surfaces tend to be roughened by high winds resulting in high backscatter. Therefore, as thin ice forms over the lake in early November it creates a mirror-like surface accompanied by a drop in backscatter.

2. By mid-December as ice thickens and forms tubular bubbles the backscatter increases creating a bright signature, particularly in shallower areas of lakes.

3. By mid-January ice has grown sufficiently thick to reach the bed in shallower areas causing signal absorption by the frozen sediments and, therefore, resulting in a dark signature (low backscatter).

4. By late March most shallow lakes are covered by bedfast ice and appear dark in SAR imagery. Late March to late April are generally considered to be the months of maximum ice thickness in Arctic and sub-Arctic regions.

5. From May to early June, as the air temperatures rise above zero, the break-up period begins. During this period a variety of tones are observed. As bedfast ice transitions

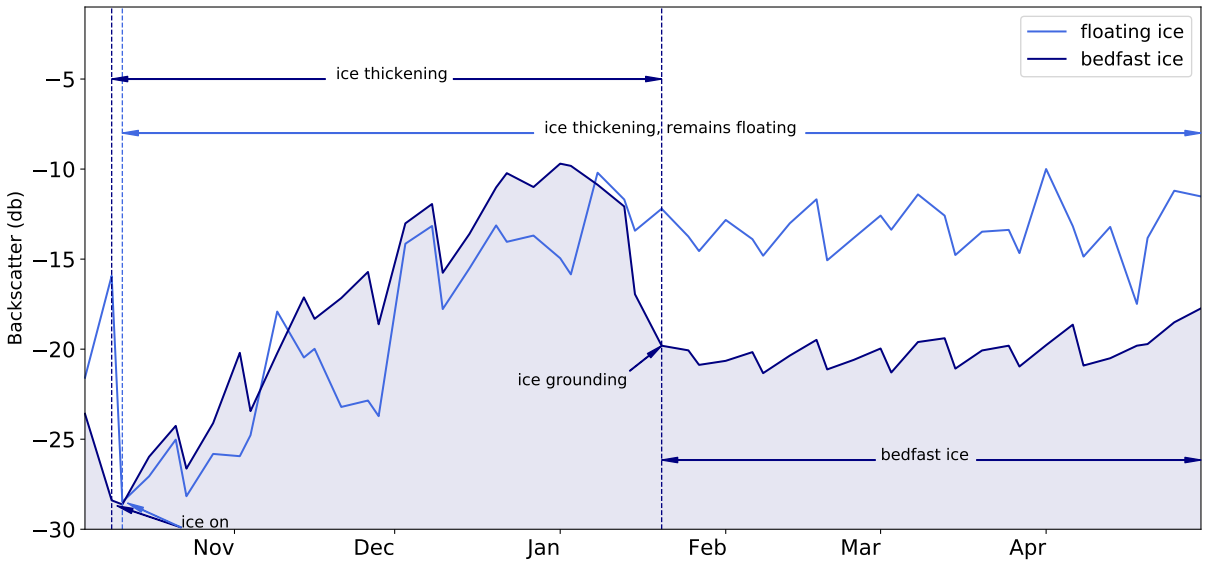


Figure 2.1: General lake ice backscatter (VV, a similar pattern is observed for HH) lifecycle from early October to late April in stages. If by the end of the cycle ice remains floating it is refered to as floating, if the ice grounds, it is refered to as bedfast. Each of the ice regimes is illustrated by an example of one pixel from the study area traced through time.

to floating ice at the lake fringes the backscatter increases, while ice covered by wet snow or pools of standing water appears dark due to signal absorption and reflection, respectively. Finally, ice-free areas appear dark, due to specular reflection caused by low or absent winds.

Owing to the focus of this thesis on the months of maximum ice thickness, Figure 2.1 below illustrates the lifecycle of floating and bedfast ice from early October to late April including stages 1-4 discussed above.

However, the distinction between floating and bedfast ice at each given time is not always clear-cut. Multiple suggestions have been made with regard to the potential reasons

for the appearance of darker backscatter signatures in areas of lakes corresponding to floating ice. Although uncommon in permafrost regions, larger lakes that exceed the depth of 4 m, such as Teshekpuk Lake on the North Slope of Alaska, often demonstrate a darker signature in their deepest sections. In the study on the impact of lake size on the accuracy of bedfast and floating ice classification, Pointner *et al.* (2019) suggest that the darker signature in the deeper sections of lakes could be caused by such phenomena as cracks in the ice and presence of small patches of thin ice. However, it is still indicated that the observed patterns remain largely unexplained due to the lack of field observations coincident with SAR image acquisitions. Additionally, as mentioned by Grunblatt and Atwood (2014), brackish lakes tend to produce lower backscatter even in the presence of liquid water underneath the ice. Moreover, the presence of wet snow during brief periods of winter melt results in reduced backscatter intensities of floating ice (Duguay et al., 2002). Finally, incidence angle of the instrument is an important parameter that has to be taken into account when interpreting bedfast and floating ice backscatter (Duguay et al., 2002).

Floating and bedfast ice mapping has a variety of applications, including climate monitoring (Arp et al., 2012), permafrost studies (Arp et al., 2011), bathymetric mapping (Duguay and Lafleur, 2003; Kozlenko and Jeffries, 2000), overwintering fish habitat (Brown et al., 2010), and winter water withdrawal (Hirose et al., 2008). Traditionally, bedfast and floating ice has been mapped from spaceborne C-band SAR. However, a number of studies also resorted to X- and L-band imagery (Antonova et al., 2016; Engram et al., 2013; Jones et al., 2013; Wang et al., 2018).

2.2.2 Methods for mapping bedfast and floating ice

A variety of methods have been proposed to distinguish between bedfast and floating ice based on SAR backscatter, namely threshold-based classification (Bartsch et al., 2017; Brown et al., 2010; Duguay et al., 2002; Duguay and Wang, 2019; Engram et al., 2018; Hirose et al., 2008; Kozlenko and Jeffries, 2000; Wakabayashi and Motohashi, 2018), supervised and unsupervised classification (Grunblatt and Atwood, 2014), region-based classification (Pointner et al., 2019; Surdu et al., 2014), as well as one unique method based on data mining (Tsui et al., 2019).

Thresholding is by far the most widely used method. For instance, Bartsh *et al.* (2017) using ENVISAT ASAR C-band imagery produced circumpolar maps of bedfast and floating ice for a single winter season based on a threshold function fitted to data collected from the Yamal Peninsula, Russia. The utilized threshold function accounted for incidence angle variability and was successfully applied to two million Arctic lakes. Engram *et al.* (2018) reported a 93% overall accuracy achieved through an interactive thresholding algorithm applied to a 25-year time-series of six generations of C-band SAR imagery from ERS-1 to Sentinel-1. The developed algorithm identified a unique threshold for each scene avoiding errors resulting from variations in ice and weather conditions as well as alleviating the need for incidence angle normalization. Finally, Duguay and Wang (2019) compared thresholding with correction for incidence angle effects to two unsupervised classification techniques (K-means and Iterative Region Growing Using Semantics) and found that thresholding outperforms the other two algorithms, reaching an overall accuracy of 92.56%, and generalizes the best to new geographical regions. In spite of the fact that

both thresholding and K-means provided a reasonable classification of bedfast and floating ice for small shallow lakes, both algorithms resulted in overestimation of bedfast ice in deep lakes, such as Teshekpuk Lake, Alaska. With the aim of improving classification results for deeper lakes, Pointner *et al.* (2019) compared the threshold method to two novel methods based on pixel connectivity: flood-fill and watershed methods. Both methods took topography and the fact that ice grounding generally takes place in the shelf regions into account. Although visual assessment suggested an improved performance, no definitive conclusion was reached due to the lack of ground truth data. The summary of works that used a variety of bedfast and floating ice classification methods can be found in Tables 1-4.

To the best of our knowledge, the only study that exploited the temporal evolution of backscatter is Tsui *et al.* (2019) who adopted a data mining approach called dynamic time warping (DTW). DTW compares backscatter time-series based on their shape. Tsui *et al.* (2019) assembled a time-series of 53 RADARSAT-2 C-band scenes collected between November and June. Then, based on ground penetrating radar field measurements, 13 bedfast ice reference time-series were identified. All the unclassified time-series were compared to the reference ones using the DTW similarity measure. The performance of the approach was assessed based on 37 field measurements resulting in an overall accuracy of 89.1%. However, approaches that use temporal similarity measures, such as DTW, are very computationally costly as they require scanning the training set in its entirety in order to make a decision for every test instance (Pelletier et al., 2019b). Therefore, in this project, we propose adopting a deep learning end-to-end framework for bedfast and floating ice classification that exploits the temporal dimension of the C-band SAR. The potential of the deep learning approach and the existing literature is explored in the next

Reference	Study Area	Sensor (band)	Pol.	I.A.	Method	Drop in Backscatter/Threshold/Accuracy
Kozlenko and Jeffries, 2000	North Slope of Alaska	ERS-1 (C)	VV		thresholding and supervised maximum likelihood classification	threshold = (spatially averaged backscatter (sab) of grounded ice + sab of floating ice)/2
Duguay et al., 2002	Churchill, Manitoba, Canada	RADARSAT-1 (C)	HH	20-49°	thresholding	Arctic drop: 10dB 7dB sub-Arctic drop: 7dB
Duguay and Lafleur, 2003	Hudson Bay Lowlands Manitoba, Canada	ERS-1 (C)	VV	20.1-25.9°	thresholding	Thermokarst drop: 9-10dB Bedrock drop: 6dB
Hirose et al., 2008	Mackenzie River Delta, NWT, Canada	RADARSAT-1 (C)	HH	37-42°	manual tracing of the boundary by visual analysis of tone change	n/a
Brown et al., 2010	Sagavanirktok River, Alaska	ERS-1/2 ENVISAT (C)	VV, VH, HH, HV	19.2-31.4°	thresholding	threshold: HH, VV: -10dB; HV, VH: -19dB pixel accuracy: 69% 100% of under ice pools of water identified from SAR
Engram et al., 2013	Northern Seward Peninsula and Arctic Coastal Plain, Alaska	ALOS PALSAR, JERS-1 (L) ERS-1/2 (C)	HH (L) VV (C)	24-39° (L) 23° (C)	thresholding	L-band: G: -19dB F: -16 to -13dB (drop: 3-6dB) C-band: G: -15 to -14dB F: -6dB (drop: 8-9dB)
Jones et al., 2013	Fish Creek watershed, Arctic Coastal Plain, Alaska	TerraSAR-X (X) and GPR	HH	46°	thresholding	threshold: -12.3dB accuracy >90%
Grunblatt and Atwood, 2014	North Slope of Alaska	ERS-2 (C)	VV	23°	supervised isoclas clustering combined with thresholding	accuracy 89%
Antonova et al., 2016	Lena River Delta, Siberia	TerraSAR-X (X)	HH	31.6-31.7°	thresholding	drop: 1.8-8.3dB
Bartsch et al., 2017	Circumpolar mapping of grounded ice	ENVISAT ASAR (C)	HH	15-45°	thresholding	third degree polynomial threshold function based on backscatter and incidence angle drop: 7-8 dB
Engram et al., 2018	Arctic Coastal Plain: North Slope foothills and northern Seward Peninsula	ERS-1/2 RADARSAT-1 Envisat ASAR RADARSAT-2 Sentinel-1 (C)	VV, VH, HH, HV	15-49°	statistic-based interactive threshold classification method	threshold range: -9 to -19dB accuracy 93%
Wakabayashi and Motohashi, 2018	Barrow, Northern Alaska	Sentinel-1 (C)	HH	19-47°	thresholding	threshold: -14 dB.
Wang et al., 2018	Hudson Bay, northern Quebec, Canada	TerraSAR-X (X)	HH, VV		thresholding	threshold: -10.36dB accuracy: 99%
Duguay and Wang, 2019	Barrow and Teshekpuk Lake, Alaska; Mackenzie Delta, Canada; Kytalyk, Lena Delta and Yamal Peninsula, Russia	Sentinel-1 (C)			IRGS K-means thresholding	accuracy: thresholding 92.4%, IRGS 90.1%; K-means 85.3%

Table 2.1: Floating and bedfast ice mapping methods: Threshold-based algorithms (Pol. stands for Polarization; I.A. stands for Incidence Angle).

Reference	Study Area	Sensor (band)	Pol.	I.A.	Method	Drop in Backscatter/Threshold/Accuracy
Surdu et al., 2014	North Slope of Alaska	ERS-1/2 (C)	VV		IRGS	n/a
Pointner et al., 2019	Yamal Peninsula, Siberia	Sentinel-1 (C)	HH	20-45°	thresholding flood-fill watershed	improvement for deep areas

Table 2.2: Floating and bedfast ice mapping methods: Region-based classification (Pol. stands for Polarization; I.A. stands for Incidence Angle).

Reference	Study Area	Sensor (band)	Pol.	I.A.	Method	Drop in Backscatter/Threshold/Accuracy
Antonova et al., 2016	Lena River Delta, Siberia	TerraSAR-X (X)	HH	31.6-31.7°	interferometric coherence change	coherence increase with ice grounding
You et al., 2018	Qinghai-Tibet Plateau	GPR	n/a	n/a	thresholding	NAR threshold: >0.3 for floating; <0.19 for grounded . Floating range: 0.3-0.7; grounded 0.2
Tsui et al., 2019	Slave Geological Province and Central Mackenzie Valley Rigion, NWT, Canada	RADARSAT-2 (C)	HH	20-39.5°	dynamic time wrapping (DTW)	accuracy 89.1% (80% for grounded ice and 100% for floating ice)

Table 2.3: Floating and bedfast ice mapping methods: Special approaches (Pol. stands for Polarization; I.A. stands for Incidence Angle).

subsection.

2.3 Deep Learning

Machine learning (ML) techniques are used in a variety of fields, including identification of objects and patterns in images, speech recognition, machine vision, drug discovery, etc. (LeCun et al., 2015). Deep learning (DL), a set of techniques inspired by the human visual interpretation process and structured to imitate human nervous system, is quickly gaining popularity in a lot of machine learning applications. The main advantage of the DL approach over other ML techniques is its ability to independently learn important features from the provided "raw" data, rather than being fed features accurately designed by a human specialist. Neural network – the basis of DL – consists of multiple levels or layers. Each layer receives the information, transforms it to a higher level of abstraction using non-linear models and passes it to the next layer for further transformation (LeCun et al., 2015).

Remote sensing has been making use of ML techniques since early 1960s. Examples of early work include contributions of the Laboratory for Applications of Remote Sensing (Holloway and Mengersen, 2018; Landgrebe, 1986). The early accomplishments of the laboratory consisted in machine-implemented classification of multispectral data as early as 1966. Since then, ML has been widely applied for such tasks as image pre-processing, segmentation, and classification (Ma et al., 2019). Although, the remote-sensing community has been giving preference to ML methods such as Support Vector Machines (SVM) and Random Forest (RF), starting in 2014 the focus has largely shifted to DL methods (Chen

et al., 2014; Ma et al., 2019; Romero et al., 2016).

Based on the meta-analysis and review by Ma *et al.* (2019), convolutional neural network (CNN) is the most commonly used DL model for image analysis in remote sensing. As opposed to a simple neural network, CNNs are particularly strong at recognizing and extracting spatial features. CNNs consist of multiple convolutional layers alternated with pooling layers. Convolutional layers use filters that convolve across the image detecting spatial "patterns", for instance, edges, corners, or shapes. Each of the filters produces a feature map, which are then stacked (Wang et al., 2016). The deeper into the network, the more sophisticated are the filters and the patterns they can recognize. Pooling layers reduce the dimensions of the feature maps - a sliding window moves over the image replacing a "pool of values" with one single value, usually the maximum. The purpose of the convolutional and pooling layers is to extract features and reduce the number of parameters. The last stage of the CNN is a fully connected layer that performs the classification. After each iteration, the network backpropagates calculating the errors of the produced prediction based on the available labels and modifies the parameters of each layer to fit the data just a little bit better. To summarize the learning process, a CNN takes labeled data as input, learns from it, validating the accuracy of the prediction at each iteration and adjusting its parameters accordingly. Once the network is trained, it returns a prediction, when provided with unlabeled data.

In permafrost research there were early attempts to incorporate DL techniques (Leverington and Duguay, 1996; Leverington and Duguay, 1997). Since then, DL methods and computational power have evolved allowing for a more extensive use of DL for the investigation of

such permafrost landscapes as retrogressive thaw slumps (Huang et al., 2020), wetland ecosystems (Jiang et al., 2019), permafrost soil organic carbon content (Siewert, 2018), ice wedge polygons (Abolt, 2019), and others. However, studies involving DL for ice mapping are scarce. CNNs have shown impressive results in application to sea ice concentration mapping from SAR (Wang et al., 2016). To the best of our knowledge, only two studies made use of DL techniques for lake ice mapping: Tom *et al.* (2020) and Scott *et al.* (2020). Tom *et al.* (2020) proposed an automatic lake ice monitoring systems based on a CNN with Deeplabv3+ architecture which achieved an accuracy of 94.8-95.5%. Using VV and VH polarized Sentinel-1 SAR high-resolution imagery from three Alpine lakes in Switzerland the model was taught to output binary classification maps for the lake surface with a frozen and a non-frozen class. The lake shapes were extracted from Open Street Map. For the training purposes, Sentinel-1 SAR imagery was labeled through visual interpretation of webcam data and Sentinel-2 optical imagery. Moreover, to remedy the lack of an extensive labeled dataset, Tom *et al.* (2020) leveraged a transfer learning technique, which consists in using a pre-trained model, in this case a DL model trained on RGB data, and then fine-tuned on a small set of training SAR data. Scott *et al.* (2020) investigated retrieving high-quality ice/water observations from SAR imagery of the Laurentian Great Lakes (Lake Erie and Lake Ontario) using a CNN. The proposed approach focused on obtaining high-quality observations, rather than classifying the entire image. As such, areas where the classifier was uncertain were left unclassified. Using single-(HH) and dual-polarized (HH/HV) RADARSAT-2 imagery and experimenting with a classification probability threshold, the authors achieved classification accuracy ranging from 95% to 97% with an unclassified fraction between 20% and 53%.

Although, basic CNNs are powerful at analyzing spectral and spatial features, they fail to take advantage of the temporal aspect of satellite imagery. With the growing availability of high spatial, spectral, and temporal resolution remote sensing imagery, both optical and microwave, there is a growing interest among the remote sensing community to exploit the temporal dimension. Temporal evolution becomes important for the classification of landscapes and features that display distinct life cycles, such as vegetation types and agricultural fields with crops. In the computer science community, the sequential data is generally tackled using Recurrent Neural Networks (RNNs) facilitating such tasks as image captioning, sentiment analysis, language translation, and other (Ma et al., 2019). The state-of-the-art RNNs consist of multiple long short-term memory (LSTM) modules (Hochreiter and Schmidhuber, 1997) or Gated Recurrent Units (GRU) (Cho et al., 2014) that facilitate sequential processing of time-series where only relevant information is retained. The units are generally organized into a chain where the first unit receives the first input of the sequence, processes it using multiple neural networks, referred to as gates, passing to the next unit only relevant information. The next unit in the chain receives the second input of the sequence and processes it in the context of the information retained by the network from the first unit. During the training stage gates learn to retain relevant information and discard irrelevant information. This way, the most significant components are passed through the chain reaching the very last unit where they facilitate the final decision. Hence, as opposed to CNNs which have been shown to efficiently extract spatial features, RNNs are believed to offer a strong baseline for temporal analysis. Consequently, in the remote sensing context, RNNs have been found to be suitable for working with image time-series (Ienco et al., 2017; Minh et al., 2018; Sun et al., 2019).

RNNs were first adopted for land cover classification of multi-temporal optical imagery (Ienco et al., 2017; Sun et al., 2019). Later, RNNs started to be utilized for time-series classification of SAR imagery. For instance, studies by Ndikumana *et al.* (2018) and Minh *et al.* (2018) tested the utility of Sentinel-1 dual-polarization (VV+VH) SAR time-series and LSTM and GRU RNN models for summer crop and winter vegetation quality mapping, respectively. In both cases RNN was shown to outperform such ML approaches as K-means, RF, and SVM achieving an overall accuracy of 89-99%.

Recently, modified CNNs or combinations of CNNs and RNNs have shown an improved performance over simple RNNs. For example, Interdonato *et al.* (2019) developed a DuPLO - a DUal view Point deep Learning architecture for time-series land cover classification from Sentinel-2 optical imagery that includes a CNN and an RNN branch harnessing the strengths of both approaches. This approach achieved an accuracy of 83.72-96.36% exceeding the performance of standard ML methods. The study also found, analogously to Ienco *et al.* (2017), that feeding the features extracted by DuPLO to an RF algorithm performed even better than the DuPLO alone. Mauro *et al.* (2017) and Ji *et al.* (2018) achieved good results with 3D CNNs that incorporate spectral, spatial, and temporal dimensions for land cover and crop classification, respectively. Finally, studies by Pelletier *et al.* (2019a, 2019b) proposed a temporal 2D CNN (TempCNN) for land cover classification of Formosat-2 and Sentinel-2 time-series that incorporates spectral and temporal dimensions by performing temporal rather than spatial convolutions. These studies suggest that RNNs are unsuitable for large scale studies due to their high computational complexity. The TempCNN was shown to have higher accuracy than RF, SVM, and RNN and a much shorter training time.

Taking into consideration distinct life cycles of floating and bedfast ice, we hypothesize that classification accuracy as well as the floating ice misclassification in the deep portions of thermokarst lakes can be significantly improved by applying a temporal approach. In this thesis, the TempCNN architecture proposed by Pelletier *et al.* (2019) will be used as the basis and will be modified appropriately to fit the bedfast and floating ice classification. In the future, the work might be extended to include the spatial dimension by using a 3D CNN.

2.4 Time trends of thermokarst lake ice regimes

As mentioned earlier in this chapter, lake ice is a sensitive indicator of the changing climate. Warming predicted by numerical models by the end of the century is expected to shorten the ice season and reduce ice thickness (Brown and Duguay, 2011b). Thinning lake ice and longer open water season alter the heat storage and permafrost thaw rates, and trigger positive feedback loops that promote further warming (Arp et al., 2012). Therefore, monitoring of lake ice regimes and their changes over time is essential for more accurate bottom surface condition for climate modeling. A variety of different lake ice parameters can be monitored, such as ice-on/off dates (Geldsetzer et al., 2010), ice thickness (Duguay and Lafleur, 2003), or accumulated freezing index as an indicator of ice growth (Wakabayashi and Motohashi, 2018). However, in this thesis, we will focus on the bedfast and floating ice regimes making use of the extensive SAR imagery record that allows for change analysis starting as far back as fall of 1992.

The bedfast and floating ice regimes of Alaskan lakes have been studied extensively.

For instance, a study by Surdu *et al.* (2014) notes a clear trend towards a decreasing number of bedfast ice lakes. The study made use of a 20-year time-series of ERS-1/2 SAR imagery from 1991 to 2011 in a region that encompasses 402 lakes, near Barrow, North Slope of Alaska. The analysis of 79 SAR images between December and May revealed an overall decrease in the fraction of bedfast ice in April to be 22%. The maximum fraction of bedfast ice of 62% was observed in 1992, while in 2011 this fraction was only 26% for the same lakes. A study by Arp *et al.* (2012) reports significant variability of ice regime changes observed in inner and outer regions of Arctic Coastal Plain of northern Alaska (ACP). Analyzing SAR imagery between 2003-2011 and comparing it to radar-based maps of bedfast and floating ice from 1980 it was found that 16% of bedfast lakes shifted to floating ice regimes. This shift is attributed to a thinning ice trend of 1.5 cm per year since 1978. However, while in the outer ACP three lakes shifted from bedfast to a floating ice regime, in the inner ACP 27% of bedfast-ice lakes transitioned to floating ice. Engram *et al.* (2018) analyzed a 25-year time-series (1992-2016) of C-band SAR images in seven regions of northern Alaska and Seward Peninsula. The authors note that due to high inter-annual variability in floating ice extent no statistically significant trends could be observed. Nonetheless, one of the study areas, namely Fish Creek, exhibited strong trends towards bedfast ice regimes. Over the 25 years an increase of 4.2 % per decade was observed in the areas covered by floating ice. Moreover, the number of floating-ice lakes increased by 1.5% per decade.

Taking into consideration the variability observed between different study areas within northern Alaska, it is logical to assume that lake ice trends in other thermokarst lake areas of the Northern Hemisphere characterized by different climate and types of underlying

sediments will show different results. Hence, in this thesis, the Old Crow Flats (OCF), Yukon, Canada is selected as the focus area for ice regime change analysis and is discussed in detail in the Chapter 3.

Chapter 3

Study Area

While thermokarst lake ice regimes of northern Alaska, USA, Lena River Delta, Russia, and Hudson Bay, Canada (Antonova et al., 2016; Arp et al., 2011; Arp et al., 2012; Duguay and Wang, 2019; Engram et al., 2018; Mommertz, 2019; Surdu et al., 2014; Wang et al., 2018) have been studied by multiple researchers, ice regimes of Old Crow Flats, Yukon, Canada (OCF), remain largely unexplored. OCF is a wetland of international significance (Lynch-Stewart and Associates, 2008) rich in lakes of thermokarst origin and surrounded by mountains (Figure 3.1)(Lantz and Turner, 2015). The 4,300 km^2 area is covered by over 2500 flat-bottomed shallow lakes of 1 to 1.5 meters depth on average (Roy-Léveillée and Burn, 2010; Roy-Roy-Léveillée and Burn, 2015). OCF was submerged under a large glacial lake Old Crow during the Wisconsin stage (Irving and Cinq-Mars, 1974). The glacial lake drained catastrophically about 15,000 years ago leaving behind thick glaciolacustrine deposits and remnant lakes (Lauriol et al., 2009; Zazula et al., 2004). More lakes formed during early Holocene through thermokarst processes (Ovenden, 1985).

The northern part of the lowland is characterized by polygonal tundra, while subarctic boreal forest is found in the south (Roy-Léveillée, 2014). Lakes located in areas of taiga and tall shrubs have irregular shorelines and expand slowly due to vegetation roots holding the sediments, even following the shore subsidence caused by talik development, protecting them from wave action and ice push (Roy-Roy-Léveillée and Burn, 2015; Roy-Roy-Léveillée and Burn, 2017). Lakes located in polygonal tundra and low shrub areas, in contrast, are rectangular or triangular in shape. The absence of tall vegetation allows wave action and ice push to erode the shores and redistribute sediments creating a more even lake outline. These lakes are expanding rapidly and, in their majority, have a north-east – south-west orientation parallel to the dominant direction of the winds (Roy-Roy-Léveillée and Burn, 2015).

As indicated in Chapter 2, thermokarst lakes are extremely dynamic. After their formation initiated by permafrost thaw and ground subsidence, they continue their expansion until a drainage event occurs (Bouchard et al., 2017). Lake drainage might be followed by permafrost aggradation and formation of new lakes (Roy-Léveillée, 2014). As the climate warms and precipitation becomes more abundant in OCF, the frequency of lake drainage events is on the rise due to thermokarst activity (MacDonald et al., 2012). In fact, according to tree-ring climate records, the last few decades have been characterized by warming unseen in any other period of the past 300 years (Porter and Pisaric, 2011). Moreover, Vuntut Gwitchin First Nations, whose lifestyle is largely sustained by OCF, note significant changes in air temperatures, precipitation, and ice regimes in the past decades (Wolfe et al., 2011). Between 1951 and 2007, OCF has seen a decline in lake area of approximately 6,000 hectares, with the rate of lake drainage five times higher in

recent decades (Labrecque et al., 2009; Lantz and Turner, 2015). The overall decrease in the surface lake area is mainly attributed to the climate- and erosion-induced catastrophic lake drainages (e.g. Zelma and Netro Lakes) (Labrecque et al., 2009; Turner et al., 2010). A study of OCF drained lake basins vegetation indicates that willow stands and sedge swards quickly populate the drained lake area leading to increased snow capture which could increase ground temperatures leading to permafrost thaw (Lantz, 2017). Although older drained basins are generally covered by tussock grasses and dwarf shrubs, it is unclear whether the newly drained basins populated by willow thickets following the drainage event will transition to tundra vegetation, in the light of the warmer and wetter climate (Lantz, 2017). Despite the overall trend of decreasing water surface area, the majority of lakes are increasing in surface area and new ponds are forming due to rising air temperatures and increased precipitation, which bring on thinning of lake ice, deepening of active layers, permafrost thaw, and ground subsidence (Labrecque et al., 2009).

The climate of OCF is continental with cold winters (mean January temperature of -31.1°C) and warm summers (mean July temperature of 14.6°C)(Lantz and Turner, 2015). Continental climate and glaciolacustrine deposits make this area unique and different from other thermokarst lake zones. Although the area is underlain by continuous ice-rich permafrost, unlike other regions, such as Mackenzie River Delta, even shallow bedfast-ice lakes display mean lake-bed temperatures above zero due to high summer air temperatures (Roy-Léveillée, 2014). Lakes surrounded by boreal forest tend to accumulate more snow, and therefore, develop thinner ice, while tundra lakes have a thinner, denser snow which results in ice grounding (Duguay et al., 2003; Roy-Léveillée et al., 2014). To the best of our knowledge, bedfast and floating ice regime changes over time have not been analyzed

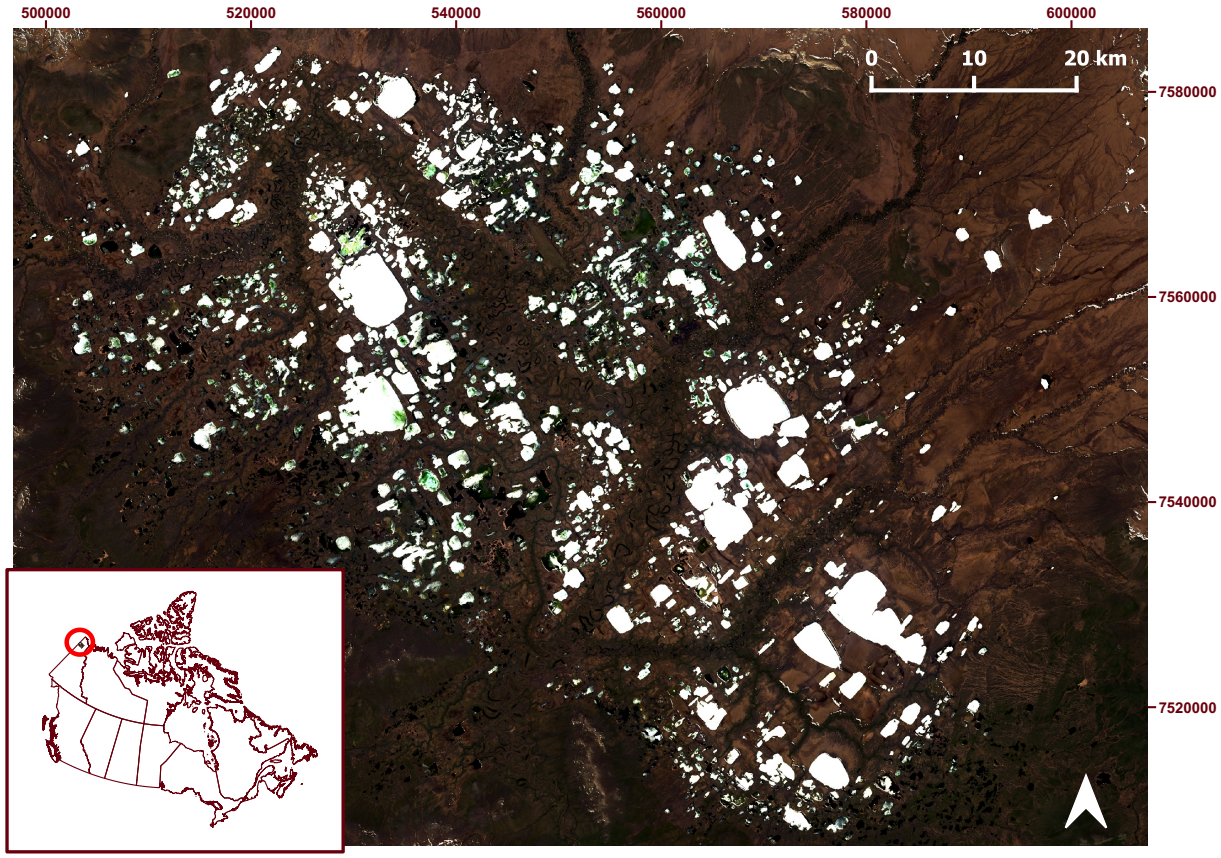


Figure 3.1: Old Crow Flats, Yukon, Canada. The background image is an RGB Landsat 8 of May 31, 2020. Most lakes are still ice covered at this time of the year.

for the region of OCF. In light of this region's unique climate and sediment type, active thermokarst processes, and climate-driven vegetation changes, such as shrubification of the tundra area (Wang et al., 2020), such analysis will make a valuable addition to the existing body of knowledge.

Chapter 4

Methodology

4.1 SAR imagery and processing

The SAR scenes cover the time period between 1992 to 2021. For each year the scenes were selected to cover the period from October to mid-March as densely as possible. Although ice reaches its maximum thickness in the OCF in late March or early April, mid-March was selected owing to the classification approach requirement for a consistent time-series end date throughout the entire time period. For all the later dates, beyond mid-March, one or more of the years had air temperatures above $0°C$ according to the weather station located in the village of Old Crow located approximately 40 km to the south of the OCF. Above $0°C$ temperatures lead to surface melt which, in turn, results in a decrease in radar backscatter interfering with the discrimination between floating and bedfast ice (Duguay and Lafleur, 2003). A dataset consisting of imagery from four C-band SAR space-borne

platforms was compiled: Sentinel 1 (S1) (VV polarization), ERS 1 and 2 (ERS1/2) (VV polarization), and RADARSAT 1 (R1) (HH polarization). The years covered by each instrument and their specifications are listed in Table 4.1. In total 18 years of SAR scenes across the 1992-2021 period were chosen as they offered a minimum of two scenes for each month throughout the ice season (555 scenes in total, see Appendix).

S1, ERS 1/2, and R1 imagery was obtained from Alaska Satellite Facility (ASF) - an online data repository which allows access to a wide range of SAR raw (level 0) and processed (levels 1 and 2) data. For S1, Radiometrically Terrain Corrected (RTC) level 2 products were downloaded from ASF. The RTC processing procedure calibrates the images removing topographic effects and corrects for geometric distortions ensuring precise geolocation. The process involves calibration, multi-looking to six looks, digital elevation model (DEM) matching, radiometric calibration to sigma nought amplitude, and speckle filtering. Images are subsequently terrain corrected and geocoded to WGS 84 / UTM zone 7N. The pixel size of the RTC product is determined by the resolution of the DEM utilized in the correction process. The DEM used by the ASF is the National Elevation Dataset (NED1), which has a native resolution of 1 arc second (approximately 30 m) yielding a 30-m final pixel size of SAR scenes.

The ERS1/2 and R1 data were available as level 1 products in a CEOS (Committee on Earth Observation Satellites) format. They were processed using MapReady Remote Sensing Tool Kit available from ASF. Analogously to the RTC processing chain, MapReady allows to perform calibration to sigma nought, terrain correction using a manually uploaded

DEM NED1 tile matching the extent of the study area, and geocoding to UTM Zone 7N, datum WGS84.

Once all the three datasets were analysis-ready, further processing was done using Sentinel Application Platform (SNAP) available from the European Space Agency (ESA). All the scenes were subset to the area of interest, namely the extent of OCF. Secondly, ERS 1/2 and R1 were speckle filtered using a 7x7 Lee filter to match the speckle filtering of the RTC S1 products. Finally, the scenes for each year (October to mid-March) were co-registered using product geolocation to create stacks of SAR image time-series and converted to a decibel (db) logarithmic scale traditionally used for C-band SAR analysis (e.g., Brown et al., 2010; Engram et al., 2018; Filipponi, 2019).

It is important to note that the four SAR platforms differ significantly in terms of spatial resolution/gird spacing, as well as spatial and temporal coverage. S1A provided full coverage of the OCF at least every five days between October and mid-March when data from both descending and ascending overpasses were used. Due to its relatively narrower swath size (100 km), ERS 1/2 did not cover the OCF in their entirety and scenes were much more sparse in time. Consequently, the majority of the OCF extent was covered only four to eight times per ice season. However, for certain parts of the OCF, a more frequent but irregular coverage was available. The wide swath ScanSAR imaging mode of RADARSAT-1 allowed for full coverage of the OCF. However, the revisit time was extremely variable from month to month and year to year, anywhere from daily to monthly revisits.

Instrument	Year	Polarization	Imaging Mode	Data Product	Pixel Size (m)	Spatial Resolution (m)	I.A.
Sentinel - 1	2020/2021; 2019/2020; 2018/2019; 2017/2018;	VV	IW (Interferometric Wide Swath) IW covers an area of 250 km	L2 RTC product	10 (30 after RTC)	5x20	20-45
ERS 1/2	2009/2010; 2008/2009; 1995/1996; 1994/1995; 1993/1994; 1992/1993	VV (central frequency 5.6 cm)	STD (SAR Imaging Mode; swath width of 100 km)	L1 amplitude CEOS image	12.5	26x6	23 at mid-swath
RADARSAT-1	1999/2000; 2000/2001; 2001/2002; 2002/2003; 2003/2004; 2004/2005; 2005/2006; 2007/2008	HH (central frequency 5.6 cm)	ScanSAR wide (SWB, swath width of 450 km)	L1 amplitude CEOS image	50	100x100	20-46

Table 4.1: Data used in the project (I.A. stands for Incidence Angle).

Sentinel 1		ERS 1/2		RADARSAT 1	
2020/2021 (28 full)	March 15	2009/2010 (32; 7 full)	March 4	2007/2008 (24 full)	March 10
2019/2020 (41 full)	March 13	2008/2009 (26; 7 full)	March 19	2005/2006 (16 full)	March 11
2018/2019 (37 full)	March 14	1995/1996 (52; 9 full)	March 13/16	2004/2005 (21 full)	March 16
2017/2018 (36 full)	March 12	1994/1995 (34; 6 full)	March 16	2003/2004 (24 full)	March 4
		1993/1994 (25; 4 full)	March 22	2002/2003 (32 full)	March 13
		1992 /1993 (30; 6 full)	March 10	2001/2002 (45 full)	March 14
				2000/2001 (22; 16 full)	March 13
				1999/2000 (30)	March 18

Table 4.2: Date of labeling and number of scenes by year (year (#of scenes), where full indicates # of full coverage scenes of OCF).

4.2 Annotated dataset creation

Machine learning and deep learning algorithms, in particular, require extensive annotated datasets to learn from. Therefore, a dataset consisting of 129,000 labeled backscatter time-series was created. Labeling was done in SNAP by manually placing pins at locations identified as either floating ice, bedfast ice, or land through visual assessment of the ice regime/land on the last day of the time-series for a given season. This was done for each of the 18-year SAR image stacks. Due to variable temporal coverage, the dates of labeling range from March 4 to March 22 (Table 4.2). The labeling date was selected as close as possible to mid-March, and for the dates that fell after mid-March, care was taken to ensure that the air temperature on that day was below $0°C$. Then, the backscatter values at the locations identified by each pin were extracted for each of the scenes in a SAR stack, creating time-series of labeled backscatter values for each year covering the October to mid-March period.

Labels were assigned based on the following three factors: 1) backscatter values, 2) value of the projected incidence angle of the SAR pulse, and 3) location of the pixel within the scene. Firstly, due to high dielectric contrast of water and ice, floating ice is characterized by higher backscatter values, while bedfast ice displays low backscatter due to the low dielectric contrast between ice and frozen sediments (Grunblatt and Atwood, 2014). Therefore, on a gray level scale floating ice appears bright (white to light gray), whereas bedfast ice is dark (dark gray to black). Secondly, previous studies have shown that backscatter intensity is dependent on incidence angle, and therefore can vary from scene to scene and within the same scene (Bartsch et al., 2017; Duguay and Wang, 2019). It has been noted in previous investigations that the threshold between bedfast and floating ice becomes lower as the value of the projected incidence angle increases (Bartsch et al., 2017). Hence, each scene was analyzed taking incidence angle into consideration. Finally, location within the lake was helpful for identifying ice regimes, since shallower shore areas tend to become bedfast, while deeper middle portions maintain liquid water under the ice (Pointner et al., 2019). In addition, ponds are likely to freeze to bed in their entirety, while bigger lakes display a combination of the two regimes. To distinguish between lakes and the surrounding land, early fall scenes (e.g., October, Figure 4.1) were used as a reference where water covered by very thin ice appears dark, while the land is bright due to the roughness of its surface and vegetation volume scattering (Huang et al., 2018).

To gear the dataset for the deep learning classification, all the time-series had to have equal length and temporal spacing. The total number of scenes for S1, ERS 1/2, and R1 ranged from as few as 16 scenes to a maximum of 61 scenes per year. Hence, temporal

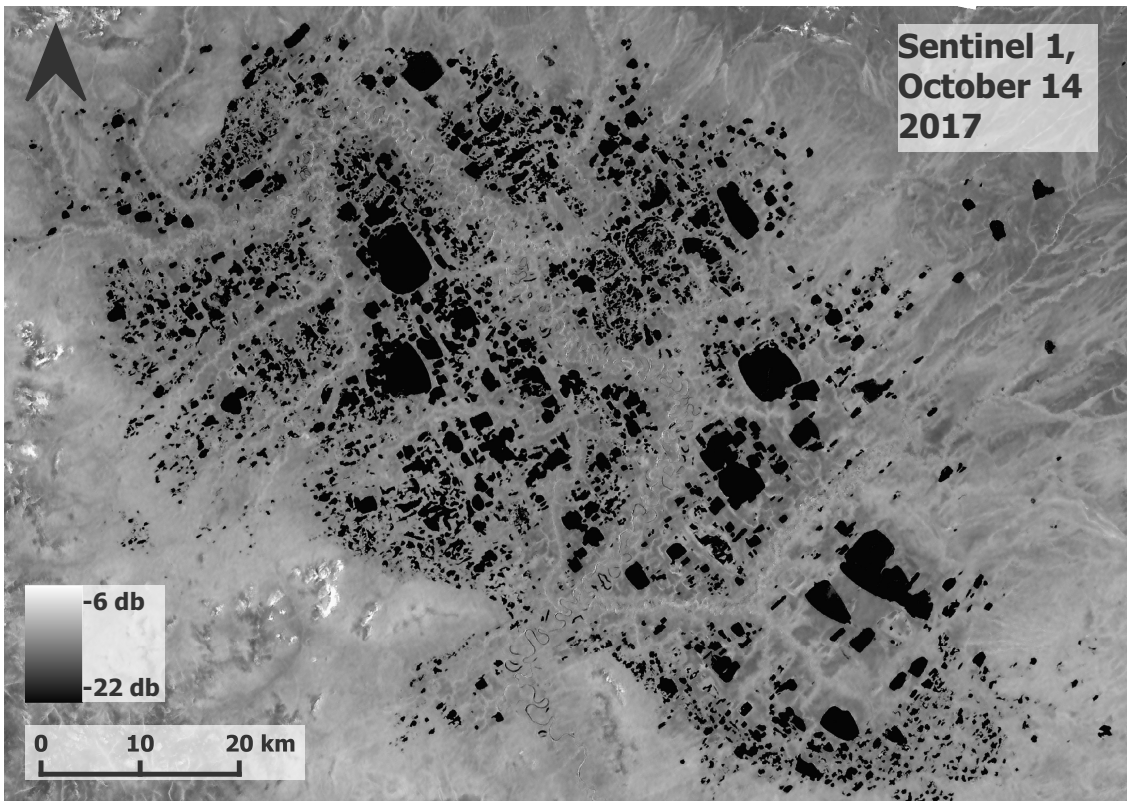


Figure 4.1: An example of an early fall scene used for identifying lake outlines during the labeling process (October 14, 2017, Sentinel 1). The greyscale corresponds to sigma nought (db) values. Lake surfaces appear black, while the surrounding land is grey.

resampling to a daily frequency and linear interpolation were applied to compensate for the temporal irregularity of the data. Although the lake ice lifecycle is non-linear, previous studies have shown that more complex interpolation methods have little influence on classification accuracy (Pelletier et al., 2019b; Valero et al., 2016). The final time-series consisted of 161 time steps (i.e., one time step per day) covering the time period between October 4 and March 13.

Figures 4.2 and 4.3 show comparisons of the interpolated time-series by class and by sensor. One can notice that the three classes are quite distinct. Both floating and bedfast ice demonstrate an initial drop in backscatter as thin ice forms on the wind-roughened water surface (Duguay and Lafleur, 2003). However, while floating ice backscatter gradually increases throughout the ice season, the bedfast ice backscatter peaks around January and then decreases as the ice becomes grounded (Figure 4.2) (Duguay and Lafleur, 2003). Land, on the other hand, shows little variability throughout the ice season and is characterized by a narrow range of backscatter values (Figure 4.2). In terms of sensor differences, S1 is characterized by the clearest pattern due to its denser temporal and spatial coverage, while ERS 1/2 appears to be the least structured (Figure 4.3). Nonetheless, the VV polarized S1 and ERS 1/2 and HH polarized R1 appear to have enough intraclass similarity and interclass distinctions to allow for successful temporal classification.

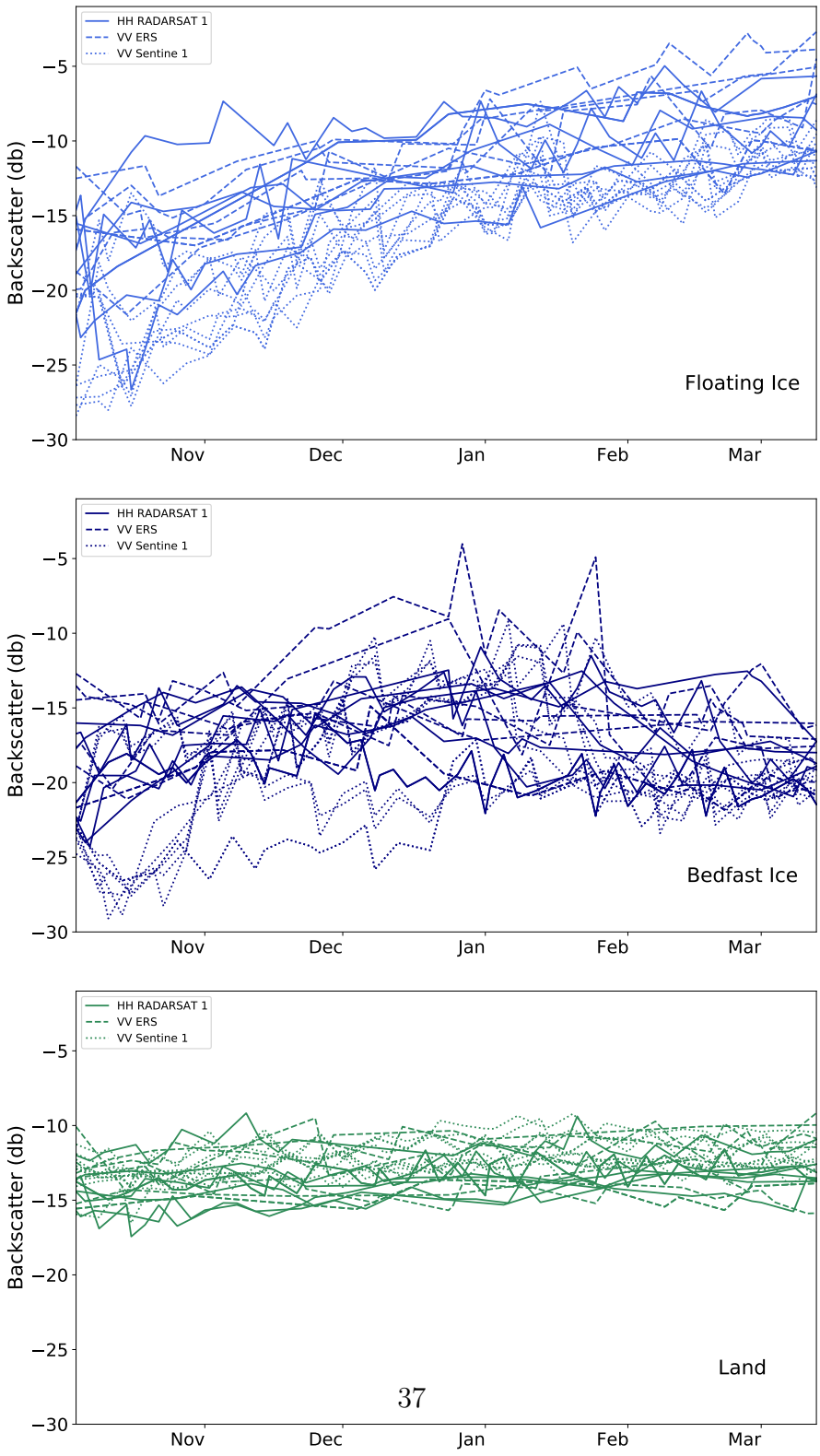


Figure 4.2: HH and VV seasonal cycles for RADARSAT 1(HH), ERS (VV), and Sentinel 1 by class (each sensor is represented by a sample of 6 randomly selected pixels per graph).

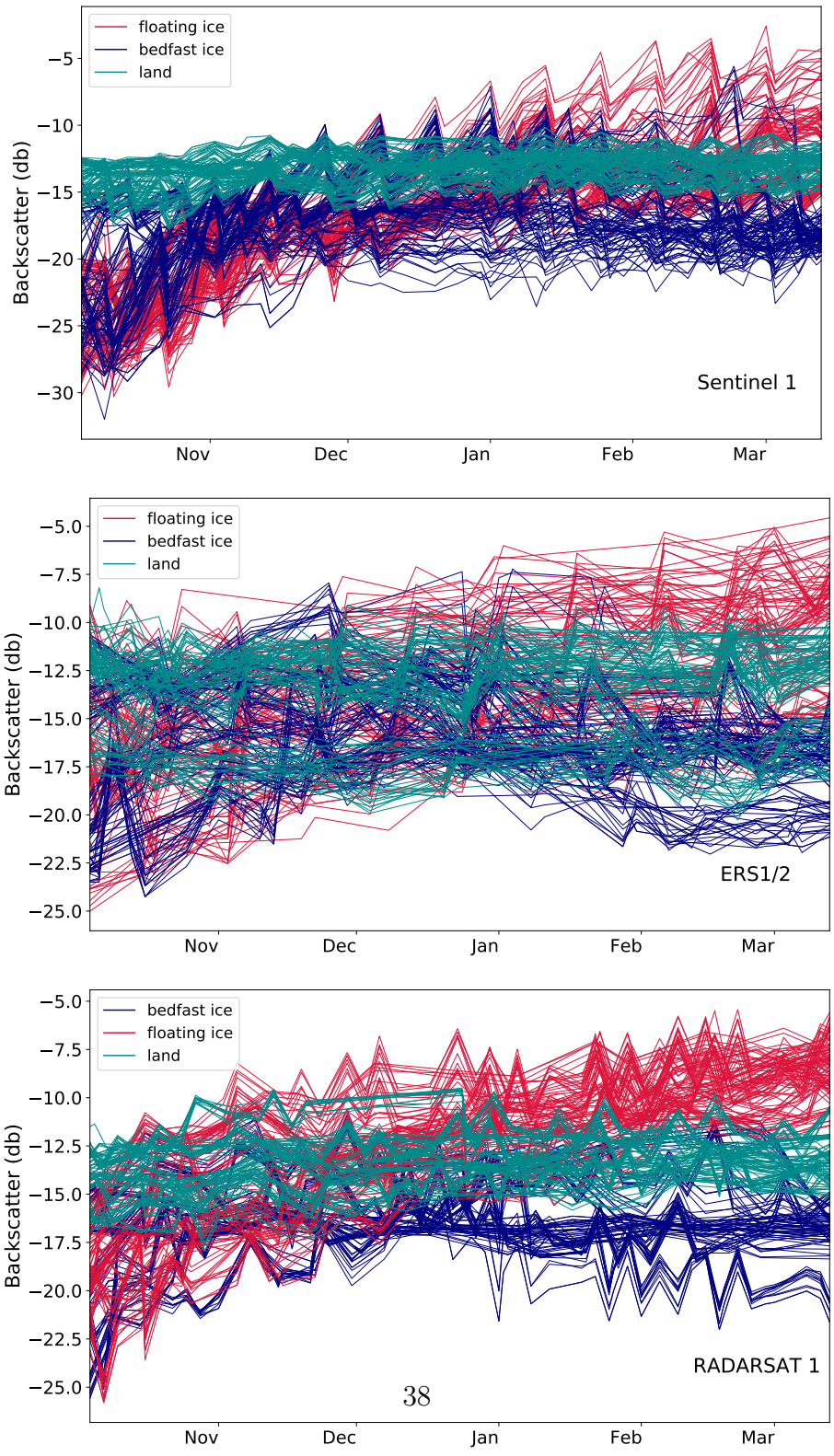


Figure 4.3: Comparison of the three classes by sensor: Sentinel 1, ERS1/2, RADARSAT 1 (each class is represented by a sample of 100 randomly selected pixels per graph).

4.3 Temporal Convolutional Neural Network

4.3.1 TempCNN

Although the field of remote sensing has been making use of machine learning techniques since the early 1960s (Holloway and Mengersen, 2018), permafrost research has not leveraged the full potential of deep learning tools. In this thesis, the temporal rather than spatial component of ice backscatter evolution is explored. Therefore, a temporal convolutional neural network (TempCNN) proposed by Pelletier *et al.* (2019) for land cover classification of optical image time-series that incorporates both a spectral and a temporal dimension was adopted. The study by Pelletier *et al.* (2019) shows that TempCNNs are more suitable for large scale studies due to their lower computational complexity, higher classification accuracy, and shorter training time than recurrent neural networks that are traditionally used for sequential data (Minh et al., 2018; Ndikumana et al., 2018). Herein, the only dimension of the data employed for the classification is the temporal dimension (1D TempCNN). However, the network structure allows for expanding it to cover both temporal and spectral dimensions (2D TempCNN). A TempCNN learns from the data by applying multiple different filters, also referred to as kernels, to the input time-series at the pixel level. A kernel of a given size constitutes a 1-dimensional array of values that convolves across the time-series from left to right. The kernel slides across the time-series moving at the stride defined by the user; in each position the values of the kernel are multiplied element-wise by the values of the portion of the time-series they overlap. The summed up resulting products become the part of the convolution output. This way, the number

of time steps of the input sequence considered in each calculation is determined by the size of the kernel. The information extracted by each kernel depends on the values that constitute it. For instance, Figure 4.4 demonstrates an input and an output for kernels of size 5 known as the gradient filter, the low-pass filter, and the high-pass filter that extract the information on whether the gradient of the input time-series is increasing or decreasing (Pelletier et al., 2019b), the trend of the time-series, and the cycling component of the time-series, respectively. In a TempCNN, each input time-series undergoes a number of kernels equal to the number of neurons (units) in a given convolutional layer. The best filters are learned by the network through the training process to allow for accurate mapping of the original input to the classification output of the final layer of the network.

4.3.2 TempCNN architecture

The TempCNN architecture used in this thesis is shown in Figure 4.5. The network consists of three convolutional layers, each of which contains 64 different filters with a kernel size of 5. Each filter is a one-dimensional array of weights that is multiplied with the input time-series. Each of the filters transforms the input time-series extracting specific patterns (Figure 4.4). Padding set to "same" in combination with the stride of the filter equal to 1 ensure that the input retains its size from one convolutional layer to the next. Pooling layers commonly used after each of the convolutional layers were omitted based on the findings of Pelletier *et al.* (2019) that showed that pooling not only does not contribute to better performance but in fact reduces the overall accuracy. The three convolutional layers are followed by a fully connected layer with 256 units. This layer performs the final class

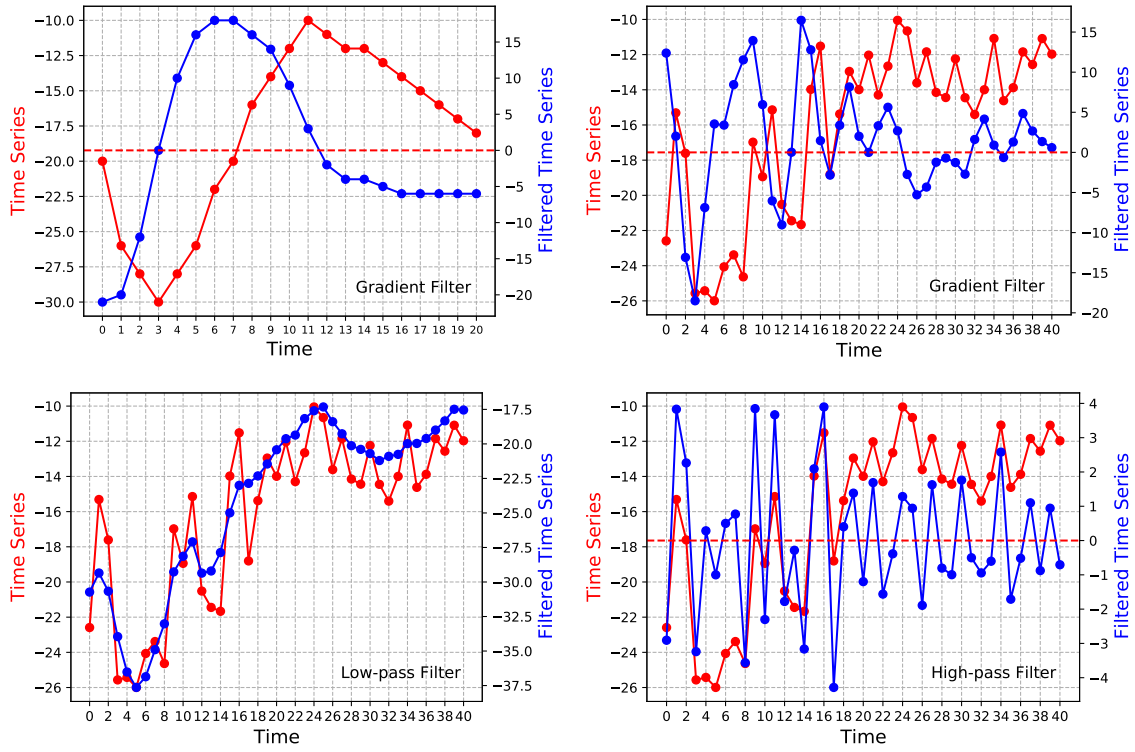


Figure 4.4: The four graphs illustrate application of 1-dimensional (1D) filters to time-series that can be used by convolutional layers of a TempCNN for extraction of temporal features. The red line represents original time-series, while the blue line denotes the filtered time-series. Top-left: simple general curve transformed by a gradient filter; top-right: a more complex curve that resembles floating ice transformed by a gradient filter; bottom-left: a curve resembling floating ice transformed by a low-pass filter; bottom-right: a curve resembling floating ice transformed by a high-pass filter.

assignment based on the final output of the convolution process. Finally, the softmax layer converts the probabilities output by the fully connected layer into class probabilities that sum up to 1. Ultimately, this information can be either used to create probability maps or transformed using an argmax function that selects the highest probability and assigns a class to each pixel.

The network was trained using an activation function called Rectified Linear Unit (ReLU). Once the input has been transformed by a convolutional unit, it is subsequently transformed by an activation function that introduces non-linearity to the model. The ReLU function outputs the input directly if it is positive and returns zero when faced with a zero or a negative input. Overfitting is a common deep learning problem. Overfit models perform extremely well on the training data, but generalize poorly to unseen data. In this thesis, the TempCNN incorporates four techniques that ensure that the model is well-trained, but at the same time able to perform well on new data: batch normalization, early stopping (patience = 10 epochs) controlled by a validation set that constitutes 5% of the training set, the dropout technique (rate = 0.5), and L2-regularization ($l2 = 1 * 10^{-6}$).

4.3.3 TempCNN architecture selection

In order to identify the best architecture a cross validation procedure was utilized. Out of 18 years of data, one year was reserved for final testing, while the remaining 17 years were used for identifying the best model structure. The aim of the cross-validation procedure was to determine the optimal number of units (4, 8, 16, 32, 64, or 128) to include in each

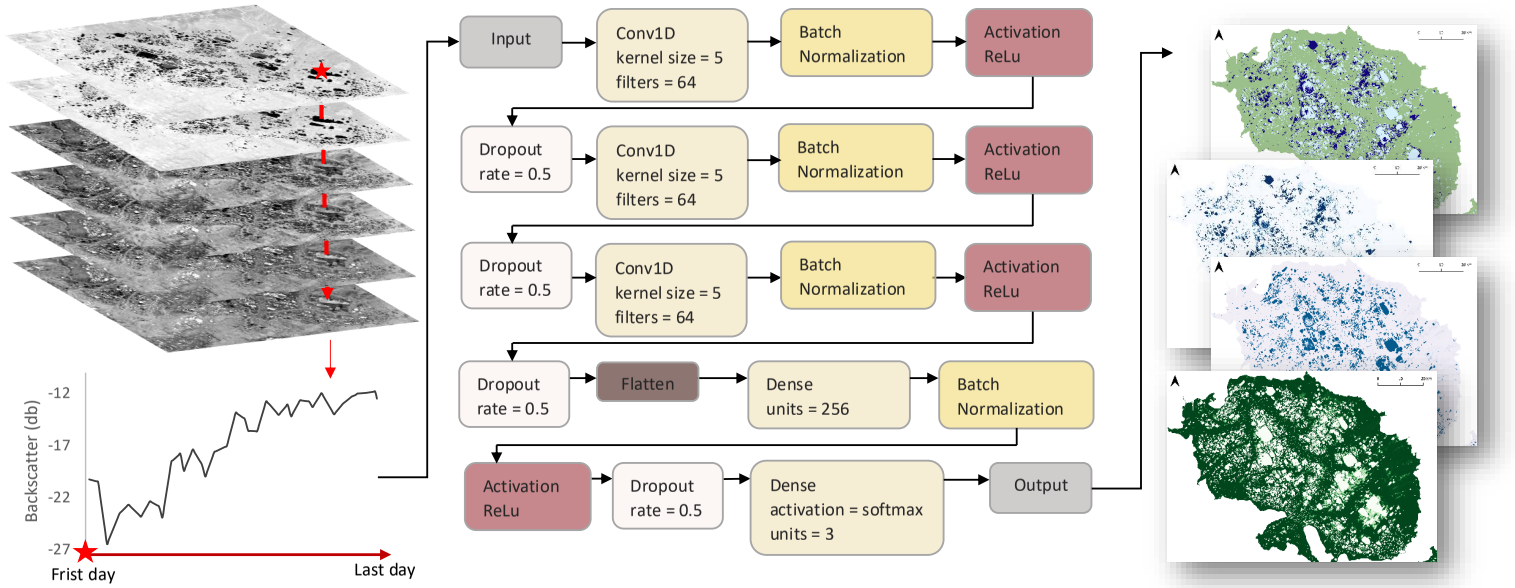


Figure 4.5: Structure of the trained TempCNN. The left portion represents an image stack that serves as an input to the neural network; the middle portion illustrates the composition of the TempCNN including layers, activation functions, and mechanisms for overcoming overfitting; the right portion represents the output created by the neural network that consists of a three-class (floating ice; bedfast ice; land) map, and three probability maps (one for each class).

	4	8	16	32	64	64 HP	64 long	128
mean	0.8828	0.9021	0.9105	0.9135	**0.9224**	0.9156	0.9192	0.9139
median	0.9290	0.9372	0.9564	0.9309	**0.9644**	0.9550	0.9597	0.9541
interquartile range	0.1539	0.1178	0.1192	0.1016	0.0959	**0.0884**	0.1152	0.1152

Table 4.3: Mean, median, IQR.

convolutional layer while keeping other elements of the structure constant (Figure 4.5). TempCNN with each number of units was trained on 16 years of data and tested on one year of data 17 times each time leaving a different year out for testing. The sets of 17 experiments were performed eight times. The results of each set of experiments in terms of overall accuracy are shown in a box-plot form in Figure 4.6 and summarized in Table 4.3. Based on the value of the median, interquartile range (IQR), length of the whiskers, and number of outliers, architecture with 64 convolutional units was identified as the best. In addition, two more sets of 17 experiments were carried out: 1) the input data was filtered prior to training using a Hodrick-Prescott filter (Hodrick and Prescott, 1997) that extracts the trend removing the cycling component; and 2) the original data was used to train the TempCNN model for a predefined number of epochs (40; with early stopping the average number of training epochs was 20). While in terms of IQR and number of outliers the filtered set performed better, the 64-unit architecture trained on the original data for a number of epochs determined by the early stopping technique performed better in terms of overall accuracy (median and length of the whiskers). As such, this architecture was selected as the best model and was subsequently used for creating lake ice maps.

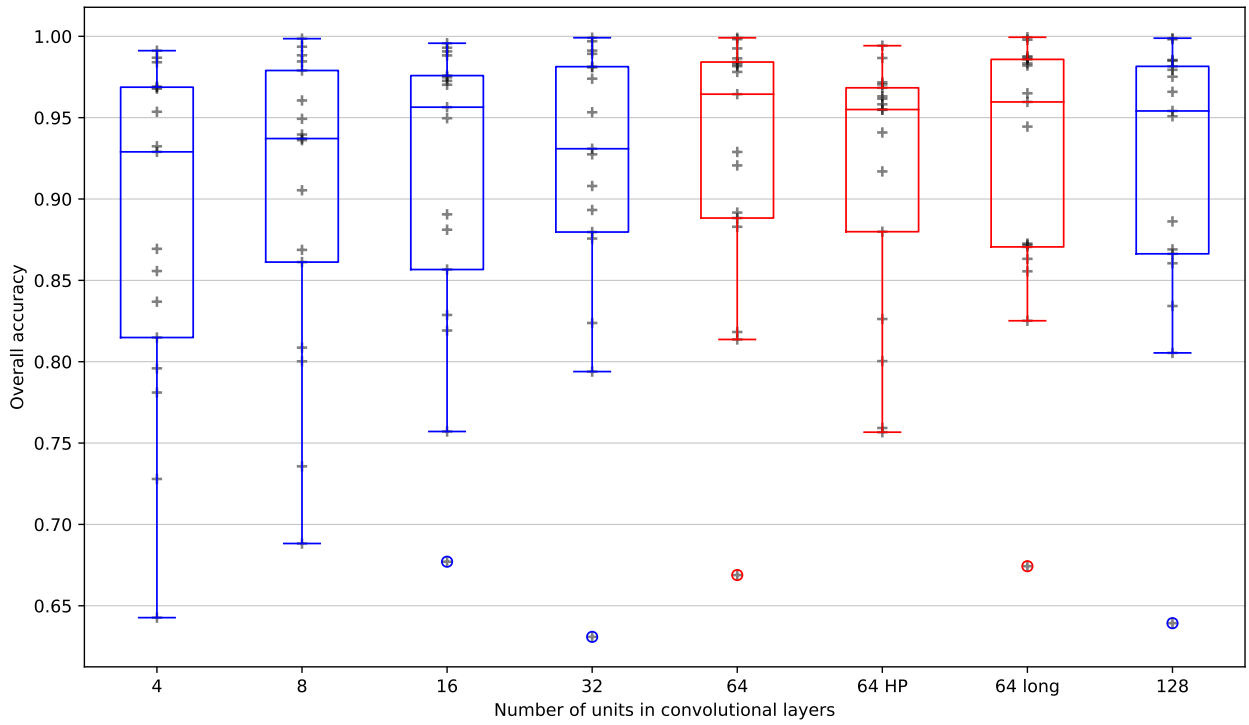


Figure 4.6: Temporal cross validation. 64 HP - 64 units convolutional layers filtered using Hodrick-Prescott filter, 64 long - original dataset trained for 45 epochs each (no early stopping).

4.3.4 TempCNN training and testing

Once the best model architecture was identified, the TempCNN model classification accuracy was evaluated through 15 more experiments to account for the stochastic nature of the neural network training process (Pelletier et al., 2019b). The training and testing were performed 15 times, consisting of three sets of five runs each split for training and testing differently. The first set randomly split the dataset into 80% for training and 20% for testing, this way incorporating data from all the years into both the training and the test set. The second set was trained on 15 years and tested on three years, where each test year was obtained by a different sensor. The third set was tested on 17 years of data and tested on the 18th year of S1, 2020/2021. This year was singled out for testing as it was initially reserved for validation and was not part of the dataset used to determine the best deep learning architecture in a cross-validation procedure outlined in the previous section (Wu et al., 2021). The model trained on points from all years of the SAR dataset was selected for the creation of lake ice regime maps. Although it is most likely worse at generalizing to unseen years and areas than other models, it produced better overall accuracy, and therefore is more likely to create high-quality maps for the purpose of ice regime change analysis. Other models generated by the experiment have been saved and will be used for future work.

4.4 Creation of ice regime maps using TempCNN

Prior to classification, SAR image stacks had to be interpolated to a daily frequency covering the period of time between October 4 to March 13 to match the temporal frequency of the time-series used for model training. Linear interpolation was done utilizing python programming language and the tools of pandas module. Interpolation not only filled the temporal gaps, but also replaced any missing or Not a Number (NaN) values, especially common for ERS1/2 and scene fringes. However, it is important to mention that linear interpolation is possible only between two values. For ERS1/2 very few scenes covered the OCF in their entirety, therefore some of the locations where missing the initial value and had to be filled with the nearest backscatter values within the same scene to allow for further interpolation.

Once the SAR stacks for 18 years were interpolated and each consisted of 161 scenes, the trained TempCNN model was used to create ice regime classification maps consisting of three classes: floating ice, bedfast ice, and land. Apart from outputting a classification map, TempCNN also provided probability maps for each class, where the value of each pixel corresponded to the probability of this pixel to belong to this specific class. The value of the three probability maps for a given pixel added up to 1. After classification, all the maps were subset using a mask created from a DEM. For consistency and subsequent change detection purposes, only areas with an elevation below 330 m were included. In addition, this step allowed to exclude high elevation mountainous areas surrounding the OCF that appear very bright in SAR imagery and could be misclassified as floating ice.

4.5 Accuracy assessment and comparison with lake ice model simulations

Due to the very limited ice regime (floating and bedfast) field observations, the accuracy assessment was challenging. In terms of field measurements, a set of bathymetry measurements collected in the OCF in late July 2000 were available. In addition, a small set of field measurements was collected in taiga and tundra zones of the OCF in spring of 2009 and 2021. Data collection included some or all of the following characteristics: ice thickness, ice regime, lake depth, temperature of the underlying sediment, and snow depth and density. Given the limited number of field measurements, lake ice thickness estimates were also obtained for comparison via simulations with the Canadian Lake Ice Model (CLIMo) (Duguay et al., 2003) over the period 1992-2021. CLIMo is a one-dimensional thermodynamic model designed for the simulation of lake ice formation, ice-growth and ice decay processes. The model has been shown to perform well for the simulation of ice dates and thickness on small (shallow) and large (deep) northern lakes (e.g., Brown and Duguay, 2011a; Duguay et al., 2003; Gunn et al., 2015b; Jeffries et al., 2005a; Kheyrollah Pour et al., 2017; Ménard et al., 2002; Surdu et al., 2014). In this study, CLIMo was forced with mean daily air temperature, wind speed, relative humidity, snow fall, and cloud cover produced from ERA-5 (global atmospheric reanalysis data, produced using ECMWF model freely available through the Copernicus Climate Change Service). In the simulations, lake depth was specified as 2 m. Snow density was set to $175\,kg/m^3$ for lakes located in the taiga zone and $300\,kg/m^3$ for those in the tundra zone. The density values were chosen based on the combination of limited field measurements and range of typical values reported in

the literature (Duguay et al., 2003; Jeffries et al., 2005a).

Bathymetric measurements of July 2000 were matched with the corresponding TempCNN predicted classes based on geolocation and analyzed in the context of CLIMo simulated ice thickness for the same year. Ice regime observations made in early April of 2009 and 2021 were also matched with the TempCNN classification output. Finally, in order to assess the accuracy of all the classified ice regime maps, the temporal ice regime change of one of the big OCF lakes was analyzed in the context of CLIMo ice thickness simulations for March 13 of each year. Other factors, such as possible water level fluctuations, were also taken into account by visually analyzing Landsat optical imagery and looking at precipitation data provided by Environment Canada.

4.6 Ice regime change analysis

In order to assess ice regime changes that took place in the OCF over the past three decades, change detection between the first (1992/1993) and the last (2020/2021) year of the series was performed, in addition to annual changes between all the available years. Due to the significant differences in spatial resolution (and grid spacing) between R1 and the other two satellite platforms, R1 scenes were compared only to each other (2000-2008). ERS 1/2 classified maps were resampled to match the pixel size of S1 (30 m) allowing for change detection between the four satellite missions (ERS1/2; S1A/B). Change maps were obtained using a simple raster calculation: $(Date1 * 10) + Date2$, which created an output where a two-digit number corresponded to the original class (1st digit) and the subsequent

class (2nd digit). When the two digits were the same, it indicated no change. Focus was placed on identifying changes between ice regimes and transitions between ice and land classes. The observed changes were analyzed in the context of CLIMo ice thickness simulations and known lake drainage and refilling events.

Chapter 5

Results and Discussion

5.1 TempCNN classification accuracy assessment

Our study shows that temporal deep learning offers a comprehensive framework that does not require a lake mask, as is the case for other studies on the topic of floating and bedfast ice mapping from SAR, and automatically classifies SAR imagery into three classes: floating ice, bedfast ice, and land. This approach offers high-quality ice regime maps for Sentinel 1 (S1), ERS 1/2 (ERS), and RADARSAT 1 (R1). Figures 5.1,5.2, and 5.3 show examples of TempCNN classification output for S1, R1, and ERS, respectively (all maps can be found in the Appendix). Although all the years were classified using the same deep learning model, map quality is dependent on the quality of the input SAR data. Spatial and especially temporal resolution of imagery through the ice season have a significant impact on the output of temporal classification. S1 data having a pixel size of 30 m and a

regular full coverage of the study area produced the best results, clearly separating the lake and the land classes. ERS is heavily affected by speckle noise, due to high original spatial resolution and small pixel size of 12.5 m and an irregular and sparse temporal coverage. In fact, available ERS scenes provided full coverage of the study area only 4-8 times in the lake ice season. Therefore, an extensive linear interpolation was employed to fill in the temporal gaps. R1 temporal coverage varies from year to year and has lower spatial resolution and a large pixel size of 100 m. Consequently, it suffers less from speckle noise and is able to capture lake shapes. However, smaller patches of bedfast ice and completely bedfast small ponds do not appear due to the coarser spatial resolution that cannot resolve smaller waterbodies compared to ERS and S1. It should be noted that years with high temporal resolution and more regular frequency showed better results for all three sensors.

As has been mentioned in Chapter 4, the TempCNN model classification accuracy was evaluated through 15 experiments. Table 5.1 presents the overall accuracy of the 15 experiments. The overall accuracy ranges from 91-99%. It should be noted that the model appears to be very sensitive to exclusion of certain years from that dataset. The sensitivity is likely attributed to temporal sparseness and irregular frequency of scenes. Especially for ERS, backscatter time-series vary significantly from year to year in terms of shape based on the missing time-periods. Although linear interpolation fills in the gaps, the major features of the lifecycle can be lost.

The following pattern emerged when analyzing confusion matrices from all experiments: the 80/20% models had very minimal misclassifications equally distributed between the

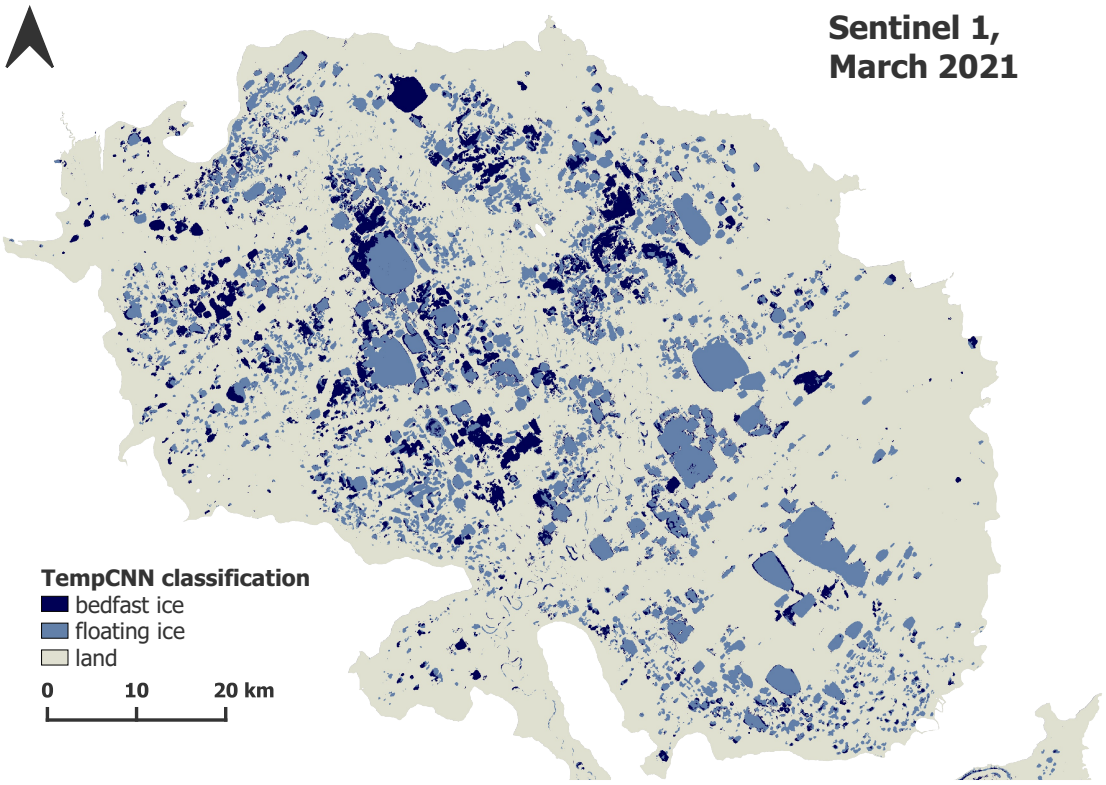


Figure 5.1: TempCNN classification output for Sentinel 1, March 2021, OCF, Yukon Canada.

Test set			20%					3 years					1 year		
Run	1	2	3	4	5	6	7	8	9	10	11	12	13	14	15
Overall accuracy	99.6	99.49	99.66	99.70	99.59	92.33	90.55	92.78	91.70	90.62	91.80	96.51	94.68	90.62	96.04
Mean accuracy			99.61					91.60					93.93		
Mean of means								95.05							

Table 5.1: TempCNN overall classification accuracy (15 experiments).

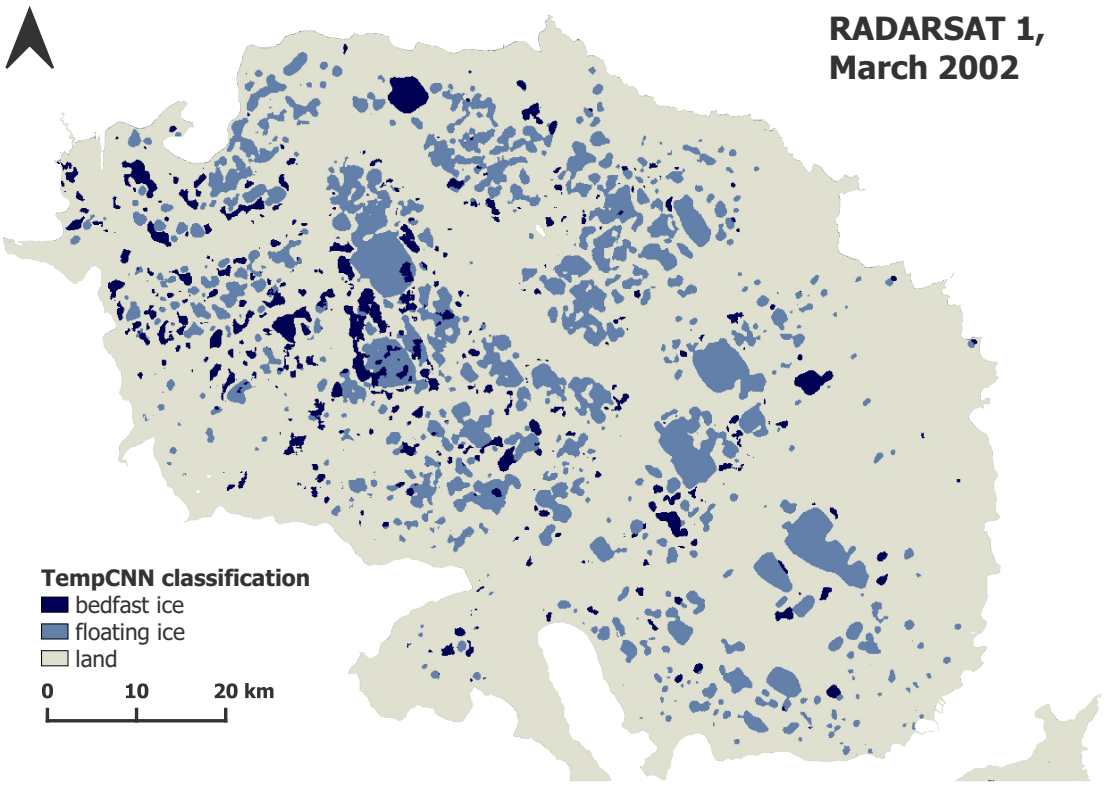


Figure 5.2: TempCNN classification output for RADARSAT 1, March 2002, OCF, Yukon Canada.

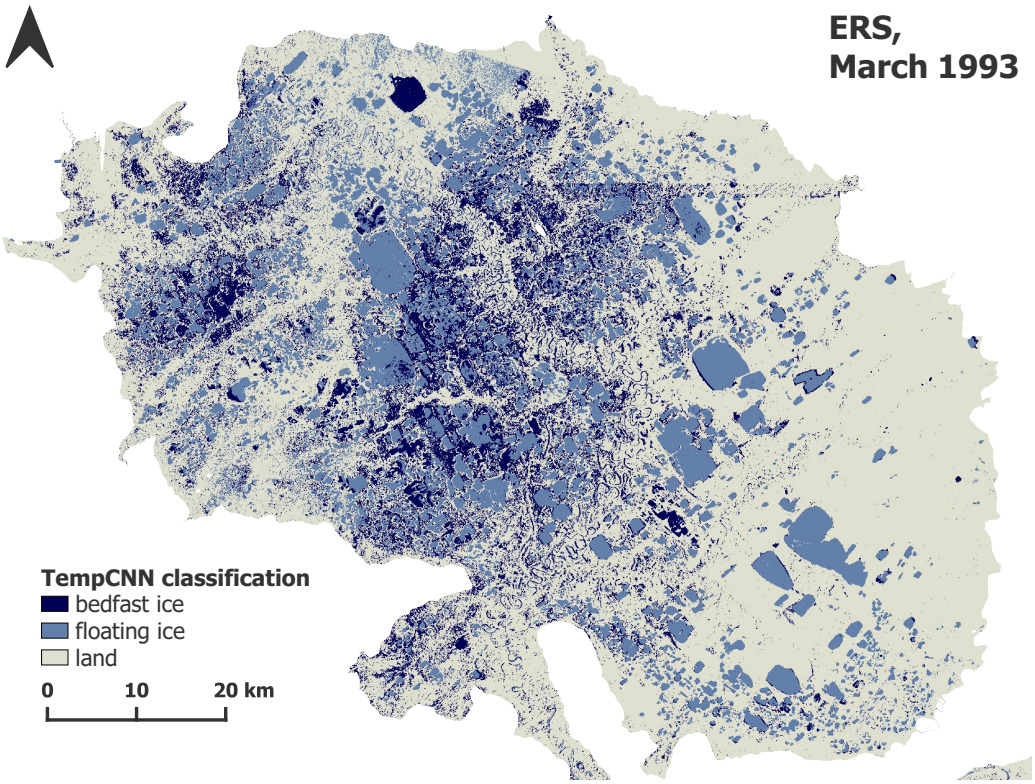


Figure 5.3: TempCNN classification output for ERS, March 1993, OCF, Yukon Canada.

three classes; the models tested on three years had most significant misclassification of land as bedfast ice; and the models tested on one year of S1 had most significant misclassifications of floating ice as bedfast ice. Land misclassification may be caused by the fact that the OCF is a wetland with varying distribution of surface water (water extent and level) that are frequently changing. Backscatter evolution of areas that have standing water will be very similar to that of bedfast lake ice making the distinction between the two classes challenging. It has been mentioned by a few researchers (e.g., Engram et al., 2018; Pointner et al., 2019), that deeper thermokarst lakes often display darker (low backscatter) patches of floating ice in their centers. Some lakes of the OCF manifest such patterns. Moreover, some of the years have characteristic dark spots in most of the lakes. Some of the recent studies (e.g., Engram et al., 2020; Pointner and Bartsch, 2020) suggest that the dark spots pattern could be a result of local ice thinning or complete melt caused by methane ebullition. Although these patterns have been accounted for in the labeled dataset as floating ice, the model still appears to struggle with some of those cases. Antonova *et al.* (2016) and Engram *et al.* (2018) also suggest that temperature of the underlying sediments, and whether they are fully frozen or not once the ice has become bedfast, could have an impact on the SAR backscatter.

5.2 Assessment against field observations and lake ice thickness simulations

Although an extensive accuracy assessment has been performed using the labeled dataset, the model prediction is only as accurate as the labeled data provided for its training and testing. Most of the field work conducted in the OCF is performed in summer (Labrecque et al., 2009; Lantz and Turner, 2015; Turner et al., 2010). Winter lake ice observations are largely non-existent for the OCF so that little is known about the actual ice regime (floating and bedfast ice) patterns of its lakes. As such, due to the lack of ground truthing, the labeled dataset used for model training was created from visual interpretation of SAR and optical imagery and, therefore, could contain erroneous labeling. In order to leverage the few field observations available to us and ice thickness simulated using CLIMo, classification results were compared against point lake depth measurements collected in 2000, observations of ice thickness and lake depth (or ice regime) at drilling holes collected in early April 2009 and 2021, and ice thickness model output from CLIMo. CLIMo simulated ice thickness has been successfully used in absence or in addition to limited field observations to provide context for SAR-derived lake ice regime findings by Surdu *et al.* (2014) and Antonova *et al.* (2016).

The lake ice regime is determined by multiple factors, including atmospheric conditions such as air temperature and snow accumulation on the ice surface (i.e. depth and density), which is impacted by wind and the presence/absence of vegetation cover surrounding the lake (forest and shrubs) (Duguay et al., 2003; Jeffries et al., 2005a). Another obvious

control on the lake ice regime is lake bathymetry; areas that exceed the depth of maximum ice thickness remain afloat, while shallower areas become bedfast (Arp et al., 2011). As such, point lake depth measurements collected in the OCF in late July 2000 were compared with the ice regime classification produced by the TempCNN model for the mid-March of 2000. Vegetation is another important factor. The OCF is a forest-tundra ecotone and while some lakes are surrounded by tundra, namely dwarf shrubs and herbaceous plants, some are located in deciduous, coniferous, or mixed forest, and others are fringed by a combination of tundra and forest environments (Turner et al., 2014). In tundra environments, wind controls snow depth and density, which have a greater influence on the ice thickness than air temperature (Brown and Duguay, 2010; Roy-Léveillée et al., 2014). For lakes surrounded by tundra the snow cover is expected to be thinner and denser leading to faster ice growth (Roy-Léveillée, 2014). In contrast, for taiga lakes surrounded by mixed and deciduous forest that facilitates greater loose snow accumulation providing insulation, ice growth is hindered (Roy-Léveillée, 2014). Figure 5.4 shows a plot of lake depths against mid-March SAR backscatter where the color of the points indicates the class predicted by TempCNN, while the shape refers to the surrounding vegetation (tundra, taiga, or combination of the two). In addition, the horizontal lines indicate the ice thickness simulated with CLIMo for mid-March of 2000 for two different snow scenarios. The line labeled as "CLIMo taiga ice thickness" represents a scenario of 100% snow cover and 175 kg/m^3snow density, while the line labeled as "CLIMo tundra ice thickness" represents a snow scenario of 50% snow cover and 300 kg/m^3 snow density.

The three bedfast (dark blue) locations align well with the CLIMo results (Tables

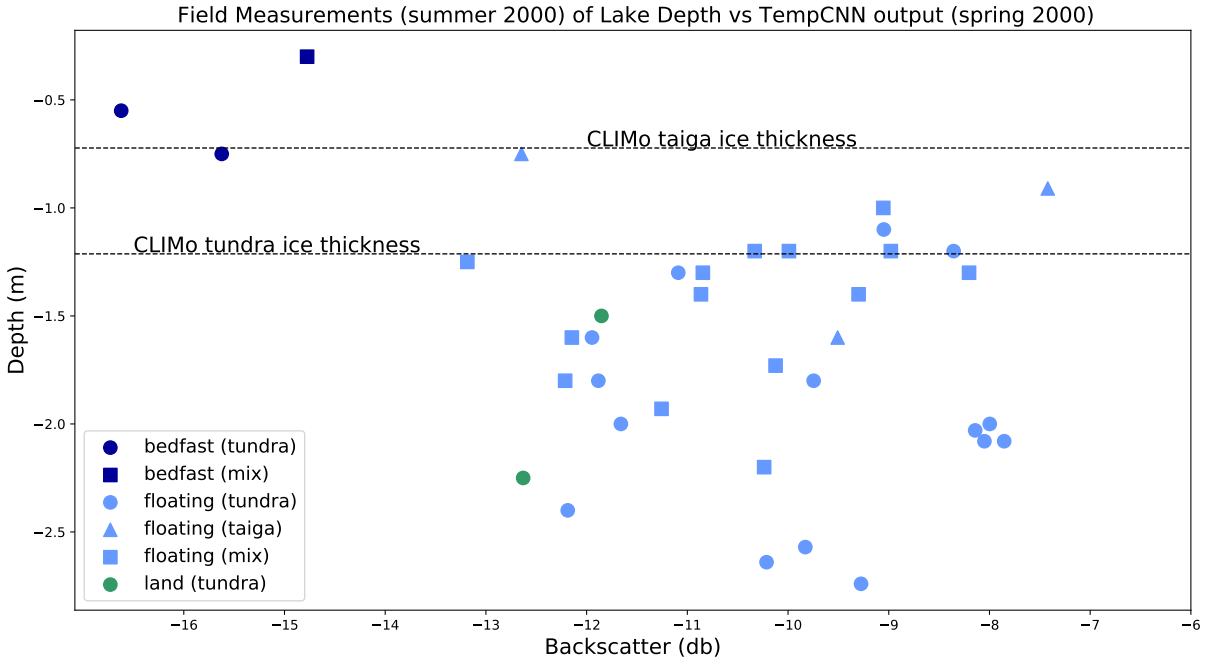


Figure 5.4: Matching TempCNN output with lake depths collected in 2000. Horizontal lines indicate CLIMo ice thickness predictions for taiga (0.72 m) and tundra (1.21 m) environments. RADARSAT 1 SAR time-series were used for ice regime classification.

5.4 and 5.5). The two tundra bedfast locations (dark blue circles) correspond to depths shallower than the CLIMo simulated ice thickness for tundra, while the one bedfast location surrounded by taiga (dark blue square) falls above the CLIMo simulated ice thickness for taiga. All of the tundra, taiga, and mixed vegetation locations with depths greater than the CLIMo simulated tundra ice thickness are classified as floating by the TempCNN indicating its accuracy. Out of the four floating ice points that fall in between the two CLIMo simulated values, two are surrounded by taiga (light blue triangles) and logically fall below the CLIMo simulated taiga ice thickness, while the remaining two points are surrounded by tundra (light blue circle) and mixed vegetation (light blue square). It is difficult to claim with certainty whether the two latter points are a TempCNN misclassification or are a result of local snow cover and vegetation variations as CLIMo output is sensitive to the input values of snow depth and density. As to the two points classified as land (green circles), one of them belongs to a lake that contains floating vegetation (Turner et al., 2014) that could contribute to the confusion between floating ice and land, while the second one belongs to a small pond whose backscatter signal was likely diluted in the surrounding land signal due to low spatial resolution and large pixel size of R1. Looking at Figure 5.4 it can be noticed that the deeper the lake, the lower is the backscatter of floating ice. This relationship contributes to the challenge of distinguishing between floating and bedfast ice in deeper lakes noted by a few researchers (Duguay and Wang, 2019; Engram et al., 2018; Pointner et al., 2019).

Apart from depth measurements, a small amount of ice thickness data was collected in OCF in April of 2009 and 2021. The results can be seen in Tables 5.2 and 5.3. For

Drill hole	Ice regime	Ice thickness (cm)	Snow depth (cm)	Sediment temperature (°C)	Backscatter (db)	TempCNN predicted ice regime
1	bedfast	67	46	<0	-18	bedfast
2	bedfast	79	37	0.5	-16.4	bedfast
3	floating	77	49	0.5	-10.17	floating
4	floating	81	39	0.5	-9.36	floating

Table 5.2: Field data collected in April 2021 on a small lake located beside the drained basin of Zelma Lake.

2021, the ice regime of the four points matches the TempCNN classification output. The field-observed ice thickness is between 77-81 cm, which is consistent with the taiga CLIMo prediction for the early April of 2021 (Figure 5.5). Table 5.2 also illustrates the effect of snow depth on the ice growth, as thicker snow above drill hole 3 corresponds to thinner ice, and thinner snow above drill hole 4 leads to thicker ice. For 2009, the first eight drill holes were made in tundra, where ice grows thicker (Table 5.3). All of the tundra drill hole locations were classified correctly by the TempCNN, with six floating ice locations (ice thickness less than lake depth), and two bedfast ice locations (ice thickness equal to lake depth). In taiga (two last drill holes), the ice is noticeably thinner. While one of the points was correctly classified as floating, the last drill hole was misclassified as land. This could be a result of the drill hole being close to the lake shore which in combination with low spatial resolution leads to mixing of backscatter contributions from the lake and the surrounding taiga.

Finally, using an example of a lake traditionally known as Husky Lake, we discuss the TempCNN ice regime classification (Figure 5.6) in the context of CLIMo simulated ice thickness over the 30-year time period (1993-2021) (Figure 5.5, Table 5.5). Due to the

Drill hole	Ice thickness (cm)	Lake depth (cm)	Ice regime	TempCNN predicted ice regime	Vegetation
1	109	154	floating	floating	tundra
2	124	208	floating	floating	tundra
3	125	145	floating	floating	tundra
4	130	200	floating	floating	tundra
5	140	232	floating	floating	tundra
6	102.5	102.5	bedfast	bedfast	tundra
7	151	151	bedfast	bedfast	tundra
8	132.5	213	floating	floating	tundra
9	77.5	232	floating	floating	taiga
10	100	191	floating	land	taiga

Table 5.3: Field data collection in the OCF in April 2009.

fact that Husky Lake is surrounded mainly by dwarf shrubs and herbaceous vegetation, tundra CLIMo simulation results were used. Aligning CLIMo simulated ice thickness with TempCNN classification results (Table 5.5) it was noticed that all years with simulated ice thickness equal to or thinner than 1.14 m were classified as floating ice, while all years with simulated ice thickness equal to or greater than 1.29 m were classified as bedfast. Years with simulated ice thickness ranging between 1.21 m and 1.23 m fluctuated between the two ice regimes. This could be attributed to the fact that CLIMo has a general uncertainty of approximately 0.05-0.06 m (Duguay et al., 2003) which could explain the fluctuations. In addition, according to Tondu (2012), depth of Husky Lake is approximately 1 m based on 2010/2011 observations. As such, CLIMo results for tundra are most likely overestimating ice thickness, while taiga simulation are underestimating it. Consequently, years where CLIMo simulated ice thickness ranged between 1.21 m and 1.23 m were likely characterized by ice thickness very close to the depth of Husky Lake, resulting in different

	1993	1994	1995	1996	2000	2001	2002	2003	2004
max ITh	0.81	0.81	0.80	0.85	0.86	0.80	0.82	0.81	0.84
Mar 13 ITh	0.72	0.71	0.74	0.74	**0.72**	0.70	0.73	0.73	0.71
	2005	**2006**	**2008**	**2009**	**2010**	**2018**	**2019**	**2020**	**2021**
max ITh	0.82	0.81	0.79	0.80	0.76	0.74	0.74	0.78	0.81
Mar 13 ITh	0.74	0.70	0.69	0.72	0.69	0.67	0.67	0.72	0.77

Table 5.4: CLIMo simulated ice thickness for OCF taiga: maximum ice thickness and March 13 ice thickness. Ice thickness value highlighted in red was used for 2000 field data analysis.

ice regimes for different years. The two years where CLIMo results seemed to contradict the TempCNN predictions were 2006 (1.19 m CLIMo simulated ice thickness; bedfast label) and 1996 (1.32 CLIMo simulated ice thickness; floating label). It is worth noting that ice thickness is not the only factor that dictates lake ice regime. Fluctuating lake water levels could result in different ice regimes given the same winter atmospheric conditions (Surdu et al., 2014). Therefore, mismatch between CLIMo and TempCNN predictions is most likely rooted in the water level difference. As is shown in Figure 5.7, the summer preceding spring of 2006 was characterized by lower water levels (drier year) based on visual analysis of Landsat optical imagery. Lower water level could potentially explain ice grounding in spite of thinner CLIMo simulated ice thickness. For 1996, on the other hand, the reason for floating ice regime, despite greater than usual CLIMo simulated ice thickness, was not identified. However, it is important to note that CLIMo simulations can be impacted by the quality of the atmospheric forcings input data. Visual analysis of mid-March SAR scenes in 1996 indicate widespread floating ice throughout the OCF.

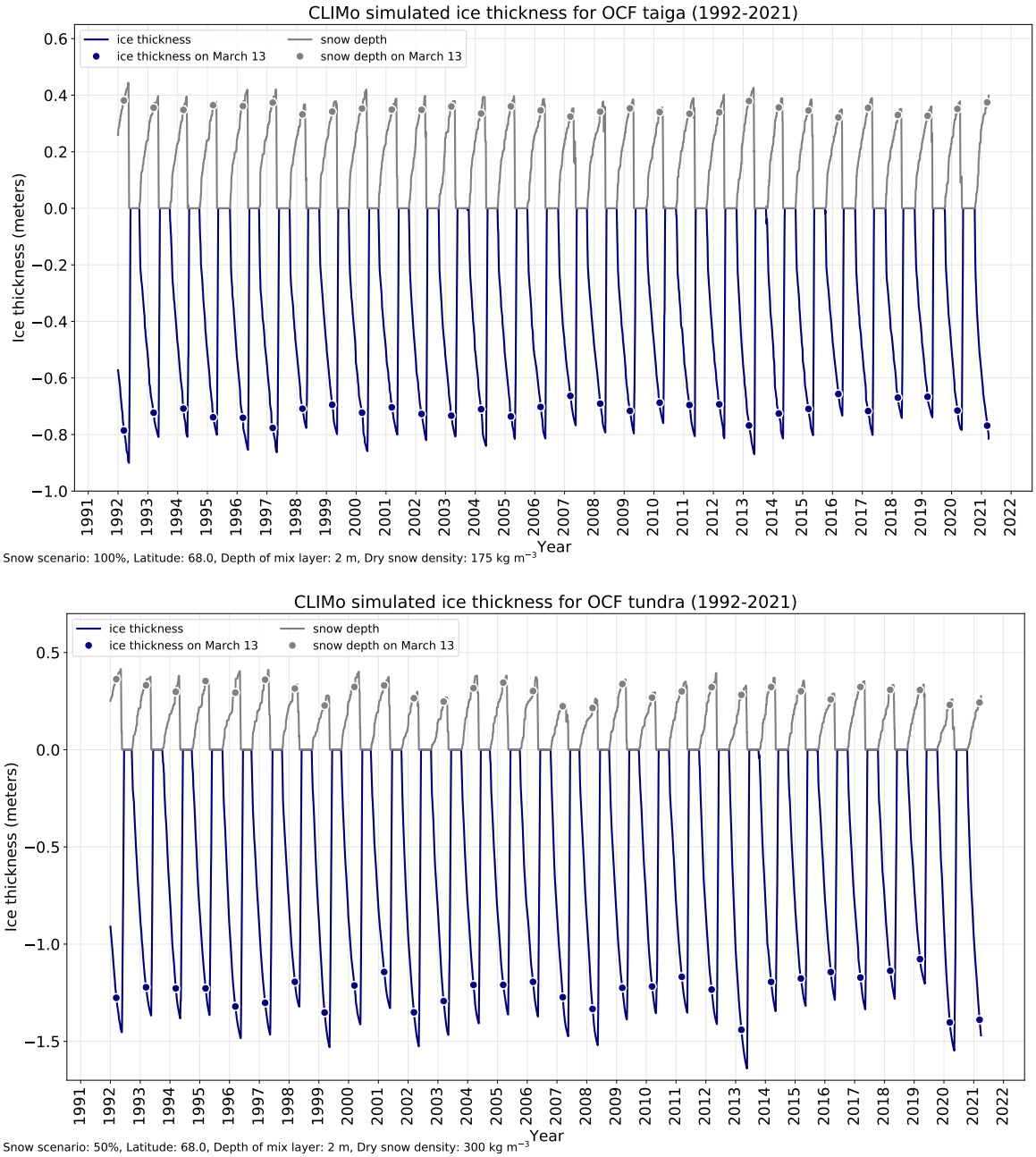


Figure 5.5: CLIMo simulated ice thickness for OCF (top: simulation of taiga environment; bottom: simulation of tundra environment).

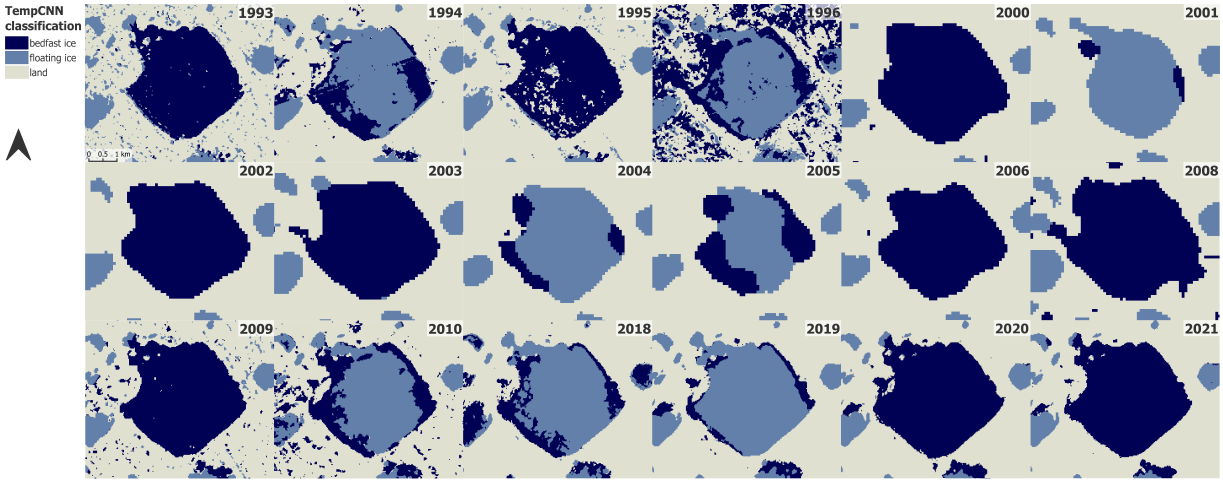


Figure 5.6: Husky Lake TempCNN predicted ice regime (1993-2021).

	1993	1994	1995	1996	2000	2001	2002	2003	2004
max ITh	1.37	**1.38**	1.37	**1.48**	1.41	**1.33**	1.53	1.47	**1.41**
Mar 13 ITh	1.22	**1.23**	1.23	**1.32**	1.21	**1.14**	1.35	1.29	**1.21**
	2005	**2006**	**2008**	**2009**	**2010**	**2018**	**2019**	**2020**	**2021**
max ITh	**1.36**	1.37	1.52	1.39	**1.36**	**1.28**	**1.20**	1.55	1.47
Mar 13 ITh	**1.21**	1.19	1.33	1.22	**1.22**	**1.14**	**1.08**	1.40	1.39

Table 5.5: CLIMo simulated ice thickness for OCF tundra: maximum ice thickness and March 13 ice thickness. Years highlighted in red had floating ice according to TempCNN.

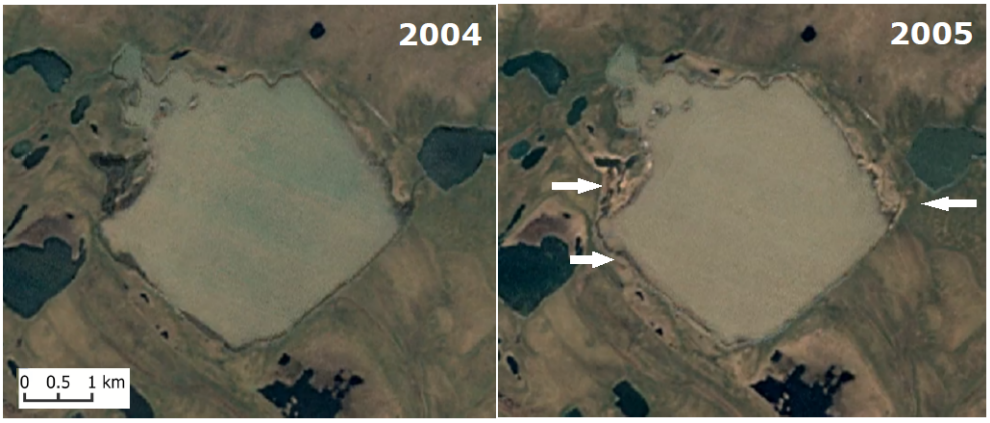


Figure 5.7: Husky Lake water level changes visible on Landsat imagery between summers of 2004 and 2005.

5.3 Ice regime change analysis

With the goal of analyzing changes in the ice regime of lakes within the OCF, this study yielded 18 lake ice regime maps from 1993 - 2021 created using SAR image time-series and the trained TempCNN deep learning model. The classified maps contain three classes, where two classes characterize the lake surface: bedfast ice and floating ice, and the remaining class encompasses the surrounding land area, which includes tundra, boreal forest, and more.

Performing change detection between the first (1993) and the last years of the dataset (2021), reveals a transition of 83 km^2 from bedfast to floating ice regime. However, 187 km^2 of floating ice shifted to a bedfast state. In addition, over the 30-year period, 148 km^2 transitioned from land to water reflecting active erosion processes (Roy-Roy-Léveillée and Burn, 2015), out of which 62 km^2 transitioned from land to bedfast ice, and 86 km^2 transitioned from land to floating ice. Figure 5.8 highlights the lake ice regime transitions

in dark and light blue, and also shows areas that switched from ice to land in green. The three insets illustrate each of the change types. According to ERA5 atmospheric data and CLIMo ice thickness simulations, the winters of 1993 was warmer than the winter of 2021 with the maximum ice thickness of $0.81\,m$ for taiga in both years and $1.37\,m$ and $1.47\,m$ in 1993 and 2021, respectively, for tundra. In mid-March, the simulated ice thickness was $0.72\,m$ for taiga and $1.22\,m$ for tundra in 1993 and $0.77\,m$ for taiga and $1.39\,m$ for tundra in 2021. Greater ice thickness simulated for 2021 helps explain part of the transition from floating to bedfast regime as for shallow flat-bottomed OCF lakes a 5-17 cm difference in ice thickness could allow for ice grounding. Moreover, as has been mentioned above, water levels play a significant role in winter lake ice conditions. As indicated by Lantz and Turner (2015) who studied OCF lake area changes in response to thermokarst processes and climate change between 1950 and 2009, the annual rate of lake drainage has increased 4-5 times in the recent decades. Looking at the change map, one can notice multiple locations where the significant ice regime change was indeed caused by significant changes in water level, in particular lake drainage and refills.

Firstly, let us look in more detail at Netro Lake that represents the most significant transition to a floating ice regime. Figure 5.9 illustrates its gradual transition from mostly bedfast to a mostly floating ice regime. It has been reported by Labrecque *et al.* (2009) that Netro Lake drained catastrophically losing $10.51\,km^2$ between 1972 and 2001. However, it appears that Netro Lake has not only refilled, regaining a lot of its area back, but has also transitioned to a floating ice regime.

The second example is Zelma Lake. Zelma Lake drained catastrophically in summer of 2007 through an outflow gully into a nearby creek losing 43% of its area over a course

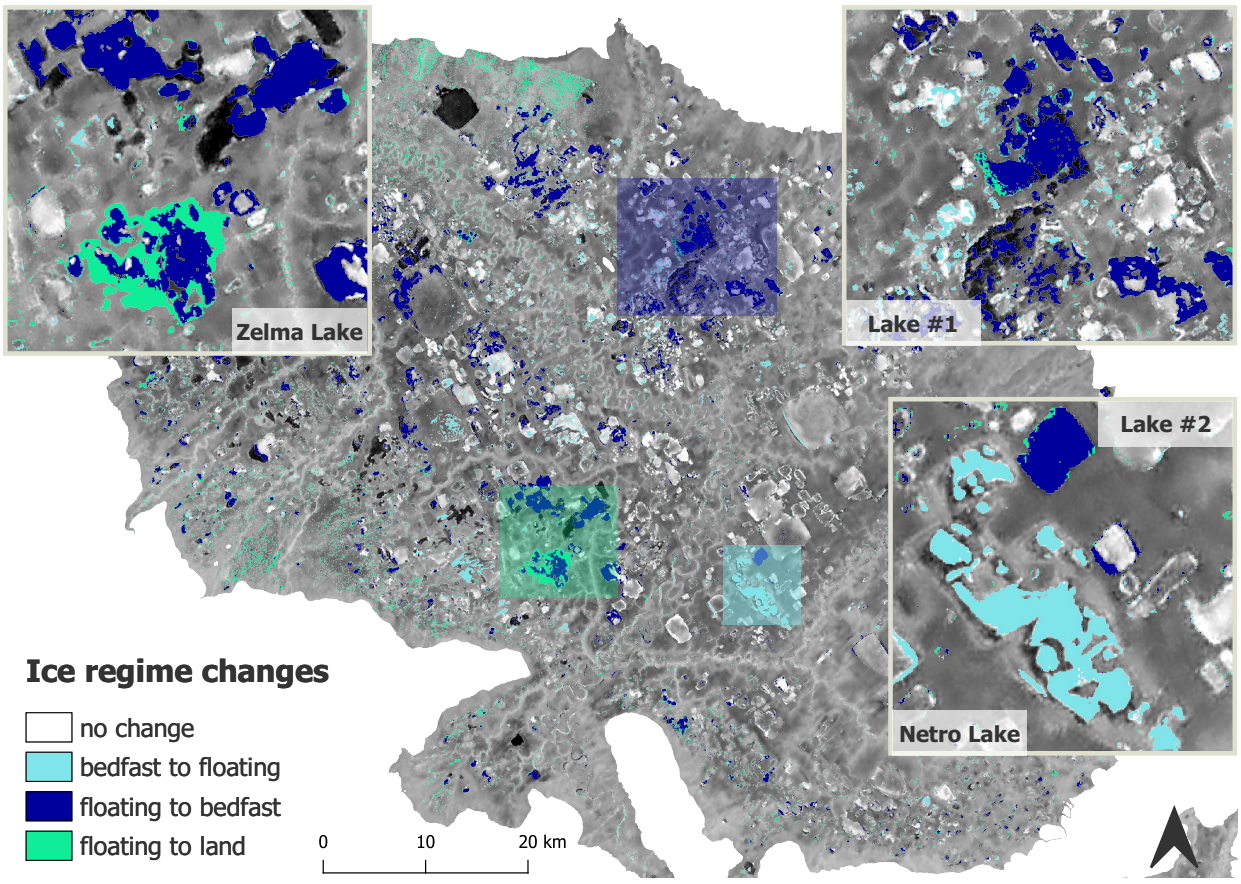


Figure 5.8: Change detection between 1993 (ERS) and 2021 (Sentinel 1) ice regime maps. Dark blue represents transition from floating to bedfast ice regime; light blue shows transition from bedfast to floating ice regime; green stands for transition from floating ice regime to land. The inset map in the top left corner is a zoomed in view of the area highlighted as a green rectangle on the main map; top right corner - dark blue rectangle; bottom right corner – light blue rectangle.

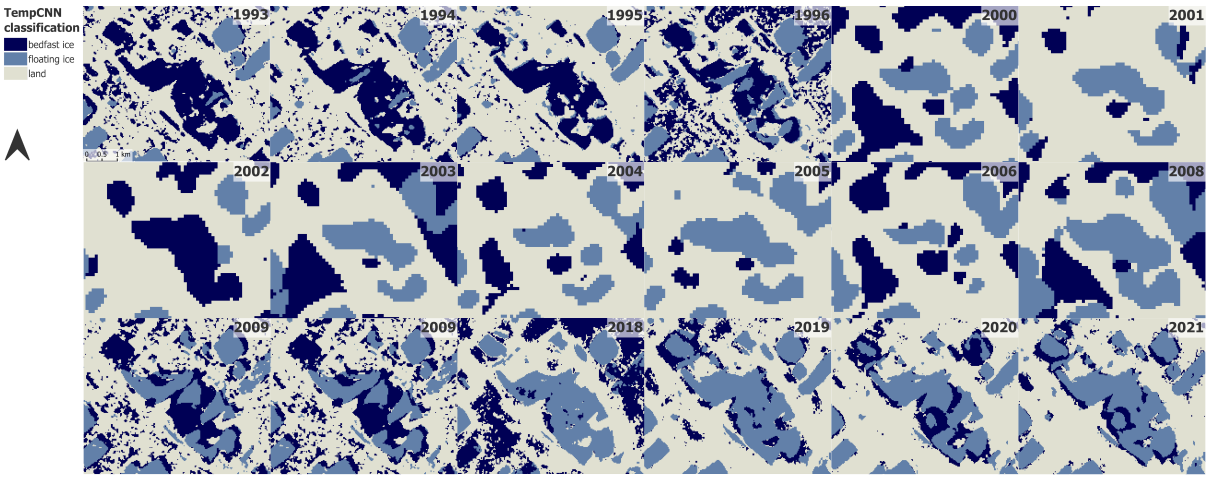


Figure 5.9: Netro Lake TempCNN predicted ice regime (1993-2021).

of a few weeks (Lantz and Turner, 2015; Turner et al., 2010). The drainage exposed approximately 5.2 km^2(Turner et al., 2010) of lakebed leaving behind shallow remnant ponds. Figure 5.10 illustrates ice regime changes over the course of the past 30 years. A significant reduction of lake area can clearly be seen between 2006 and 2008 maps. It should also be noted that the ice regime after the drainage has mostly become bedfast for years 2009, 2010, 2020, and 2021 following the drainage. The fact that 2018 and 2019 contain patches of floating ice in deeper areas can be explained by these two years being significantly warmer than the others resulting in thinner ice (Figure 5.5).

The two other lakes that experienced drainage events in the recent years are referred to as Lake #1 and #2 in Figure 5.8. Lake #1 and #2 presumably drained in 2017 and 2018, respectively, and therefore are not mentioned in the study of Lantz and Turner (2015). Figures 5.11 and 5.12 present lake ice regime change detection between 2010 and 2018 for both lakes. Change maps reveal extensive transition to a bedfast lake ice regime (dark

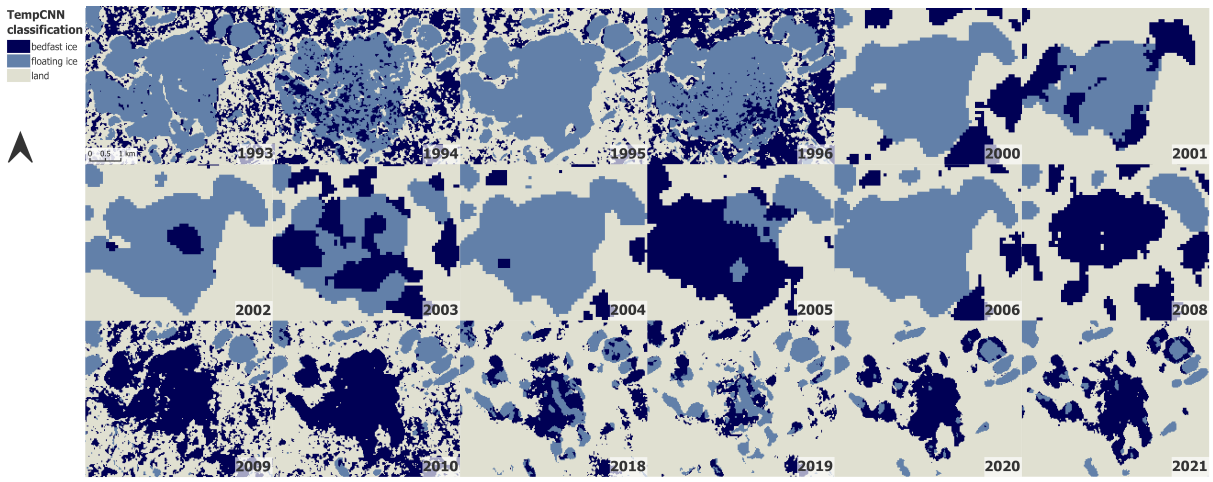


Figure 5.10: Zelma Lake TempCNN predicted ice regime (1993-2021).

blue) as the lakes drained and became shallower. Both change maps are supplemented with Landsat images that clearly demonstrate exposed land at lake edges. It is worth noting that extensive lake drainage (192 lakes) has been recently documented for nearby northwestern Alaska in 2018 and explained by winter 2017/2018 being the warmest and wettest on record (Nitze et al., 2020).

It is important to consider that a variety of simultaneous processes are working to modify the OCF landscape. For instance, while larger lakes drain losing surface area, smaller ponds are forming and expanding through permafrost thaw and erosion processes (Labrecque et al., 2009; Roy-Léveillée and Burn, 2010; Roy-Roy-Léveillée and Burn, 2015) as is illustrated in Figure 5.8. However, based on the above examples, it appears that the ice regime changes are significantly impacted by drainage events driven by a combination of climate change and thermokarst processes (Labrecque et al., 2009; Lantz and Turner, 2015).



Figure 5.11: Lake #1: Transition from floating to bedfast ice regime between 2010 and 2018 (left). Water level changes visible on Landsat imagery between summers of 2016 (center) and 2017 (right).



Figure 5.12: Lake #2: Transition from floating to bedfast ice regime between 2010 and 2018 (left). Water level changes visible on Landsat imagery between summers of 2017 (center) and 2018 (right).

To capture inter-annual changes that occurred with lake ice regimes, change detection was performed between each year of the available data. Due to a significantly larger pixel size of R1, it was analyzed separately from ERS and S1 that were resampled to the same pixel size of 30 m to allow for change detection. Table 5.6 and Figure 5.13 quantify and illustrate inter-annual ice regime transitions and transitions between floating ice and land which are assumed to capture lake drainage and expansion. For instance, summer of 2007 was characterized by high precipitation, leading to drainage events (Ex. Zelma Lake). Those events are captured in the spike in floating ice to land transition evident in 2009 on the bottom graph of Figure 5.13 (2009 represents the change that took place between 1996 and 2009, including 2007). In addition, the changes between 2010 and 2018 appear to be greater than between any other two years in terms of ice regimes (Figure 5.13, top graph). Transitions from floating to bedfast ice and vice versa are occurring simultaneously in different OCF locations with the dominating process changing from year to year. However, the change detection between the very first (1993) and the very last (2021) year indicate a more dominant transition to bedfast ice regime. Lake drainage is likely a significant contributor to this type of ice regime transition.

Scenes compared (mid-March)	Floating to bedfast (km^2)	Bedfast to floating (km^2)	Floating to land (km^2)	Dominant ice regime transition
1993 vs 1994	144	150	179	floating
1994 vs 1995	90	149	129	floating
1995 vs 1996	83	93	88	floating
2000 vs 2001	70	25	179	bedfast
2001 vs 2002	44	56	74	floating
2002 vs 2003	72	30	79	bedfast
2003 vs 2004	25	124	215	floating
2004 vs 2005	129	29	88	bedfast
2005 vs 2006	36	163	222	floating
2006 vs 2008	44	20	138	bedfast
1996 vs 2009	150	67	285	bedfast
2009 vs 2010	112	49	117	bedfast
2010 vs 2018	263	130	95	bedfast
2018 vs 2019	84	223	54	floating
2019 vs 2020	138	157	47	floating
2020 vs 2021	99	32	25	bedfast
1993 vs 2021	187	83	197	bedfast

Table 5.6: Inter-annual change in regimes.

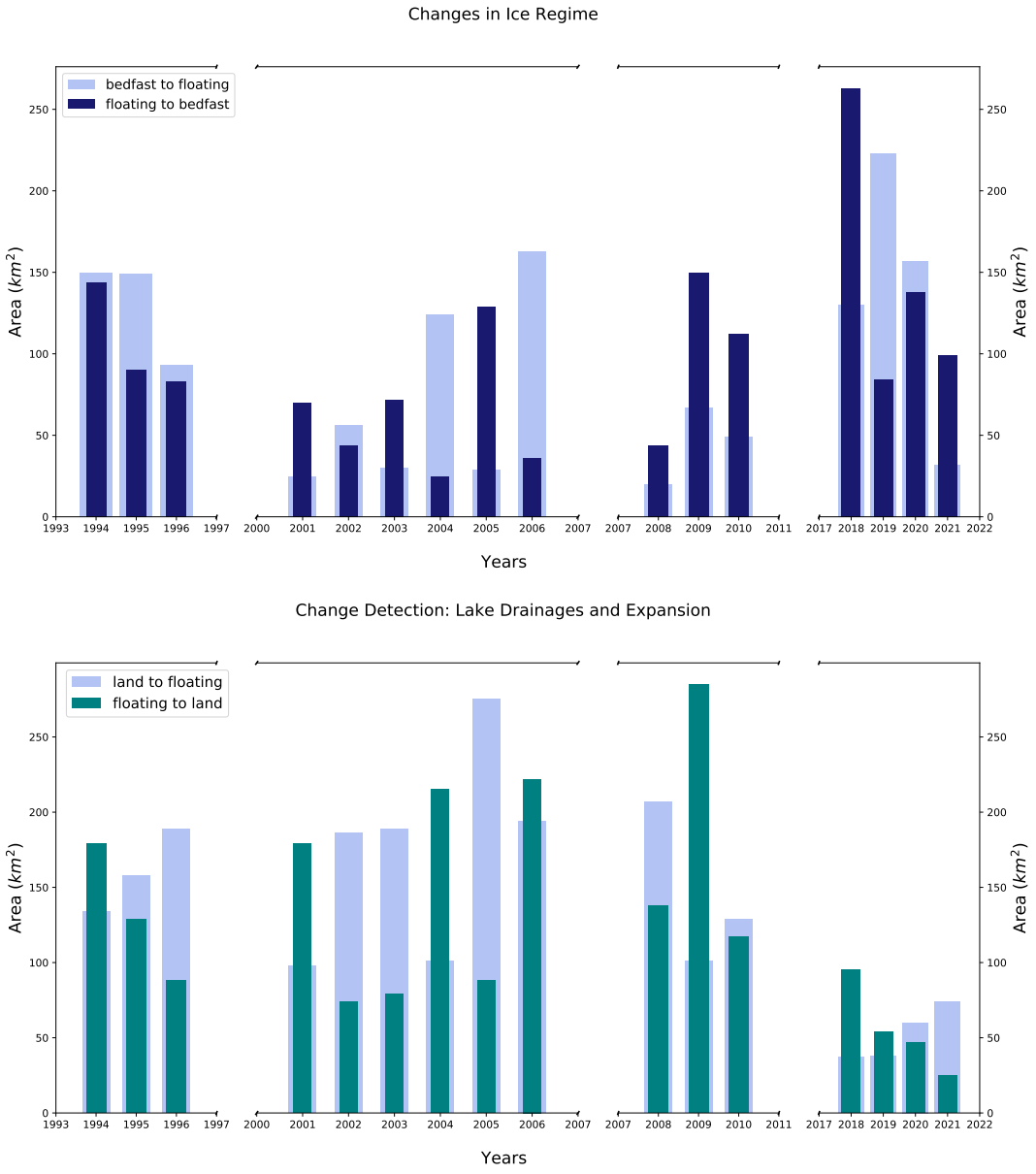


Figure 5.13: Change detection analysis (top: ice regime transitions; bottom: water and land transitions). The height of each bar in both charts represents the area in km^2 that transitioned between the two ice regimes (top chart) and floating ice regime and land (bottom chart) between two consecutive years of the dataset.

Chapter 6

Conclusion

6.1 Concluding remarks

Automated mapping of lake ice regimes from C-band SAR is an important but challenging task. The main classification issues encountered in previous studies are the lower backscatter of deeper floating ice areas, presence of cracks and small patches of thin ice, water salinity, presence of wet snow, dependence of backscatter on incidence angle of the instrument, and specificity of the threshold value or function to a study area or an instrument (Bartsch et al., 2017; Duguay et al., 2002; Duguay and Wang, 2019; Grunblatt and Atwood, 2014; Pointner et al., 2019). In an attempt to tackle the challenges of lake ice regime automated classification and propose a more universal classification method, in this work we explored a temporal deep learning approach in application to lake ice regime mapping from C-band SAR time-series. Scenes covering the period of time from October to mid-March for each

year of data were obtained from Sentinel 1, ERS 1 and 2, and RADARSAT 1 and were used to create an extensive annotated dataset of time-series each labeled as either floating ice, bedfast ice, or land based on the ice regime on the last day of the series. A temporal convolutional neural network (TempCNN) was trained and tested using the annotated dataset. The trained network, in turn, was employed to create lake ice maps of the Old Crow Flats, Yukon, Canada covering a period of 29 years from 1993 to 2021. The ice regime maps allowed to perform ice regime change detection analysis.

It was found that the TempCNN approach offers a comprehensive automatic classification framework suitable for different polarizations (HH and VV), SAR platforms, and years. In addition, it does not require a lake mask, in contrast to all the previously proposed methods (Bartsch et al., 2017; Duguay and Wang, 2019; Engram et al., 2018; Pointner et al., 2019). However, it was also found that the accuracy of the lake ice maps is heavily dependent on the temporal density and quality of the input data. Sentinel 1 time-series produced the best maps due to a combination of spatial resolution appropriate for the task, dense temporal coverage, and full spatial coverage of Old Crow Flats. The ice map accuracy was validated using a small set of field measurements and CLIMo simulated ice thickness. Field bathymetry data and ice regime measurements aligned well with the TempCNN classification output. It was noted that effects of surrounding vegetation on the ice thickness are important to consider, as some of OCF lakes are surrounded by tundra, some by boreal forest, and some by a combination of the two. In terms of inter-annual changes, lake ice regimes aligned well with the CLIMo predicted ice thickness, confirming its sensitivity to atmospheric conditions. Apart from ice thickness, water level of the lakes

was suggested to have a significant impact on the ice regime inter-annual variability. No long-term transition to an increased number of floating ice lakes was observed. On the contrary, it was noticed that the area covered by bedfast ice has increased over the 29-year period. Analyzing changes in ice regime in the context of an increased frequency of catastrophic lake drainages driven by climate change and thermokarst processes, in addition to a significant number of lakes experiencing bidirectional changes in water area, and lakes exhibiting gradual reduction in water area (Lantz and Turner, 2015), it was noticed that lake drainages are often associated with the transition from a floating to a bedfast ice regime. Further investigation is required to assess the influence of widespread lake drainages and the transition to shallower bedfast lakes on the condition of the underlying permafrost taking into account vegetation succession associated with lake drainages and climate change (Lantz, 2017).

6.2 Recommendations for future work

This study demonstrates the promising potential of a temporal deep learning approach to C-band SAR lake ice regime automated classification. However, when working with deep learning it is essential to understand that the result is only as accurate as the annotated dataset used for neural network training, validation, and testing. Therefore, in order to create a truly robust temporal deep learning model an extensive field data collection including ice regimes and lake bathymetry is indispensable. This will not only allow for creation of a highly accurate labeled dataset, but also for a highly reliable accuracy

assessment. In this work we have relied on a general assumption that shallower lake fringes generally freeze to bed while deeper lake centers remain afloat. However, for flat-bottomed OCF lakes (Roy-Roy-Léveillée and Burn, 2015), this assumption does not necessarily hold true. For instance, some lakes appeared to have very dark middle and bright edges. This pattern could be explained by greater snow accumulation at the margins or the contribution of the surrounding shrubs to volume scattering. In addition, flat lakebeds with slight local depth variations could lead to isolated patches of bedfast ice surrounded by floating ice, which are generally considered to be misclassified. As such, ground truth is essential for designing an accurate classification algorithm. In addition, the current temporal deep learning model learns only from the temporal component of the data. In future work, incorporation of the spatial component could greatly reduce misclassifications associated with deeper regions with dark signatures. Furthermore, a study by Wang *et al.* (2020) indicates a significant shrubification trend in the arctic-boreal northwestern North America. Shrubification could potentially lead to greater snow accumulation and reduced ice growth, particularly near lake shores, resulting in a transition of affected lakes to a floating ice regime. Consequently, for developing a better understanding of underlying causes of ice regime transitions, it would be valuable to investigate ice regime trends in the context of OCF shrubification. Finally, the temporal resolution of the analyses can be improved by taking advantage of other C-band SAR platforms, such as Envisat ASAR, RADARSAT 2, and the recently launched RADARSAT Constellation Mission (RCM).

In conclusion, this work provides a strong baseline for future development of deep learning automated classification algorithms that incorporate the temporal components

of lake ice evolution. Furthermore, the high spatial and temporal resolution provided by the Sentinel 1 mission combined with the future altimetry Surface Water and Ocean Topography (SWOT) mission (due for launch in 2022) will allow for higher accuracy mapping of water level of lakes than is currently possible. This comprehensive approach will remove the uncertainty of whether the ice regime change is associated with air temperature, snowfall, water level changes or a combination of these factors.

References

Abolt, C. J. (2019). *Trajectories of land surface evolution in polygonal tundra*. PhD thesis, The University of Texas at Austin, Austin, TX.

Antonova, S., Duguay, C. R., Kääb, A., Heim, B., Langer, M., Westermann, S., and Boike, J. (2016). Monitoring bedfast ice and ice phenology in lakes of the Lena river delta using TerraSAR-X backscatter and coherence time series. *Remote Sensing*, 8(11):1–23.

Arp, C. D., Jones, B. M., Bondurant, A. C., Grosse, G., Parsekian, A., Romanovsky, V., and Hinkel, K. M. (2016). Extreme sensitivity of shallow lakes and sublake permafrost to arctic climate change. In *Proceedings of XI International Conference on Permafrost*, pages 700–701, Potsdam, Germany.

Arp, C. D., Jones, B. M., Lu, Z., and Whitman, M. S. (2012). Shifting balance of thermokarst lake ice regimes across the Arctic Coastal Plain of northern Alaska. *Geophysical Research Letters*, 39(16):1–5.

Arp, C. D., Jones, B. M., Urban, F. E., and Grosse, G. (2011). Hydrogeomorphic processes

of thermokarst lakes with grounded-ice and floating-ice regimes on the Arctic coastal plain, Alaska. *Hydrological Processes*, 25(15):2422–2438.

Bartsch, A., Pointner, G., Leibman, M. O., Dvornikov, Y. A., Khomutov, A. V., and Trofaier, A. M. (2017). Circumpolar mapping of ground-fast lake ice. *Frontiers in Earth Science*, 5:1–16.

Belward, A., Bourassa, M., Dowell, M., Briggs, S., Dolman, H., Holmlund, K., and Verstraete, M. (2016). The global observing system for climate: implementation needs. Report GCOS-200, World Meteorological Organization.

Bouchard, F., MacDonald, L. A., Turner, K. W., Thienpont, J. R., Medeiros, A. S., Biskaborn, B. K., Korosi, J., Hall, R. I., Pienitz, R., and Wolfe, B. B. (2017). Paleolimnology of thermokarst lakes: a window into permafrost landscape evolution. *Arctic Science*, 3(2):91–117.

Brewer, M. C. (1958). The thermal regime of an arctic lake. *Eos, Transactions American Geophysical Union*, 39(2):278–284.

Brown, L. C. and Duguay, C. R. (2010). The response and role of ice cover in lake-climate interactions. *Progress in physical geography*, 34(5):671–704.

Brown, L. C. and Duguay, C. R. (2011a). A comparison of simulated and measured lake ice thickness using a Shallow Water Ice Profiler. *Hydrological Processes*, 25(19):2932–2941.

Brown, L. C. and Duguay, C. R. (2011b). The fate of lake ice in the North American Arctic. *The Cryosphere*, 5(4):869–892.

Brown, R. S., Duguay, C. R., Mueller, R. P., Moulton, L. L., Doucette, P. J., and Tagestad, J. D. (2010). Use of synthetic aperture radar (SAR) to identify and characterize overwintering areas of fish in ice-covered Arctic rivers: a demonstration with Broad Whitefish and their habitats in the Sagavanirktok River, Alaska. *Transactions of the American Fisheries Society*, 139(6):1711–1722.

Chen, Y., Lin, Z., Zhao, X., and Wang, Gand Gu, Y. (2014). Deep learning-based classification of hyperspectral data. *IEEE Journal of Selected topics in applied earth observations and remote sensing*, 7(6):2094–2107.

Cho, K., Van Merriënboer, B., Gulcehre, C., Bahdanau, D., Bougares, F., Schwenk, H., and Bengio, Y. (2014). Learning phrase representations using RNN encoder-decoder for statistical machine translation. *arXiv preprint arXiv:1406.1078*.

Duguay, C. and Wang, J. (2019). Advancement in bedfast lake ice mapping from Sentinel-1 SAR data. In *IGARSS 2019-2019 IEEE International Geoscience and Remote Sensing Symposium*, pages 6922–6925. IEEE.

Duguay, C. R., Bernier, M., Gauthier, Y., and Kouraev, A. (2015). Remote sensing of lake and river ice. *Remote sensing of the cryosphere*, pages 273–306.

Duguay, C. R., Flato, G. M., Jeffries, M. O., Ménard, P., Morris, K., and Rouse, W. R. (2003). Ice-cover variability on shallow lakes at high latitudes: model simulations and observations. *Hydrological Processes*, 17(17):3465–3483.

Duguay, C. R. and Lafleur, P. M. (2003). Determining depth and ice thickness of shallow

sub-Arctic lakes using space-borne optical and SAR data. *International Journal of Remote Sensing*, 24(3):475–489.

Duguay, C. R., Pultz, T. J., Lafleur, P. M., and Drai, D. (2002). RADARSAT backscatter characteristics of ice growing on shallow sub-Arctic lakes, Churchill, Manitoba, Canada. *Hydrological Processes*, 16(8):1631–1644.

Engram, M., Anthony, K. M. W., Sachs, T., Kohnert, K., Serafimovich, A., Grosse, G., and Meyer, F. (2020). Remote sensing northern lake methane ebullition. *Nature Climate Change*, 10(6):511–517.

Engram, M., Anthony, K. W., Meyer, F. J., and Grosse, G. (2013). Characterization of l-band synthetic aperture radar (SAR) backscatter from floating and grounded thermokarst lake ice in Arctic Alaska. *The Cryosphere*, 7(6):1741–1752.

Engram, M., Arp, C. D., Jones, B. M., Ajadi, O. A., and Meyer, F. J. (2018). Analyzing floating and bedfast lake ice regimes across Arctic Alaska using 25 years of space-borne SAR imagery. *Remote sensing of environment*, 209:660–676.

Filipponi, F. (2019). Sentinel-1 GRD preprocessing workflow. In *Multidisciplinary Digital Publishing Institute Proceedings*, volume 18, page 11.

French, H. M. (2018). *The periglacial environment*. John Wiley & Sons.

Geldsetzer, T., Sanden, J., and Brisco, B. (2010). Monitoring lake ice during spring melt using RADARSAT-2 SAR. *Canadian Journal of Remote Sensing*, 36(sup2):S391–S400.

Gruber, S. (2012). Derivation and analysis of a high-resolution estimate of global permafrost zonation. *The Cryosphere*, 6(1):221–233.

Grunblatt, J. and Atwood, D. (2014). Mapping lakes for winter liquid water availability using SAR on the North Slope of Alaska. *International Journal of Applied Earth Observation and Geoinformation*, 27:63–69.

Gunn, G. E., Brogioni, M., Duguay, C., Macelloni, G., Kasurak, A., and King, J. (2015a). Observation and modeling of X- and Ku-band backscatter of snow-covered freshwater lake ice. *IEEE Journal of Selected Topics in Applied Earth Observations and Remote Sensing*, 8(7):3629–3642.

Gunn, G. E., Duguay, C. R., Brown, L. C., King, J., Atwood, D., and Kasurak, A. (2015b). Freshwater lake ice thickness derived using surface-based X- and Ku-band FMCW scatterometers. *Cold Regions Science and Technology*, 120:115–126.

Hirose, T., Kapfer, M., Bennett, J., Cott, P., Manson, G., and Solomon, S. (2008). Bottomfast ice mapping and the measurement of ice thickness on tundra lakes using C-band synthetic aperture radar remote sensing. *JAWRA Journal of the American Water Resources Association*, 44(2):285–292.

Hochreiter, S. and Schmidhuber, J. (1997). Long short-term memory. *Neural computation*, 9(8):1735–1780.

Hodrick, R. J. and Prescott, E. C. (1997). Postwar US business cycles: an empirical investigation. *Journal of Money, credit, and Banking*, pages 1–16.

Holloway, J. and Mengersen, K. (2018). Statistical machine learning methods and remote sensing for sustainable development goals: a review. *Remote Sensing*, 10(1365):1–21.

Huang, L., Luo, J., Lin, Z., Niu, F., and Liu, L. (2020). Using deep learning to map retrogressive thaw slumps in the Beiluhe region (Tibetan Plateau) from CubeSat images. *Remote Sensing of Environment*, 237:1–13.

Huang, W., DeVries, B., Huang, C., Lang, M. W., Jones, J. W., Creed, I. F., and Carroll, M. L. (2018). Automated extraction of surface water extent from Sentinel-1 data. *Remote Sensing*, 10(5):797.

Hugelius, G., Strauss, J., Zubrzycki, S., Harden, J. W., Schuur, E. A. G., Ping, C. L., Schirrmeister, L., Grosse, G., Michaelson, G. J., Koven, C. D., O'Donnell, J. A., Elberling, B., Mishra, U., Camill, P., Yu, Z., Palmtag, J., and Kuhry, P. (2014). Estimated stocks of circumpolar permafrost carbon with quantified uncertainty ranges and identified data gaps. *Biogeosciences*, 11(23):6573–6593.

Ienco, D., Gaetano, R., Dupaquier, C., and Maurel, P. (2017). Land cover classification via multitemporal spatial data by deep recurrent neural networks. *IEEE Geoscience and Remote Sensing Letters*, 14(10):1685–1689.

Interdonato, R., Ienco, D., Gaetano, R., and Ose, K. (2019). DuPLO: A DUal view point deep learning architecture for time series classification. *ISPRS Journal of Photogrammetry and Remote Sensing*, 149:91–104.

Irving, W. N. and Cinq-Mars, J. (1974). A tentative archaeological sequence for Old Crow Flats, Yukon territory. *Arctic Anthropology*, pages 65–81.

Jeffries, M. O., Morris, K., and Duguay, C. R. (2005a). Lake ice growth and decay in central Alaska, USA: observations and computer simulations compared. *Annals of glaciology*, 40:195–199.

Jeffries, M. O., Morris, K., and Kozlenko, N. (2005b). Ice characteristics and processes, and remote sensing of frozen rivers and lakes. In Duguay, C. R. and Pietroniro, A., editors, *Remote Sensing in Northern Hydrology: measuring environmental change*, pages 63–90. American Geophysical Union.

Jeffries, M. O., Morris, K., and Liston, G. E. (1996). A method to determine lake depth and water availability on the North Slope of Alaska with spaceborne imaging radar and numerical ice growth modelling. *Arctic*, pages 367–374.

Ji, S., Zhang, C., Xu, A., Shi, Y., and Duan, Y. (2018). 3d convolutional neural networks for crop classification with multi-temporal remote sensing images. *Remote Sensing*, 10(1):1–17.

Jiang, Z., Von Ness, K., Loisel, J., and Wang, Z. (2019). ArcticNet: A deep learning solution to classify Arctic wetlands. *arXiv preprint arXiv:1906.00133*.

Jones, B. M. and Arp, C. D. (2015). Observing a catastrophic thermokarst lake drainage in northern Alaska. *Permafrost and Periglacial Processes*, 26(2):119–128.

Jones, B. M., Grosse, G., Arp, C., Jones, M., Anthony, K. W., and Romanovsky, V. (2011). Modern thermokarst lake dynamics in the continuous permafrost zone, northern Seward Peninsula, Alaska. *Journal of Geophysical Research: Biogeosciences*, 116:1–13.

Jones, B. M., Gusmeroli, A., Arp, C. D., Strozzi, T., Grosse, G., Gaglioti, B. V., and Whitman, M. S. (2013). Classification of freshwater ice conditions on the Alaskan Arctic Coastal Plain using ground penetrating radar and TerraSAR-X satellite data. *International Journal of Remote Sensing*, 34(23):8267–8279.

Jorgenson, M. T. and Grosse, G. (2016). Remote sensing of landscape change in permafrost regions. *Permafrost and periglacial processes*, 27(4):324–338.

Kang, K.-K., Duguay, C. R., Howell, S. E., Derksen, C. P., and Kelly, R. E. (2010). Sensitivity of AMSR-E brightness temperatures to the seasonal evolution of lake ice thickness. *IEEE Geoscience and Remote Sensing Letters*, 7(4):751–755.

Kheyrollah Pour, H., Duguay, C. R., Scott, K. A., and Kang, K.-K. (2017). Improvement of lake ice thickness retrieval from MODIS satellite data using a thermodynamic model. *IEEE Transactions on Geoscience and Remote Sensing*, 55(10):5956–5965.

Kokelj, S. V. and Jorgenson, M. T. (2013). Advances in thermokarst research. *Permafrost and Periglacial Processes*, 24(2):108–119.

Kozlenko, N. and Jeffries, M. O. (2000). Bathymetric mapping of shallow water in thaw lakes on the North Slope of Alaska with spaceborne imaging radar. *Arctic*, 53:306–316.

Labrecque, S., Lacelle, D., Duguay, C. R., Lauriol, B., and Hawkings, J. (2009). Contemporary (1951-2001) evolution of lakes in the Old Crow Basin, Northern Yukon, Canada: Remote sensing, numerical modeling, and stable isotope analysis. *Arctic*, 62:225–238.

Landgrebe, D. (1986). Early history of LARS. https://www.lars.purdue.edu/home/LARSHistory.html#fn0. Accessed: 2019-11-19.

Lantz, T. C. (2017). Vegetation succession and environmental conditions following catastrophic lake drainage in Old Crow Flats, Yukon. *Arctic*, 70:177–189.

Lantz, T. C. and Turner, K. W. (2015). Changes in lake area in response to thermokarst processes and climate in Old Crow Flats, Yukon. *Journal of Geophysical Research: Biogeosciences*, 120(3):513–524.

Lauriol, B., Lacelle, D., Labrecque, S., Duguay, C. R., and Telka, A. (2009). Holocene evolution of lakes in the Bluefish Basin, northern Yukon, Canada. *Arctic*, pages 212–224.

LeCun, Y., Bengio, Y., and Hinton, G. (2015). Deep learning. *nature*, 521(7553):436–444.

Lenormand, F., Duguay, C. R., and Gauthier, R. (2002). Development of a historical ice database for the study of climate change in Canada. *Hydrological Processes*, 16(18):3707–3722.

Leverington, D. W. and Duguay, C. R. (1996). Evaluation of three supervised classifiers in mapping "depth to late-summer frozen ground," Central Yukon Territory. *Canadian Journal of Remote Sensing*, 22(2):163–174.

Leverington, D. W. and Duguay, C. R. (1997). A neural network method to determine the presence or absence of permafrost near Mayo, Yukon Territory, Canada. *Permafrost and Periglacial Processes*, 8(2):205–215.

Lindgren, P. R., Grosse, G., Walter Anthony, K. M., and Meyer, F. J. (2016). Detection and spatiotemporal analysis of methane ebullition on thermokarst lake ice using high-resolution optical aerial imagery. *Biogeosciences*, 13(1):27–44.

Lynch-Stewart, P. and Associates (2008). Wetlands of international importance (Ramsar sites) in Canada. Report, Environment Canada.

Ma, L., Liu, Y., Zhang, X., Ye, Y., Yin, G., and Johnson, B. A. (2019). Deep learning in remote sensing applications: A meta-analysis and review. *ISPRS journal of photogrammetry and remote sensing*, 152:166–177.

MacDonald, L. A., Turner, K. W., Balasubramaniam, A. M., Wolfe, B. B., Hall, R. I., and Sweetman, J. N. (2012). Tracking hydrological responses of a thermokarst lake in the Old Crow Flats (Yukon Territory, Canada) to recent climate variability using aerial photographs and paleolimnological methods. *Hydrological Processes*, 26(1):117–129.

Mauro, N., Vergari, A., Basile, T. M. A., Ventola, F. G., and Esposito, F. (2017). End-to-end learning of deep spatio-temporal representations for satellite image time series classification. In *Proceedings of the 2017 European Conference on Machine Learning & Principles and Practice of Knowledge Discovery in Databases (ECML PKDD 2017)*, Skopje, North Macedonia.

Ménard, P., Duguay, C. R., Flato, G. M., and Rouse, W. R. (2002). Simulation of ice phenology on Great Slave Lake, Northwest Territories, Canada. *Hydrological Processes*, 16(18):3691–3706.

Meredith, M., Sommerkorn, M., Cassotta, S., Derksen, C., Ekaykin, A., Hollowed, A., Kofinas, G., Mackintosh, A., Melbourne-Thomas, J., Muelbert, M., et al. (2019). Polar regions. chapter 3, IPCC special report on the ocean and cryosphere in a changing climate.

Minh, D. H. T., Ienco, D., Gaetano, R., Lalande, N., Ndikumana, E., Osman, F., and Maurel, P. (2018). Deep recurrent neural networks for winter vegetation quality mapping via multitemporal SAR Sentinel-1. *IEEE Geoscience and Remote Sensing Letters*, 15(3):464–468.

Mommertz, R. (2019). Mapping bedfast and floating thermokarst lake ice and determining lake depth using Sentinel 1 synthetic aperture radar remote sensing on the west shore of Hudson Bay, Canada and Prudhoe Bay, Alaska. Master's thesis, Institute for Earth-and Environmental Science, University of Potsdam, Potsdam, Germany.

Ndikumana, E., Ho Tong Minh, D., Baghdadi, N., Courault, D., and Hossard, L. (2018). Deep recurrent neural network for agricultural classification using multitemporal SAR Sentinel-1 for Camargue, France. *Remote Sensing*, 10(8):1–16.

Nitze, I., Cooley, S. W., Duguay, C. R., Jones, B. M., and Grosse, G. (2020). The catastrophic thermokarst lake drainage events of 2018 in northwestern Alaska: fast-forward into the future. *The Cryosphere*, 14(12):4279–4297.

Nitze, I., Grosse, G., Jones, B. M., Arp, C. D., Ulrich, M., Fedorov, A., and Veremeeva, A. (2017). Landsat-based trend analysis of lake dynamics across northern permafrost regions. *Remote Sensing*, 9(7):1–28.

Ovenden, L. E. (1985). Hydroseral histories of the Old Crow peatlands, northern Yukon.

Pelletier, C., Webb, G. I., and Petitjean, F. (2019a). Deep learning for the classification of Sentinel-2 image time series. In *IGARSS 2019-2019 IEEE International Geoscience and Remote Sensing Symposium*, pages 461–464, Yokohama, Japan. IEEE.

Pelletier, C., Webb, G. I., and Petitjean, F. (2019b). Temporal convolutional neural network for the classification of satellite image time series. *Remote Sensing*, 11(5):1–25.

Pointner, G. and Bartsch, A. (2020). Interannual variability of lake ice backscatter anomalies on Lake Neyto, Yamal, Russia. *GI_Forum J*, 8:47–62.

Pointner, G., Bartsch, A., Forbes, B. C., and Kumpula, T. (2019). The role of lake size and local phenomena for monitoring ground-fast lake ice. *International journal of remote sensing*, 40(3):832–858.

Porter, T. J. and Pisaric, M. F. J. (2011). Temperature-growth divergence in white spruce forests of Old Crow Flats, Yukon Territory, and adjacent regions of northwestern North America. *Global Change Biology*, 17(11):3418–3430.

Romero, A., Gatta, C., and Camps-Valls, G. (2016). Unsupervised deep feature extraction for remote sensing image classification. *IEEE Transactions on Geoscience and Remote Sensing*, 54(3):1349–1362.

Rouse, W. R., Binyamin, J., Blanken, P. D., Bussières, N., Duguay, C. R., Oswald, C. J., Schertzer, W. M., and Spence, C. (2008). The influence of lakes on the regional energy

and water balance of the central Mackenzie River Basin. In *Cold region atmospheric and hydrologic studies. The Mackenzie GEWEX experience*, pages 309–325. Springer.

Roy-Léveillée, P. (2014). *Permafrost and thermokarst lake dynamics in the Old Crow Flats, northern Yukon, Canada*. PhD thesis, Carleton University, Ottawa, Canada.

Roy-Léveillée, P. and Burn, C. (2010). Permafrost conditions near shorelines of oriented lakes in Old Crow Flats, Yukon Territory. In *Conference Proceedings of GEO*, pages 1509–1516.

Roy-Léveillée, P., Burn, C. R., and McDonald, I. D. (2014). Vegetation-permafrost relations within the forest-tundra ecotone near Old Crow, Northern Yukon, Canada. *Permafrost and Periglacial Processes*, 25(2):127–135.

Roy-Roy-Léveillée, P. and Burn, C. R. (2015). Geometry of oriented lakes in Old Crow Flats, northern Yukon. In *Proceedings, 68th Canadian Geotechnical Conference and 7th Canadian Permafrost Conference*, pages 21–23, Quebec City, QC.

Roy-Roy-Léveillée, P. and Burn, C. R. (2017). Near-shore talik development beneath shallow water in expanding thermokarst lakes, Old Crow Flats, Yukon. *Journal of Geophysical Research: Earth Surface*, 122(5):1070–1089.

Scott, K. A., Xu, L., and Pour, H. K. (2020). Retrieval of ice/water observations from synthetic aperture radar imagery for use in lake ice data assimilation. *Journal of Great Lakes Research*, 46(6):1521–1532.

Sellmann, P., Weeks, W., and Campbell, W. (1975). Use of Side-looking Airborne Radar to

determine lake depth on the Alaskan North Slope. Technical Report Special Report No. 230, Cold Regions Research and Engineering Laboratory, Hanover, New Hampshire.

Siewert, M. B. (2018). High-resolution digital mapping of soil organic carbon in permafrost terrain using machine learning: a case study in a sub-Arctic peatland environment. *Biogeosciences*, 15(6):1663–1682.

Sun, Z., Di, L., and Fang, H. (2019). Using long short-term memory recurrent neural network in land cover classification on Landsat and cropland data layer time series. *International journal of remote sensing*, 40(2):593–614.

Surdu, C. M., Duguay, C. R., Brown, L. C., and Fernández Prieto, D. (2014). Response of ice cover on shallow lakes of the North Slope of Alaska to contemporary climate conditions (1950–2011): radar remote-sensing and numerical modeling data analysis. *The Cryosphere*, 8(1):167–180.

Swanson, D. K. (2019). Thermokarst and precipitation drive changes in the area of lakes and ponds in the national parks of northwestern Alaska, 1984–2018. *Arctic, Antarctic, and Alpine Research*, 51(1):265–279.

Tom, M., Aguilar, R., Imhof, P., Leinss, S., Baltsavias, E., and Schindler, K. (2020). Lake ice detection from Sentinel-1 SAR with deep learning. *arXiv preprint arXiv:2002.07040*.

Tondu, J.-m. (2012). An interdisciplinary approach to monitoring the hydroecology of thermokarst lakes in Old Crow Flats, Yukon Territory, Canada. Master's thesis, University of Waterloo.

Tsui, O. W., Chiang, M., and Dean, A. (2019). Mapping of bottomfast lake ice in the northwest territories via data mining of synthetic aperture radar image time series. *Canadian Journal of Remote Sensing*, 45(5):572–590.

Turner, K. W., Wolfe, B. B., and Edwards, T. W. D. (2010). Characterizing the role of hydrological processes on lake water balances in the Old Crow Flats, Yukon Territory, Canada, using water isotope tracers. *Journal of Hydrology*, 386(1-4):103–117.

Turner, K. W., Wolfe, B. B., Edwards, T. W. D., Lantz, T. C., Hall, R. I., and Larocque, G. (2014). Controls on water balance of shallow thermokarst lakes and their relations with catchment characteristics: a multi-year, landscape-scale assessment based on water isotope tracers and remote sensing in Old Crow Flats, Yukon (Canada). *Global change biology*, 20(5):1585–1603.

Valero, S., Pelletier, C., and Bertolino, M. (2016). Patch-based reconstruction of high resolution satellite image time series with missing values using spatial, spectral and temporal similarities. In *2016 IEEE International Geoscience and Remote Sensing Symposium (IGARSS)*, pages 2308–2311. IEEE.

van Huissteden, J. (2020). *Permafrost thawing: permafrost carbon in a warming Arctic*. Springer Nature Switzerland AG, Cham, Switzerland.

Wakabayashi, H. and Motohashi, K. (2018). Monitoring freezing and thawing of shallow lakes in Northern Alaska using Sentinel-1 data. In *IGARSS 2018-2018 IEEE International Geoscience and Remote Sensing Symposium*, pages 7157–7160. IEEE.

Wang, J. A., Sulla-Menashe, D., Woodcock, C. E., Sonnentag, O., Keeling, R. F., and Friedl, M. A. (2020). Extensive land cover change across Arctic–Boreal Northwestern North America from disturbance and climate forcing. *Global Change Biology*, 26(2):807–822.

Wang, L., Jolivel, M., Marzahn, P., Bernier, M., and Ludwig, R. (2018). Thermokarst pond dynamics in subarctic environment monitoring with radar remote sensing. *Permafrost and Periglacial Processes*, 29(4):231–245.

Wang, L., Scott, K. A., Clausi, D. A., and Xu, Y. (2017). Ice concentration estimation in the gulf of St. Lawrence using fully convolutional neural network. In *2017 IEEE International Geoscience and Remote Sensing Symposium (IGARSS)*, pages 4991–4994. IEEE.

Wang, L., Scott, K. A., Xu, L., and Clausi, D. A. (2016). Sea ice concentration estimation during melt from dual-pol SAR scenes using deep convolutional neural networks: A case study. *IEEE Transactions on Geoscience and Remote Sensing*, 54(8):4524–4533.

Wolfe, B. B., Humphries, M. M., Pisaric, M. F. J., Balasubramaniam, A. M., Burn, C. R., Chan, L., Cooley, D., Froese, D. G., Graupe, S., Hall, R. I., et al. (2011). Environmental change and traditional use of the Old Crow Flats in northern Canada: an IPY opportunity to meet the challenges of the new northern research paradigm. *Arctic*, 64(1):127–135.

Wu, Y., Duguay, C. R., and Xu, L. (2021). Assessment of machine learning classifiers for

global lake ice cover mapping from MODIS TOA reflectance data. *Remote Sensing of Environment*, 253:112206.

You, Y., Yang, M., Yu, Q., Pan, X., Guo, L., Wang, X., and Wu, Q. (2018). Factors influencing the reliability of grounded and floating ice distinguishing based on ground penetrating radar reflection amplitude. *Cold Regions Science and Technology*, 154:1–8.

Zazula, G. D., Duk-Rodkin, A., Schweger, C. E., and Morlan, R. E. (2004). Late Pleistocene chronology of glacial lake Old Crow and the north-west margin of the Laurentide Ice Sheet. In *Developments in Quaternary Sciences*, volume 2, pages 347–362. Elsevier.

Zhang, S., Pavelsky, T. M., Arp, C. D., and Yang, X. (2021). Remote sensing of lake ice phenology in Alaska. *Environmental Research Letters*, 16(6):064007.

Appendix

Appendix A

A.1 List of all the SAR scenes used in this thesis

Table 1: Sentinel 1 scenes used in this thesis. "RTC_ID" is the ID of the level 2 RTC products processed by ASF, "Pol." stands for Polarization, "A" stands for the ascending mode, and "D" stands for the descending mode.

ID	RTC_ID	Date	Mode	Pol.
2020/2021				
S1A_IW_GRDH_1SDV_20201003T024103 _20201003T024128_034626_040830_A1E2	S1A_IW_20201003T024103_ DVP_RTC30_G_spufem_6438	2020-10-03	A	VV
S1A_IW_GRDH_1SDV_20201010T155449 _20201010T155518_034736_040C01_10FA	S1A_IW_20201010T155449_ DVP_RTC30_G_spufem_74F6	2020-10-10	D	VV
S1A_IW_GRDH_1SDV_20201015T024103 _20201015T024128_034801_040E45_E188	S1A_IW_20201015T024103_ DVP_RTC30_G_spufem_8896	2020-10-15	A	VV

ID	RTC_ID	Date	Mode	Pol.
S1A_IW_GRDH_1SDV_20201022T155449 _20201022T155518_034911_041213_7DC9	S1A_IW_20201022T155449_ DVP_RTC30_G_spufem_79B1	2020-10-22	D	VV
S1A_IW_GRDH_1SDV_20201027T024103 _20201027T024128_034976_04144C_2BA3	S1A_IW_20201027T024103_ DVP_RTC30_G_spufem_53F6	2020-10-27	A	VV
S1A_IW_GRDH_1SDV_20201103T155449 _20201103T155518_035086_04181D_D250	S1A_IW_20201103T155449_ DVP_RTC30_G_spufem_7B4C	2020-11-03	D	VV
S1A_IW_GRDH_1SDV_20201108T024103 _20201108T024128_035151_041A53_82BF	S1A_IW_20201108T024103_ DVP_RTC30_G_spufem_F50D	2020-11-08	A	VV
S1A_IW_GRDH_1SDV_20201115T155449 _20201115T155518_035261_041E38_92BA	S1A_IW_20201115T155449_ DVP_RTC30_G_spufem_1888	2020-11-15	D	VV
S1A_IW_GRDH_1SDV_20201120T024103 _20201120T024128_035326_04206F_F96B	S1A_IW_20201120T024103_ DVP_RTC30_G_spufem_8E34	2020-11-20	A	VV
S1A_IW_GRDH_1SDV_20201127T155449 _20201127T155518_035436_042444_133E	S1A_IW_20201127T155449_ DVP_RTC30_G_spufem_3F40	2020-11-27	D	VV
S1A_IW_GRDH_1SDV_20201202T024102 _20201202T024127_035501_04267F_3FD2	S1A_IW_20201202T024102_ DVP_RTC30_G_spufem_7073	2020-12-02	A	VV
S1A_IW_GRDH_1SDV_20201209T155448 _20201209T155517_035611_042A52_7312	S1A_IW_20201209T155448_ DVP_RTC30_G_spufem_A4A2	2020-12-09	D	VV
S1A_IW_GRDH_1SDV_20201214T024102 _20201214T024127_035676_042C82_93E8	S1A_IW_20201214T024102_ DVP_RTC30_G_spufem_93D7	2020-12-14	A	VV

ID	RTC_ID	Date	Mode	Pol.
S1A_IW_GRDH_1SDV_20201221T155448 _20201221T155517_035786_043053_A03A	S1A_IW_20201221T155448_ DVP_RTC30_G_spufem_1087	2020-12-21	D	VV
S1A_IW_GRDH_1SDV_20201226T024101 _20201226T024126_035851_04328C_3F96	S1A_IW_20201226T024101_ DVP_RTC30_G_spufem_9836	2020-12-26	A	VV
S1A_IW_GRDH_1SDV_20210102T155447 _20210102T155516_035961_043667_951E	S1A_IW_20210102T155447_ DVP_RTC30_G_spufem_50D9	2021-01-02	D	VV
S1A_IW_GRDH_1SDV_20210107T024101 _20210107T024126_036026_0438A0_B2E9	S1A_IW_20210107T024101_ DVP_RTC30_G_spufem_B6D5	2021-01-07	A	VV
S1A_IW_GRDH_1SDV_20210114T155447 _20210114T155516_036136_043C92_EF33	S1A_IW_20210114T155447_ DVP_RTC30_G_spufem_6136	2021-01-14	D	VV
S1A_IW_GRDH_1SDV_20210119T024100 _20210119T024125_036201_043EC8_A246	S1A_IW_20210119T024100_ DVP_RTC30_G_spufem_0C13	2021-01-19	A	VV
S1A_IW_GRDH_1SDV_20210126T155446 _20210126T155515_036311_0442A3_D458	S1A_IW_20210126T155446_ DVR_RTC30_G_spufem_1D51	2021-01-26	D	VV
S1A_IW_GRDH_1SDV_20210131T024100 _20210131T024125_036376_0444D8_1CA5	S1A_IW_20210131T024100_ DVR_RTC30_G_spufem_A357	2021-01-31	A	VV
S1A_IW_GRDH_1SDV_20210207T155446 _20210207T155515_036486_0448B1_337F	S1A_IW_20210207T155446_ DVR_RTC30_G_spufem_5794	2021-02-07	D	VV
S1A_IW_GRDH_1SDV_20210212T024100 _20210212T024125_036551_044AED_24D7	S1A_IW_20210212T024100_ DVP_RTC30_G_spufem_73EA	2021-02-12	A	VV

ID	RTC_ID	Date	Mode	Pol.
S1A_IW_GRDH_1SDV_20210219T155445 _20210219T155514_036661_044ED0_019B	S1A_IW_20210219T155445_ DVR_RTC30_G_spufem_4EB1	2021-02-19	D	VV
S1A_IW_GRDH_1SDV_20210224T024059 _20210224T024124_036726_045105_272C	S1A_IW_20210224T024059_ DVR_RTC30_G_spufem_AC27	2021-02-24	A	VV
S1A_IW_GRDH_1SDV_20210303T155445 _20210303T155514_036836_0454DD_8D16	S1A_IW_20210303T155445_ DVR_RTC30_G_spufem_21EF	2021-03-03	D	VV
S1A_IW_GRDH_1SDV_20210308T024059 _20210308T024124_036901_04571F_78A3	S1A_IW_20210308T024059_ DVR_RTC30_G_spufem_4EFA	2021-03-08	A	VV
S1A_IW_GRDH_1SDV_20210315T155445 _20210315T155514_037011_045AFA_EBE0	S1A_IW_20210315T155445_ DVP_RTC30_G_spufem_0E57	2021-03-15	D	VV
2019/2020				
S1A_IW_GRDH_1SDV_20191004T155443 _20191004T155512_029311_0354C5_E4A3	S1A_IW_20191004T155443_ DVP_RTC30_G_saufem_D0E1	2019-10-04	D	VV
S1A_IW_GRDH_1SDV_20191009T024057 _20191009T024122_029376_035703_1A06	S1A_IW_20191009T024057_ DVP_RTC30_G_saufem_36C3	2019-10-09	A	VV
S1A_IW_GRDH_1SDV_20191011T154629 _20191011T154654_029413_03585F_D7B6	S1A_IW_20191011T154629_ DVP_RTC30_G_saufem_5F83	2019-10-11	D	VV
S1A_IW_GRDH_1SDV_20191016T155443 _20191016T155512_029486_035AD0_F446	S1A_IW_20191016T155443_ DVP_RTC30_G_saufem_D625	2019-10-16	D	VV
S1A_IW_GRDH_1SDV_20191021T024057 _20191021T024122_029551_035D0D_6ABF	S1A_IW_20191021T024057_ DVP_RTC30_G_saufem_CAD6	2019-10-21	A	VV

ID	RTC_ID	Date	Mode	Pol.
S1A_IW_GRDH_1SDV_20191023T154629 _20191023T154654_029588_035E5F_F9E0	S1A_IW_20191023T154629_ DVP_RTC30_G_saufem_EC76	2019-10-23	D	VV
S1A_IW_GRDH_1SDV_20191028T155443 _20191028T155512_029661_0360DA_E72E	S1A_IW_20191028T155443_ DVP_RTC30_G_saufem_3A8A	2019-10-28	D	VV
S1A_IW_GRDH_1SDV_20191102T024057 _20191102T024122_029726_036320_0801	S1A_IW_20191102T024057_ DVP_RTC30_G_saufem_BDEC	2019-11-02	A	VV
S1A_IW_GRDH_1SDV_20191104T154629 _20191104T154654_029763_036480_36D1	S1A_IW_20191104T154629_ DVP_RTC30_G_saufem_D4C4	2019-11-04	D	VV
S1A_IW_GRDH_1SDV_20191109T155443 _20191109T155512_029836_036708_44BC	S1A_IW_20191109T155443_ DVP_RTC30_G_saufem_17A6	2019-11-09	D	VV
S1A_IW_GRDH_1SDV_20191114T024057 _20191114T024122_029901_036946_BB73	S1A_IW_20191114T024057_ DVP_RTC30_G_saufem_541E	2019-11-14	A	VV
S1A_IW_GRDH_1SDV_20191116T154629 _20191116T154654_029938_036AA5_3604	S1A_IW_20191116T154629_ DVP_RTC30_G_saufem_7DCB	2019-11-16	D	VV
S1A_IW_GRDH_1SDV_20191121T155443 _20191121T155512_030011_036D12_E962	S1A_IW_20191121T155443_ DVP_RTC30_G_saufem_C790	2019-11-21	D	VV
S1A_IW_GRDH_1SDV_20191126T024057 _20191126T024122_030076_036F57_36B7	S1A_IW_20191126T024057_ DVP_RTC30_G_saufem_259F	2019-11-26	A	VV
S1A_IW_GRDH_1SDV_20191128T154628 _20191128T154653_030113_0370B7_232C	S1A_IW_20191128T154628_ DVP_RTC30_G_saufem_7B36	2019-11-28	D	VV

ID	RTC_ID	Date	Mode	Pol.
S1A_IW_GRDH_1SDV_20191203T155442 _20191203T155511_030186_037324_E8D8	S1A_IW_20191203T155442_ DVP_RTC30_G_saufem_80BF	2019-12-03	D	VV
S1A_IW_GRDH_1SDV_20191208T024056 _20191208T024121_030251_037557_0900	S1A_IW_20191208T024056_ DVP_RTC30_G_saufem_8AF4	2019-12-08	A	VV
S1A_IW_GRDH_1SDV_20191210T154628 _20191210T154653_030288_0376BC_B12D	S1A_IW_20191210T154628_ DVP_RTC30_G_saufem_DB4C	2019-12-10	D	VV
S1A_IW_GRDH_1SDV_20191215T155442 _20191215T155511_030361_03792F_565C	S1A_IW_20191215T155442_ DVP_RTC30_G_saufem_DB39	2019-12-15	D	VV
S1A_IW_GRDH_1SDV_20191220T024056 _20191220T024121_030426_037B66_335D	S1A_IW_20191220T024056_ DVP_RTC30_G_saufem_4E02	2019-12-20	A	VV
S1A_IW_GRDH_1SDV_20191222T154628 _20191222T154653_030463_037CC6_22F6	S1A_IW_20191222T154628_ DVP_RTC30_G_saufem_4507	2019-12-22	D	VV
S1A_IW_GRDH_1SDV_20191227T155441 _20191227T155510_030536_037F38_4278	S1A_IW_20191227T155441_ DVP_RTC30_G_saufem_38F3	2019-12-27	D	VV
S1A_IW_GRDH_1SDV_20200101T024055 _20200101T024120_030601_038171_1A01	S1A_IW_20200101T024055_ DVP_RTC30_G_saufem_6D4F	2020-01-01	A	VV
S1A_IW_GRDH_1SDV_20200103T154627 _20200103T154652_030638_0382CF_6A29	S1A_IW_20200103T154627_ DVP_RTC30_G_saufem_166B	2020-01-03	D	VV
S1A_IW_GRDH_1SDV_20200108T155441 _20200108T155510_030711_038548_6343	S1A_IW_20200108T155441_ DVP_RTC30_G_saufem_64B1	2020-01-08	D	VV

ID	RTC_ID	Date	Mode	Pol.
S1A_IW_GRDH_1SDV_20200113T024055 _20200113T024120_030776_038785_A71A	S1A_IW_20200113T024055_ DVP_RTC30_G_saufem_C30F	2020-01-13	A	VV
S1A_IW_GRDH_1SDV_20200115T154626 _20200115T154651_030813_0388ED_43D6	S1A_IW_20200115T154626_ DVP_RTC30_G_saufem_9BA2	2020-01-15	D	VV
S1A_IW_GRDH_1SDV_20200120T155440 _20200120T155509_030886_038B6E_C898	S1A_IW_20200120T155440_ DVP_RTC30_G_saufem_749A	2020-01-20	D	VV
S1A_IW_GRDH_1SDV_20200125T024054 _20200125T024119_030951_038DB0_EA97	S1A_IW_20200125T024054_ DVP_RTC30_G_saufem_D38B	2020-01-25	A	VV
S1A_IW_GRDH_1SDV_20200127T154626 _20200127T154651_030988_038F17_AA3C	S1A_IW_20200127T154626_ DVP_RTC30_G_saufem_CA68	2020-01-27	D	VV
S1A_IW_GRDH_1SDV_20200201T155440 _20200201T155509_031061_039188_8CD1	S1A_IW_20200201T155440_ DVP_RTC30_G_saufem_6CE7	2020-02-01	D	VV
S1A_IW_GRDH_1SDV_20200206T024054 _20200206T024119_031126_0393CB_7397	S1A_IW_20200206T024054_ DVP_RTC30_G_saufem_FD5A	2020-02-06	A	VV
S1A_IW_GRDH_1SDV_20200208T154626 _20200208T154651_031163_039536_FEB0	S1A_IW_20200208T154626_ DVP_RTC30_G_saufem_1A2F	2020-02-08	D	VV
S1A_IW_GRDH_1SDV_20200213T155440 _20200213T155509_031236_03979A_B3DC	S1A_IW_20200213T155440_ DVP_RTC30_G_saufem_567E	2020-02-13	D	VV
S1A_IW_GRDH_1SDV_20200218T024054 _20200218T024119_031301_0399DC_CE0C	S1A_IW_20200218T024054_ DVP_RTC30_G_saufem_2D77	2020-02-18	A	VV

ID	RTC_ID	Date	Mode	Pol.
S1A_IW_GRDH_1SDV_20200220T154626 _20200220T154651_031338_039B39_7889	S1A_IW_20200220T154626_ DVP_RTC30_G_saufem_6FFB	2020-02-20	D	VV
S1A_IW_GRDH_1SDV_20200225T155439 _20200225T155508_031411_039DA6_8BCE	S1A_IW_20200225T155439_ DVP_RTC30_G_saufem_F23A	2020-02-25	D	VV
S1A_IW_GRDH_1SDV_20200301T024053 _20200301T024118_031476_039FD9_C85C	S1A_IW_20200301T024053_ DVP_RTC30_G_saufem_CDF0	2020-03-01	A	VV
S1A_IW_GRDH_1SDV_20200303T154625 _20200303T154650_031513_03A145_DE58	S1A_IW_20200303T154625_ DVP_RTC30_G_saufem_A8B9	2020-03-03	D	VV
S1A_IW_GRDH_1SDV_20200308T155440 _20200308T155509_031586_03A3B0_BBCE	S1A_IW_20200308T155440_ DVP_RTC30_G_saufem_0A1F	2020-03-08	D	VV
S1A_IW_GRDH_1SDV_20200313T024054 _20200313T024119_031651_03A5EC_66E3	S1A_IW_20200313T024054_ DVP_RTC30_G_saufem_AA4C	2020-03-13	A	VV
20‘8/2019				
S1A_IW_GRDH_1SDV_20181004T154622 _20181004T154647_023988_029EDD_4F4B	S1A_IW_20181004T154622_ DVP_RTC30_G_saufem_69C3	2018-10-04	D	VV
S1A_IW_GRDH_1SDV_20181009T155437 _20181009T155506_024061_02A12A_DA0D	S1A_IW_20181009T155437_ DVP_RTC30_G_saufem_FE2A	2018-10-09	D	VV
S1A_IW_GRDH_1SDV_20181014T024051 _20181014T024116_024126_02A349_9235	S1A_IW_20181014T024051_ DVP_RTC30_G_saufem_DFA6	2018-10-14	A	VV
S1A_IW_GRDH_1SDV_20181016T154623 _20181016T154648_024163_02A48F_67F9	S1A_IW_20181016T154623_ DVP_RTC30_G_saufem_1C91	2018-10-16	D	VV

ID	RTC_ID	Date	Mode	Pol.
S1A_IW_GRDH_1SDV_20181021T155437 _20181021T155506_024236_02A6DA_23CB	S1A_IW_20181021T155437_ DVP_RTC30_G_saufem_12B4	2018-10-21	D	VV
S1A_IW_GRDH_1SDV_20181026T024051 _20181026T024116_024301_02A8EF_9BA8	S1A_IW_20181026T024051_ DVP_RTC30_G_saufem_4CF6	2018-10-26	A	VV
S1A_IW_GRDH_1SDV_20181028T154623 _20181028T154648_024338_02AA32_384E	S1A_IW_20181028T154623_ DVP_RTC30_G_saufem_5EC1	2018-10-28	D	VV
S1A_IW_GRDH_1SDV_20181102T155437 _20181102T155506_024411_02ACA5_49A8	S1A_IW_20181102T155437_ DVP_RTC30_G_saufem_E7EC	2018-11-02	D	VV
S1A_IW_GRDH_1SDV_20181107T024050 _20181107T024115_024476_02AEF9_2D2B	S1A_IW_20181107T024050_ DVP_RTC30_G_saufem_86FA	2018-11-07	A	VV
S1A_IW_GRDH_1SDV_20181109T154622 _20181109T154647_024513_02B068_CCA7	S1A_IW_20181109T154622_ DVP_RTC30_G_saufem_BECF	2018-11-09	D	VV
S1A_IW_GRDH_1SDV_20181114T155436 _20181114T155505_024586_02B30F_10F6	S1A_IW_20181114T155436_ DVP_RTC30_G_saufem_D610	2018-11-14	D	VV
S1A_IW_GRDH_1SDV_20181119T024050 _20181119T024115_024651_02B56B_FC5C	S1A_IW_20181119T024050_ DVP_RTC30_G_saufem_22D4	2018-11-19	A	VV
S1A_IW_GRDH_1SDV_20181121T154622 _20181121T154647_024688_02B6DA_F099	S1A_IW_20181121T154622_ DVP_RTC30_G_saufem_A5D6	2018-11-21	D	VV
S1A_IW_GRDH_1SDV_20181126T155436 _20181126T155505_024761_02B97E_5604	S1A_IW_20181126T155436_ DVP_RTC30_G_saufem_0327	2018-11-26	D	VV

ID	RTC_ID	Date	Mode	Pol.
S1A_IW_GRDH_1SDV_20181201T024050 _20181201T024115_024826_02BBA6_E53D	S1A_IW_20181201T024050_ DVP_RTC30_G_saufem_4CEE	2018-12-01	A	VV
S1A_IW_GRDH_1SDV_20181203T154622 _20181203T154647_024863_02BCED_6FB4	S1A_IW_20181203T154622_ DVP_RTC30_G_saufem_E491	2018-12-03	D	VV
S1A_IW_GRDH_1SDV_20181208T155436 _20181208T155505_024936_02BF56_0ACB	S1A_IW_20181208T155436_ DVP_RTC30_G_saufem_8503	2018-12-08	D	VV
S1A_IW_GRDH_1SDV_20181215T154621 _20181215T154646_025038_02C31A_8F7F	S1A_IW_20181215T154621_ DVP_RTC30_G_saufem_4F9E	2018-12-15	D	VV
S1A_IW_GRDH_1SDV_20181220T155435 _20181220T155504_025111_02C5AC_F2B4	S1A_IW_20181220T155435_ DVP_RTC30_G_saufem_1A16	2018-12-20	D	VV
S1A_IW_GRDH_1SDV_20181227T154621 _20181227T154646_025213_02C972_86B3	S1A_IW_20181227T154621_ DVP_RTC30_G_saufem_CD91	2018-12-27	D	VV
S1A_IW_GRDH_1SDV_20190101T155435 _20190101T155504_025286_02CC00_96ED	S1A_IW_20190101T155435_ DVP_RTC30_G_saufem_5C82	2019-01-01	D	VV
S1A_IW_GRDH_1SDV_20190106T024048 _20190106T024113_025351_02CE58_7B1C	S1A_IW_20190106T024048_ DVP_RTC30_G_saufem_7E01	2019-01-06	A	VV
S1A_IW_GRDH_1SDV_20190108T154620 _20190108T154645_025388_02CFC4_324F	S1A_IW_20190108T154620_ DVP_RTC30_G_saufem_E5F1	2019-01-08	D	VV
S1A_IW_GRDH_1SDV_20190113T155434 _20190113T155503_025461_02D249_D8A8	S1A_IW_20190113T155434_ DVP_RTC30_G_saufem_AE20	2019-01-13	D	VV

ID	RTC_ID	Date	Mode	Pol.
S1A_IW_GRDH_1SDV_20190118T024048 _20190118T024113_025526_02D4A8_05CB	S1A_IW_20190118T024048_ DVP_RTC30_G_saufem_4871	2019-01-18	A	VV
S1A_IW_GRDH_1SDV_20190120T154620 _20190120T154645_025563_02D61E_691A	S1A_IW_20190120T154620_ DVP_RTC30_G_saufem_4713	2019-01-20	D	VV
S1A_IW_GRDH_1SDV_20190125T155434 _20190125T155503_025636_02D8AE_A125	S1A_IW_20190125T155434_ DVP_RTC30_G_saufem_8249	2019-01-25	D	VV
S1A_IW_GRDH_1SDV_20190201T154620 _20190201T154645_025738_02DC7E_E567	S1A_IW_20190201T154620_ DVP_RTC30_G_saufem_6936	2019-02-01	D	VV
S1A_IW_GRDH_1SDV_20190206T155433 _20190206T155502_025811_02DEF5_0DEE	S1A_IW_20190206T155433_ DVP_RTC30_G_saufem_EBA4	2019-02-06	D	VV
S1A_IW_GRDH_1SDV_20190213T154619 _20190213T154644_025913_02E2B1_23E5	S1A_IW_20190213T154619_ DVP_RTC30_G_saufem_D4FF	2019-02-13	D	VV
S1A_IW_GRDH_1SDV_20190218T155433 _20190218T155502_025986_02E534_AD9A	S1A_IW_20190218T155433_ DVP_RTC30_G_saufem_F75F	2019-02-18	D	VV
S1A_IW_GRDH_1SDV_20190223T024047 _20190223T024112_026051_02E791_E8EA	S1A_IW_20190223T024047_ DVP_RTC30_G_saufem_59D3	2019-02-23	A	VV
S1A_IW_GRDH_1SDV_20190225T154619 _20190225T154644_026088_02E8F6_CBEC	S1A_IW_20190225T154619_ DVP_RTC30_G_saufem_9FE1	2019-02-25	D	VV
S1A_IW_GRDH_1SDV_20190302T155433 _20190302T155502_026161_02EB7D_2686	S1A_IW_20190302T155433_ DVP_RTC30_G_saufem_EF29	2019-03-02	D	VV

ID	RTC_ID	Date	Mode	Pol.
S1A_IW_GRDH_1SDV_20190307T024047 _20190307T024112_026226_02EDD1_EE85	S1A_IW_20190307T024047_ DVP_RTC30_G_saufem_869C	2019-03-07	A	VV
S1A_IW_GRDH_1SDV_20190309T154619 _20190309T154644_026263_02EF46_25E3	S1A_IW_20190309T154619_ DVP_RTC30_G_saufem_3DAD	2019-03-09	D	VV
S1A_IW_GRDH_1SDV_20190314T155433 _20190314T155502_026336_02F1E0_ED8B	S1A_IW_20190314T155433_ DVP_RTC30_G_saufem_F0F7	2019-03-14	D	VV
2017/2018				
S1A_IW_GRDH_1SDV_20171002T155430 _20171002T155459_018636_01F6CA_E95B	S1A_IW_20171002T155430_ DVP_RTC30_G_saufem_7A79	2017-10-02	D	VV
S1A_IW_GRDH_1SDV_20171009T154616 _20171009T154641_018738_01F9E9_DACA	S1A_IW_20171009T154616_ DVP_RTC30_G_saufem_4787	2017-10-09	D	VV
S1A_IW_GRDH_1SDV_20171014T155430 _20171014T155459_018811_01FC1A_9DD3	S1A_IW_20171014T155430_ DVP_RTC30_G_saufem_72B4	2017-10-14	D	VV
S1A_IW_GRDH_1SDV_20171021T154616 _20171021T154641_018913_01FF4E_6113	S1A_IW_20171021T154616_ DVP_RTC30_G_saufem_F613	2017-10-21	D	VV
S1A_IW_GRDH_1SDV_20171026T155430 _20171026T155459_018986_020169_8B5C	S1A_IW_20171026T155430_ DVP_RTC30_G_saufem_1A1B	2017-10-26	D	VV
S1A_IW_GRDH_1SDV_20171102T154616 _20171102T154641_019088_02049D_22AF	S1A_IW_20171102T154616_ DVP_RTC30_G_saufem_E2A1	2017-11-02	D	VV
S1A_IW_GRDH_1SDV_20171107T155430 _20171107T155459_019161_0206D6_FB01	S1A_IW_20171107T155430_ DVP_RTC30_G_saufem_497D	2017-11-07	D	VV

ID	RTC_ID	Date	Mode	Pol.
S1A_IW_GRDH_1SDV_20171112T024044 _20171112T024109_019226_0208EA_D126	S1A_IW_20171112T024044_ DVP_RTC30_G_saufem_63CB	2017-11-12	A	VV
S1A_IW_GRDH_1SDV_20171114T154616 _20171114T154641_019263_020A12_5AE5	S1A_IW_20171114T154616_ DVP_RTC30_G_saufem_8176	2017-11-14	D	VV
S1A_IW_GRDH_1SDV_20171119T155430 _20171119T155459_019336_020C52_5529	S1A_IW_20171119T155430_ DVP_RTC30_G_saufem_83C6	2017-11-19	D	VV
S1A_IW_GRDH_1SDV_20171124T024044 _20171124T024109_019401_020E71_5270	S1A_IW_20171124T024044_ DVP_RTC30_G_saufem_E5AD	2017-11-24	A	VV
S1A_IW_GRDH_1SDV_20171126T154616 _20171126T154641_019438_020F9C_0FE1	S1A_IW_20171126T154616_ DVP_RTC30_G_saufem_EA49	2017-11-26	D	VV
S1A_IW_GRDH_1SDV_20171201T155429 _20171201T155458_019511_0211CB_3FBC	S1A_IW_20171201T155429_ DVP_RTC30_G_saufem_90AD	2017-12-01	D	VV
S1A_IW_GRDH_1SDV_20171206T024043 _20171206T024108_019576_0213EF_B147	S1A_IW_20171206T024043_ DVP_RTC30_G_saufem_1B87	2017-12-06	A	VV
S1A_IW_GRDH_1SDV_20171208T154615 _20171208T154640_019613_02150F_4469	S1A_IW_20171208T154615_ DVP_RTC30_G_saufem_9B69	2017-12-08	D	VV
S1A_IW_GRDH_1SDV_20171213T155429 _20171213T155458_019686_021746_B3AB	S1A_IW_20171213T155429_ DVP_RTC30_G_saufem_F5F6	2017-12-13	D	VV
S1A_IW_GRDH_1SDV_20171220T154615 _20171220T154640_019788_021A83_6948	S1A_IW_20171220T154615_ DVP_RTC30_G_saufem_EEFD	2017-12-20	D	VV

ID	RTC_ID	Date	Mode	Pol.
S1A_IW_GRDH_1SDV_20171225T155428 _20171225T155457_019861_021CAB_F1EF	S1A_IW_20171225T155428_ DVP_RTC30_G_saufem_7E81	2017-12-25	D	VV
S1A_IW_GRDH_1SDV_20171230T024042 _20171230T024107_019926_021ECA_386F	S1A_IW_20171230T024042_ DVP_RTC30_G_saufem_B6EB	2017-12-30	A	VV
S1A_IW_GRDH_1SDV_20180101T154614 _20180101T154639_019963_021FF5_3A60	S1A_IW_20180101T154614_ DVP_RTC30_G_saufem_8ABB	2018-01-01	D	VV
S1A_IW_GRDH_1SDV_20180106T155428 _20180106T155457_020036_022237_6F74	S1A_IW_20180106T155428_ DVP_RTC30_G_saufem_60AD	2018-01-06	D	VV
S1A_IW_GRDH_1SDV_20180111T024042 _20180111T024107_020101_022451_B04C	S1A_IW_20180111T024042_ DVP_RTC30_G_saufem_0178	2018-01-11	A	VV
S1A_IW_GRDH_1SDV_20180113T154614 _20180113T154639_020138_02257E_C744	S1A_IW_20180113T154614_ DVP_RTC30_G_saufem_E89D	2018-01-13	D	VV
S1A_IW_GRDH_1SDV_20180118T155427 _20180118T155456_020211_0227C3_3716	S1A_IW_20180118T155427_ DVP_RTC30_G_saufem_CD06	2018-01-18	D	VV
S1A_IW_GRDH_1SDV_20180123T024041 _20180123T024106_020276_0229DF_69DF	S1A_IW_20180123T024041_ DVP_RTC30_G_saufem_286C	2018-01-23	A	VV
S1A_IW_GRDH_1SDV_20180125T154613 _20180125T154638_020313_022B0A_23E5	S1A_IW_20180125T154613_ DVP_RTC30_G_saufem_E488	2018-01-25	D	VV
S1A_IW_GRDH_1SDV_20180130T155427 _20180130T155456_020386_022D53_8FFA	S1A_IW_20180130T155427_ DVP_RTC30_G_saufem_CE41	2018-01-30	D	VV

ID	RTC_ID	Date	Mode	Pol.
S1A_IW_GRDH_1SDV_20180204T024041 _20180204T024106_020451_022F75_7FD1	S1A_IW_20180204T024041_ DVP_RTC30_G_saufem_F95A	2018-02-04	A	VV
S1A_IW_GRDH_1SDV_20180206T154613 _20180206T154638_020488_0230A0_ACE0	S1A_IW_20180206T154613_ DVP_RTC30_G_saufem_C3E3	2018-02-06	D	VV
S1A_IW_GRDH_1SDV_20180211T155427 _20180211T155456_020561_0232EA_552F	S1A_IW_20180211T155427_ DVP_RTC30_G_saufem_F1B9	2018-02-11	D	VV
S1A_IW_GRDH_1SDV_20180218T154613 _20180218T154638_020663_023635_E316	S1A_IW_20180218T154613_ DVP_RTC30_G_saufem_D71E	2018-02-18	D	VV
S1A_IW_GRDH_1SDV_20180223T155427 _20180223T155456_020736_02387F_0116	S1A_IW_20180223T155427_ DVP_RTC30_G_saufem_9BB2	2018-02-23	D	VV
S1A_IW_GRDH_1SDV_20180302T154613 _20180302T154638_020838_023BC1_9034	S1A_IW_20180302T154613_ DVP_RTC30_G_saufem_1E33	2018-03-02	D	VV
S1A_IW_GRDH_1SDV_20180307T155427 _20180307T155456_020911_023E09_5810	S1A_IW_20180307T155427_ DVP_RTC30_G_saufem_7DC3	2018-03-07	D	VV
S1A_IW_GRDH_1SDV_20180312T024041 _20180312T024106_020976_024022_0A7E	S1A_IW_20180312T024041_ DVP_RTC30_G_saufem_EB70	2018-03-12	A	VV
S1A_IW_GRDH_1SDV_20180314T154613 _20180314T154638_021013_02414E_8B2D	S1A_IW_20180314T154613_ DVP_RTC30_G_saufem_CE44	2018-03-14	D	VV

Table 2: ERS 1/2 scenes used in this thesis. "Pol." stands for Polarization, "A" stands for the ascending mode, and "D" stands for the descending mode.

ID	Date	Mode	Pol.
2009/2010			
E2_75382_STD_F171	2009-09-20	A	VV
E2_75519_STD_F279	2009-09-29	D	VV
E2_75748_STD_F279	2009-10-15	D	VV
E2_75791_STD_F279	2009-10-18	D	VV
E2_75977_STD_F279	2009-10-31	D	VV
E2_76020_STD_F279	2009-11-03	D	VV
E2_76063_STD_F279	2009-11-06	D	VV
E2_76249_STD_F279	2009-11-19	D	VV
E2_76292_STD_F279	2009-11-22	D	VV
E2_76521_STD_F279	2009-12-08	D	VV
E2_76564_STD_F279	2009-12-11	D	VV
E2_76750_STD_F279	2009-12-24	D	VV
E2_76793_STD_F279	2009-12-27	D	VV
E2_76979_STD_F279	2010-01-09	D	VV
E2_77065_STD_F279	2010-01-15	D	VV
E2_77208_STD_F279	2010-01-25	D	VV
E2_77251_STD_F279	2010-01-28	D	VV
E2_77294_STD_F279	2010-01-31	D	VV

ID	Date	Mode	Pol.
E2_77386_STD_F172	2010-02-07	A	VV
E2_77480_STD_F279	2010-02-13	D	VV
E2_77523_STD_F279	2010-02-16	D	VV
E2_77566_STD_F279	2010-02-19	D	VV
E2_77572_STD_F171	2010-02-20	A	VV
E2_77658_STD_F172	2010-02-26	A	VV
E2_77709_STD_F279	2010-03-01	D	VV
E2_77752_STD_F279	2010-03-04	D	VV
E2_77795_STD_F279	2010-03-07	D	VV
E2_77844_STD_F171	2010-03-11	A	VV
E2_77930_STD_F172	2010-03-17	A	VV
E2_78024_STD_F279	2010-03-23	D	VV
E2_78067_STD_F279	2010-03-26	A	VV
E2_78116_STD_F171	2010-03-30	A	VV
2008/2009			
E2_70237_STD_F279	2008-09-25	D	VV
E2_70280_STD_F278	2008-09-28	D	VV
E2_70552_STD_F279	2008-10-17	D	VV
E2_70738_STD_F279	2008-10-30	D	VV
E2_70781_STD_F279	2008-11-02	D	VV
E2_71010_STD_F279	2008-11-18	D	VV

ID	Date	Mode	Pol.
E2_71053_STD_F279	2008-11-21	D	VV
E2_71239_STD_F279	2008-12-04	D	VV
E2_71282_STD_F279	2008-12-07	D	VV
E2_71468_STD_F279	2008-12-20	D	VV
E2_71511_STD_F279	2008-12-23	D	VV
E2_71554_STD_F279	2008-12-26	D	VV
E2_71740_STD_F279	2009-01-08	D	VV
E2_71783_STD_F279	2009-01-11	D	VV
E2_71969_STD_F279	2009-01-24	D	VV
E2_72012_STD_F279	2009-01-27	D	VV
E2_72055_STD_F279	2009-01-30	D	VV
E2_72198_STD_F279	2009-02-09	D	VV
E2_72241_STD_F279	2009-02-12	D	VV
E2_72284_STD_F279	2009-02-15	D	VV
E2_72376_STD_F171	2009-02-22	A	VV
E2_72470_STD_F279	2009-02-28	D	VV
E2_72513_STD_F279	2009-03-03	D	VV
E2_72556_STD_F279	2009-03-06	D	VV
E2_72699_STD_F279	2009-03-16	D	VV
E2_72742_STD_F279	2009-03-19	D	VV
1995/1996			

ID	Date	Mode	Pol.
E1_21817_STD_F279	1995-09-16	D	VV
E1_22003_STD_F279	1995-09-29	D	VV
E1_22046_STD_F279	1995-10-02	D	VV
E2_02373_STD_F279	1995-10-03	D	VV
E1_22089_STD_F279	1995-10-05	D	VV
E1_22095_STD_F171	1995-10-06	A	VV
E2_02422_STD_F171	1995-10-07	A	VV
E1_22232_STD_F279	1995-10-15	D	VV
E1_22275_STD_F279	1995-10-18	D	VV
E2_02602_STD_F279	1995-10-19	D	VV
E1_22318_STD_F279	1995-10-21	D	VV
E2_02645_STD_F279	1995-10-22	D	VV
E1_22504_STD_F279	1995-11-03	D	VV
E2_02831_STD_F279	1995-11-04	D	VV
E1_22547_STD_F279	1995-11-06	D	VV
E2_02874_STD_F279	1995-11-07	D	VV
E1_22590_STD_F279	1995-11-09	D	VV
E2_02917_STD_F279	1995-11-10	D	VV
E1_22776_STD_F279	1995-11-22	D	VV
E2_03103_STD_F279	1995-11-23	D	VV
E1_22819_STD_F279	1995-11-25	D	VV

ID	Date	Mode	Pol.
E2_03146_STD_F279	1995-11-26	D	VV
E1_23005_STD_F279	1995-12-08	D	VV
E2_03332_STD_F279	1995-12-09	D	VV
E1_23048_STD_F279	1995-12-11	D	VV
E2_03375_STD_F279	1995-12-12	D	VV
E2_03418_STD_F279	1995-12-15	D	VV
E1_23234_STD_F279	1995-12-24	D	VV
E2_03561_STD_F279	1995-12-25	D	VV
E1_23277_STD_F279	1995-12-27	D	VV
E2_03604_STD_F279	1995-12-28	D	VV
E1_23320_STD_F279	1995-12-30	D	VV
E2_03647_STD_F279	1995-12-31	D	VV
E1_23506_STD_F279	1996-01-12	D	VV
E2_03833_STD_F279	1996-01-13	D	VV
E1_23592_STD_F279	1996-01-18	D	VV
E2_03919_STD_F279	1996-01-19	D	VV
E1_23956_STD_F171	1996-02-13	A	VV
E2_04283_STD_F171	1996-02-14	A	VV
E1_24007_STD_F279	1996-02-16	D	VV
E2_04334_STD_F279	1996-02-17	D	VV
E1_24050_STD_F279	1996-02-19	D	VV

ID	Date	Mode	Pol.
E2_04377_STD_F279	1996-02-20	D	VV
E1_24093_STD_F279	1996-02-22	D	VV
E1_24099_STD_F171	1996-02-23	A	VV
E1_24142_STD_F171	1996-02-26	A	VV
E2_04469_STD_F171	1996-02-27	A	VV
E1_24185_STD_F171	1996-02-29	A	VV
E1_24236_STD_F279	1996-03-03	D	VV
E1_24371_STD_F171	1996-03-13	A	VV
E2_04698_STD_F171	1996-03-14	A	VV
E1_24414_STD_F171	1996-03-16	A	VV
1994/1995			
E1_16571_STD_F279	1994-09-15	D	VV
E1_16772_STD_F279	1994-09-29	D	VV
E1_16815_STD_F279	1994-10-02	D	VV
E1_16858_STD_F279	1994-10-05	D	VV
E1_17016_STD_F279	1994-10-16	D	VV
E1_17059_STD_F279	1994-10-19	D	VV
E1_17102_STD_F279	1994-10-22	D	VV
E1_17145_STD_F279	1994-10-25	D	VV
E1_17303_STD_F279	1994-11-05	D	VV
E1_17346_STD_F279	1994-11-08	D	VV

ID	Date	Mode	Pol.
E1_17389_STD_F279	1994-11-11	D	VV
E1_17547_STD_F279	1994-11-22	D	VV
E1_17590_STD_F279	1994-11-25	D	VV
E1_17633_STD_F279	1994-11-28	D	VV
E1_17676_STD_F279	1994-12-01	D	VV
E1_17834_STD_F279	1994-12-12	D	VV
E1_17920_STD_F279	1994-12-18	D	VV
E1_17998_STD_F171	1994-12-24	A	VV
E1_18041_STD_F171	1994-12-27	A	VV
E1_18121_STD_F279	1995-01-01	D	VV
E1_18164_STD_F279	1995-01-04	D	VV
E1_18207_STD_F279	1995-01-07	D	VV
E1_18365_STD_F279	1995-01-18	D	VV
E1_18408_STD_F279	1995-01-21	D	VV
E1_18451_STD_F279	1995-01-24	D	VV
E1_18652_STD_F279	1995-02-07	D	VV
E1_18695_STD_F279	1995-02-10	D	VV
E1_18738_STD_F279	1995-02-13	D	VV
E1_18816_STD_F171	1995-02-19	A	VV
E1_18896_STD_F279	1995-02-24	D	VV
E1_18939_STD_F279	1995-02-27	D	VV

ID	Date	Mode	Pol.
E1_18982_STD_F279	1995-03-02	D	VV
E1_19183_STD_F279	1995-03-16	D	VV
E1_19269_STD_F279	1995-03-22	D	VV
1993/1994			
E1_11410_STD_F279	1993-09-20	D	VV
E1_11453_STD_F279	1993-09-23	D	VV
E1_11502_STD_F171	1993-09-27	A	VV
E1_11639_STD_F279	1993-10-06	D	VV
E1_11682_STD_F279	1993-10-09	D	VV
E1_11725_STD_F279	1993-10-12	D	VV
E1_11731_STD_F171	1993-10-13	A	VV
E1_11774_STD_F171	1993-10-16	D	VV
E1_11868_STD_F279	1993-10-22	D	VV
E1_11911_STD_F279	1993-10-25	D	VV
E1_11954_STD_F279	1993-10-28	D	VV
E1_12003_STD_F171	1993-11-01	A	VV
E1_12140_STD_F279	1993-11-10	D	VV
E1_12183_STD_F279	1993-11-13	D	VV
E1_12226_STD_F279	1993-11-16	D	VV
E1_12232_STD_F171	1993-11-17	A	VV
E1_12369_STD_F279	1993-11-26	D	VV

ID	Date	Mode	Pol.
E1_12412_STD_F279	1993-11-29	D	VV
E1_12455_STD_F279	1993-12-02	D	VV
E1_12684_STD_F279	1993-12-18	D	VV
E1_12776_STD_F171	1993-12-25	A	VV
E1_12862_STD_F171	1993-12-31	A	VV
E1_13550_STD_F171	1994-02-17	A	VV
E1_14023_STD_F171	1994-03-22	A	VV
E1_14109_STD_F171	1994-03-28	A	VV
1992/1993			
E1_06263_STD_F171	1992-09-26	A	VV
E1_06306_STD_F171	1992-09-29	A	VV
E1_06357_STD_F279	1992-10-02	D	VV
E1_06400_STD_F279	1992-10-05	D	VV
E1_06443_STD_F279	1992-10-08	D	VV
E1_06492_STD_F171	1992-10-12	A	VV
E1_06629_STD_F279	1992-10-21	D	VV
E1_06672_STD_F279	1992-10-24	D	VV
E1_06715_STD_F279	1992-10-27	D	VV
E1_06858_STD_F279	1992-11-06	D	VV
E1_06901_STD_F279	1992-11-09	D	VV
E1_07130_STD_F279	1992-11-25	D	VV

ID	Date	Mode	Pol.
E1_07173_STD_F279	1992-11-28	D	VV
E1_07216_STD_F279	1992-12-01	D	VV
E1_07359_STD_F279	1992-12-11	D	VV
E1_07402_STD_F279	1992-12-14	D	VV
E1_07445_STD_F279	1992-12-17	D	VV
E1_07631_STD_F279	1992-12-30	D	VV
E1_07674_STD_F279	1993-01-02	D	VV
E1_07860_STD_F279	1993-01-15	D	VV
E1_07903_STD_F279	1993-01-18	D	VV
E1_07946_STD_F279	1993-01-21	D	VV
E1_08132_STD_F279	1993-02-03	D	VV
E1_08175_STD_F279	1993-02-06	D	VV
E1_08361_STD_F279	1993-02-19	D	VV
E1_08404_STD_F279	1993-02-22	D	VV
E1_08496_STD_F171	1993-03-01	D	VV
E1_08633_STD_F279	1993-03-10	D	VV
E1_08676_STD_F279	1993-03-13	D	VV
E1_08768_STD_F171	1993-03-20	A	VV

Table 3: RADARSAT 1 scenes used in this thesis. "Pol." stands for Polarization, "A" stands for the ascending mode, and "D" stands for the descending mode.

ID	Date	Mode	Pol.
2007/2008			
R1_62156_SWB_F276	2007-10-01	D	HH
R1_62213_SWB_F276	2007-10-05	D	HH
R1_62256_SWB_F276	2007-10-08	D	HH
R1_62356_SWB_F276	2007-10-15	D	HH
R1_62456_SWB_F276	2007-10-22	D	HH
R1_62499_SWB_F276	2007-10-25	D	HH
R1_62556_SWB_F276	2007-10-29	D	HH
R1_62599_SWB_F276	2007-11-01	D	HH
R1_62699_SWB_F276	2007-11-08	D	HH
R1_62799_SWB_F276	2007-11-15	D	HH
R1_62899_SWB_F276	2007-11-22	D	HH
R1_62942_SWB_F276	2007-11-25	D	HH
R1_63042_SWB_F276	2007-12-02	D	HH
R1_63185_SWB_F276	2007-12-12	D	HH
R1_63285_SWB_F276	2007-12-19	D	HH
R1_63428_SWB_F276	2007-12-29	D	HH
R1_63671_SWB_F276	2008-01-15	D	HH
R1_63828_SWB_F276	2008-01-26	D	HH

ID	Date	Mode	Pol.
R1_63928_SWB_F276	2008-02-02	D	HH
R1_64014_SWB_F276	2008-02-08	D	HH
R1_64114_SWB_F276	2008-02-15	D	HH
R1_64357_SWB_F276	2008-03-03	D	HH
R1_64457_SWB_F276	2008-03-10	D	HH
R1_64614_SWB_F276	2008-03-21	D	HH
2005/2006			
R1_51723_SWB_F276	2005-10-01	D	HH
R1_51966_SWB_F276	2005-10-18	D	HH
R1_52066_SWB_F276	2005-10-25	D	HH
R1_52309_SWB_F276	2005-11-11	D	HH
R1_52409_SWB_F276	2005-11-18	D	HH
R1_52509_SWB_F276	2005-11-25	D	HH
R1_52652_SWB_F276	2005-12-05	D	HH
R1_52995_SWB_F274	2005-12-29	D	HH
R1_53095_SWB_F276	2006-01-05	D	HH
R1_53338_SWB_F276	2006-01-22	D	HH
R1_53438_SWB_F276	2006-01-29	D	HH
R1_53681_SWB_F276	2006-02-15	D	HH
R1_53781_SWB_F276	2006-02-22	D	HH
R1_53981_SWB_F276	2006-03-08	D	HH

ID	Date	Mode	Pol.
R1_54024_SWB_F276	2006-03-11	D	HH
R1_54124_SWB_F276	2006-03-18	D	HH
2004/2005			
R1_46335_SWB_F283	2004-09-19	D	HH
R1_46578_SWB_F276	2004-10-06	D	HH
R1_46721_SWB_F276	2004-10-16	D	HH
R1_46821_SWB_F276	2004-10-23	D	HH
R1_46921_SWB_F276	2004-10-30	D	HH
R1_47064_SWB_F276	2004-11-09	D	HH
R1_47164_SWB_F276	2004-11-16	D	HH
R1_47264_SWB_F276	2004-11-23	D	HH
R1_47364_SWB_F276	2004-11-30	D	HH
R1_47464_SWB_F276	2004-12-07	D	HH
R1_47507_SWB_F276	2004-12-10	D	HH
R1_47607_SWB_F276	2004-12-17	D	HH
R1_47850_SWB_F276	2005-01-03	D	HH
R1_47950_SWB_F276	2005-01-10	D	HH
R1_48050_SWB_F276	2005-01-17	D	HH
R1_48193_SWB_F276	2005-01-27	D	HH
R1_48293_SWB_F276	2005-02-03	D	HH
R1_48536_SWB_F276	2005-02-20	D	HH

ID	Date	Mode	Pol.
R1_48636_SWB_F276	2005-02-27	D	HH
R1_48879_SWB_F276	2005-03-16	D	HH
R1_48979_SWB_F276	2005-03-23	D	HH
2003/2004			
R1_41190_SWB_F276	2003-09-25	D	HH
R1_41333_SWB_F276	2003-10-05	D	HH
R1_41390_SWB_F276	2003-10-09	D	HH
R1_41476_SWB_F276	2003-10-15	D	HH
R1_41490_SWB_F276	2003-10-16	D	HH
R1_41533_SWB_F276	2003-10-19	D	HH
R1_41576_SWB_F276	2003-10-22	D	HH
R1_41633_SWB_F276	2003-10-26	D	HH
R1_41776_SWB_F276	2003-11-05	D	HH
R1_41819_SWB_F275	2003-11-08	D	HH
R1_41876_SWB_F276	2003-11-12	D	HH
R1_42019_SWB_F276	2003-11-22	D	HH
R1_42119_SWB_F276	2003-11-29	D	HH
R1_42219_SWB_F276	2003-12-06	D	HH
R1_42362_SWB_F276	2003-12-16	D	HH
R1_42462_SWB_F276	2003-12-23	D	HH
R1_42562_SWB_F276	2003-12-30	D	HH

ID	Date	Mode	Pol.
R1_42662_SWB_F276	2004-01-06	D	HH
R1_42705_SWB_F276	2004-01-09	D	HH
R1_42762_SWB_F276	2004-01-13	D	HH
R1_43148_SWB_F276	2004-02-09	D	HH
R1_43391_SWB_F276	2004-02-26	D	HH
R1_43491_SWB_F276	2004-03-04	D	HH
R1_43734_SWB_F276	2004-03-21	D	HH
2002/2003			
R1_36088_SWB_F276	2002-10-03	D	HH
R1_36145_SWB_F276	2002-10-07	D	HH
R1_36188_SWB_F276	2002-10-10	D	HH
R1_36288_SWB_F276	2002-10-17	D	HH
R1_36331_SWB_F276	2002-10-20	D	HH
R1_36388_SWB_F276	2002-10-24	D	HH
R1_36431_SWB_F276	2002-10-27	D	HH
R1_36531_SWB_F276	2002-11-03	D	HH
R1_36631_SWB_F276	2002-11-10	D	HH
R1_36674_SWB_F276	2002-11-13	D	HH
R1_36731_SWB_F276	2002-11-17	D	HH
R1_36774_SWB_F276	2002-11-20	D	HH
R1_37260_SWB_F275	2002-12-24	D	HH

ID	Date	Mode	Pol.
R1_37274_SWB_F276	2002-12-25	D	HH
R1_37360_SWB_F275	2002-12-31	D	HH
R1_37417_SWB_F276	2003-01-04	D	HH
R1_37517_SWB_F276	2003-01-11	D	HH
R1_37560_SWB_F276	2003-01-14	D	HH
R1_37617_SWB_F276	2003-01-18	D	HH
R1_37660_SWB_F276	2003-01-21	D	HH
R1_37703_SWB_F275	2003-01-24	D	HH
R1_37760_SWB_F276	2003-01-28	D	HH
R1_37860_SWB_F276	2003-02-04	D	HH
R1_37903_SWB_F276	2003-02-07	D	HH
R1_37960_SWB_F276	2003-02-11	D	HH
R1_38046_SWB_F275	2003-02-17	D	HH
R1_38103_SWB_F276	2003-02-21	D	HH
R1_38203_SWB_F276	2003-02-28	D	HH
R1_38246_SWB_F276	2003-03-03	D	HH
R1_38303_SWB_F276	2003-03-07	D	HH
R1_38389_SWB_F275	2003-03-13	D	HH
R1_38446_SWB_F276	2003-03-17	D	HH
2001/2002			
R1_30878_SWB_F171	2001-10-04	A	HH

ID	Date	Mode	Pol.
R1_30978_SWB_F172	2001-10-11	A	HH
R1_31078_SWB_F172	2001-10-15	D	HH
R1_31143_SWB_F276	2001-10-22	D	HH
R1_31178_SWB_F175	2001-10-25	A	HH
R1_31221_SWB_F171	2001-10-28	A	HH
R1_31286_SWB_F276	2001-11-01	D	HH
R1_31386_SWB_F276	2001-11-08	D	HH
R1_31421_SWB_F172	2001-11-11	A	HH
R1_31464_SWB_F171	2001-11-14	A	HH
R1_31486_SWB_F276	2001-11-15	D	HH
R1_31564_SWB_F168	2001-11-21	A	HH
R1_31629_SWB_F276	2001-11-25	D	HH
R1_31729_SWB_F278	2001-12-02	D	HH
R1_31764_SWB_F172	2001-12-05	A	HH
R1_31807_SWB_F171	2001-12-08	A	HH
R1_31829_SWB_F276	2001-12-09	D	HH
R1_31864_SWA_F171	2001-12-12	A	HH
R1_31907_SWB_F171	2001-12-15	A	HH
R1_31972_SWB_F276	2001-12-19	D	HH
R1_32007_SWB_F173	2001-12-22	A	HH
R1_32072_SWB_F276	2001-12-26	D	HH

ID	Date	Mode	Pol.
R1_32115_SWB_F275	2001-12-29	D	HH
R1_32150_SWB_F171	2002-01-01	A	HH
R1_32172_SWB_F276	2002-01-02	D	HH
R1_32215_SWB_F276	2002-01-05	D	HH
R1_32250_SWB_F167	2002-01-08	A	HH
R1_32315_SWB_F276	2002-01-12	D	HH
R1_32415_SWB_F276	2002-01-19	D	HH
R1_32458_SWB_F275	2002-01-22	D	HH
R1_32493_SWB_F174	2002-01-25	A	HH
R1_32515_SWB_F276	2002-01-26	D	HH
R1_32558_SWB_F276	2002-01-29	D	HH
R1_32593_SWB_F174	2002-02-01	A	HH
R1_32658_SWB_F276	2002-02-05	D	HH
R1_32715_SWB_F276	2002-02-09	D	HH
R1_32758_SWB_F277	2002-02-12	D	HH
R1_32801_SWB_F275	2002-02-15	D	HH
R1_32836_SWB_F171	2002-02-18	D	HH
R1_32858_SWB_F276	2002-02-19	D	HH
R1_32901_SWB_F276	2002-02-22	D	HH
R1_32936_SWB_F174	2002-02-25	A	HH
R1_33101_SWB_F276	2002-03-08	D	HH

ID	Date	Mode	Pol.
R1_33136_SWB_F173	2002-03-11	A	HH
R1_33179_SWB_F172	2002-03-14	A	HH
2000/2001			
R1_25555_SWB_F276	2000-09-26	D	HH
R1_25655_SWB_F276	2000-10-03	D	HH
R1_25698_SWB_F276	2000-10-06	D	HH
R1_25798_SWB_F276	2000-10-13	D	HH
R1_25941_SWB_F276	2000-10-23	D	HH
R1_26284_SWB_F276	2000-11-16	D	HH
R1_26384_SWB_F276	2000-11-23	D	HH
R1_26484_SWB_F276	2000-11-30	D	HH
R1_26627_SWB_F276	2000-12-10	D	HH
R1_26727_SWB_F276	2000-12-17	D	HH
R1_26827_SWB_F276	2000-12-24	D	HH
R1_26970_SWB_F276	2001-01-03	D	HH
R1_27070_SWB_F276	2001-01-10	D	HH
R1_27170_SWB_F276	2001-01-17	D	HH
R1_27313_SWB_F275	2001-01-27	D	HH
R1_27370_SWB_F275	2001-01-31	D	HH
R1_27413_SWB_F276	2001-02-03	D	HH
R1_27513_SWB_F276	2001-02-10	D	HH

ID	Date	Mode	Pol.
R1_27613_SWB_F277	2001-02-17	D	HH
R1_27748_SWB_F168	2001-02-27	A	HH
R1_27848_SWA_F169	2001-03-06	A	HH
R1_27948_SWB_F175	2001-03-13	A	HH
1999/2000			
R1_20410_SWB_F277	1999-10-02	D	HH
R1_20467_SWB_F284	1999-10-06	D	HH
R1_20610_SWB_F276	1999-10-16	D	HH
R1_20653_SWB_F277	1999-10-19	D	HH
R1_20753_SWB_F275	1999-10-26	D	HH
R1_20853_SWB_F276	1999-11-02	D	HH
R1_20896_SWB_F275	1999-11-05	D	HH
R1_21053_SWB_F279	1999-11-16	D	HH
R1_21096_SWB_F275	1999-11-19	D	HH
R1_21153_SWB_F284	1999-11-23	D	HH
R1_21239_SWB_F275	1999-11-29	D	HH
R1_21296_SWB_F279	1999-12-03	D	HH
R1_21339_SWB_F275	1999-12-06	D	HH
R1_21396_SWB_F280	1999-12-10	D	HH
R1_21496_SWB_F284	1999-12-17	D	HH
R1_21582_SWB_F275	1999-12-23	D	HH

ID	Date	Mode	Pol.
R1_21639_SWB_F276	1999-12-27	D	HH
R1_21682_SWB_F275	1999-12-30	D	HH
R1_21739_SWB_F280	2000-01-03	D	HH
R1_21839_SWB_F284	2000-01-10	D	HH
R1_21982_SWB_F276	2000-01-20	D	HH
R1_22025_SWB_F275	2000-01-23	D	HH
R1_22082_SWB_F280	2000-01-27	D	HH
R1_22125_SWB_F276	2000-01-30	D	HH
R1_22182_SWB_F284	2000-02-03	D	HH
R1_22268_SWB_F276	2000-02-09	D	HH
R1_22325_SWB_F276	2000-02-13	D	HH
R1_22425_SWB_F279	2000-02-20	D	HH
R1_22568_SWB_F276	2000-03-01	D	HH
R1_22811_SWB_F276	2000-03-18	D	HH

A.2 All the maps created using TempCNN

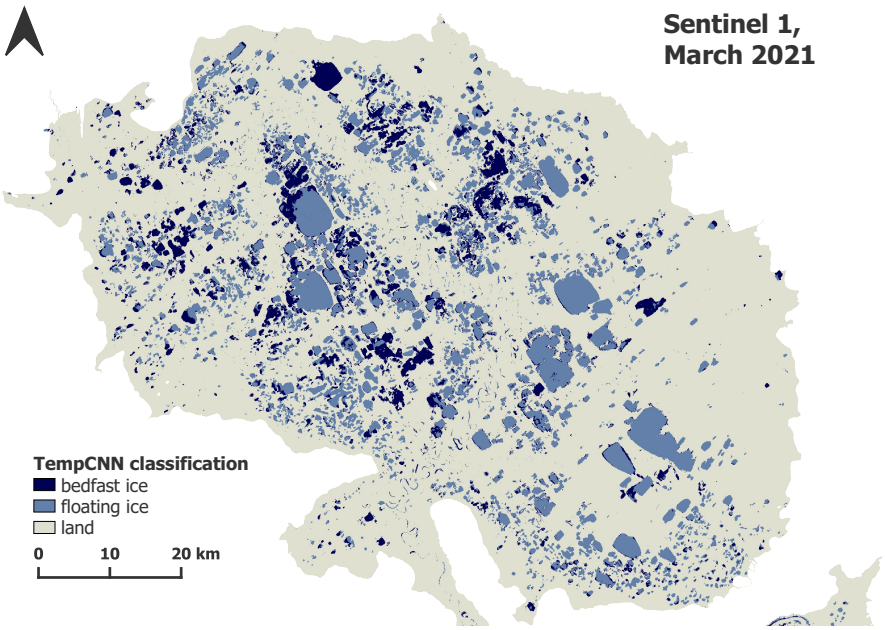


Figure A.1: TempCNN classication output for Sentinel 1, March 2021, OCF, Yukon Canada.

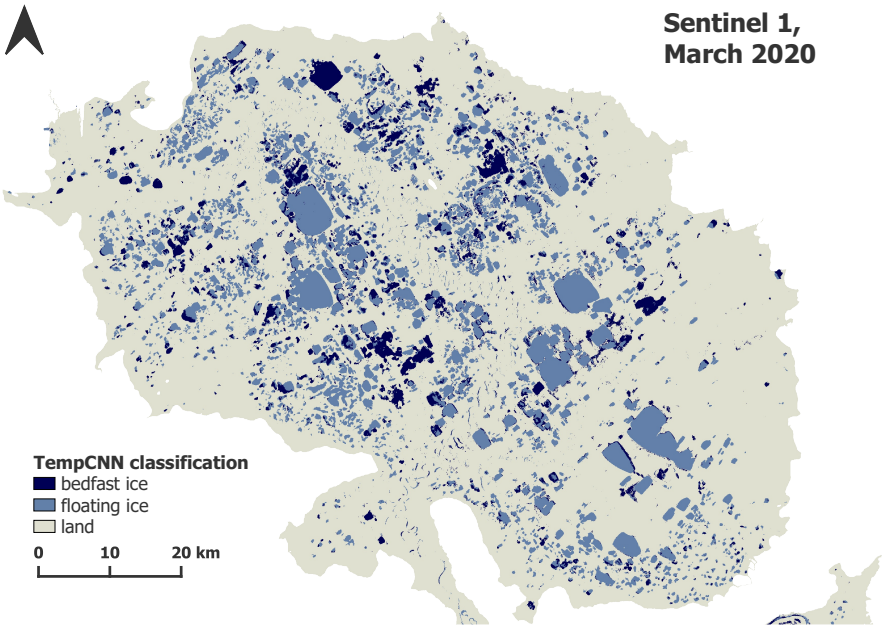


Figure A.2: TempCNN classication output for Sentinel 1, March 2020, OCF, Yukon Canada.

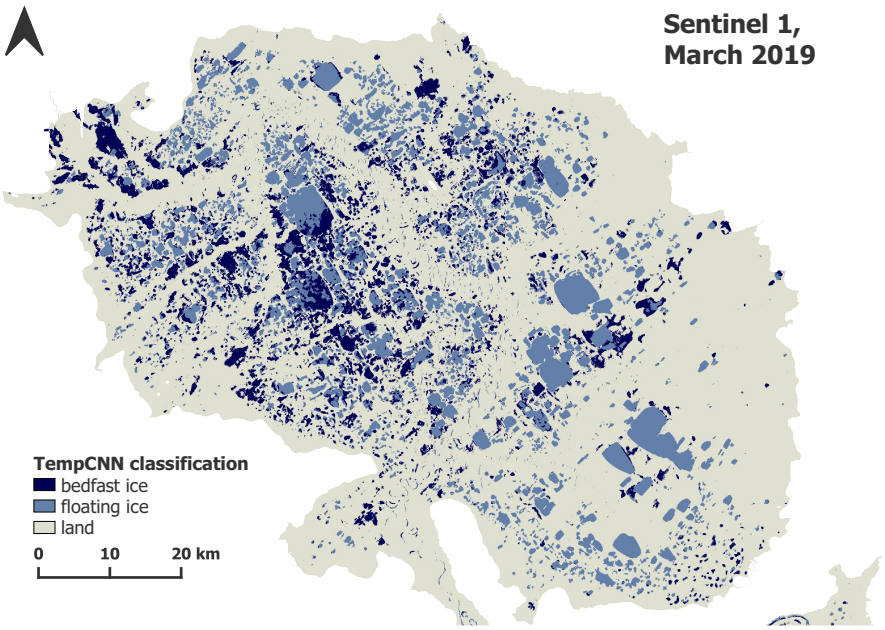


Figure A.3: TempCNN classication output for Sentinel 1, March 2019, OCF, Yukon Canada.

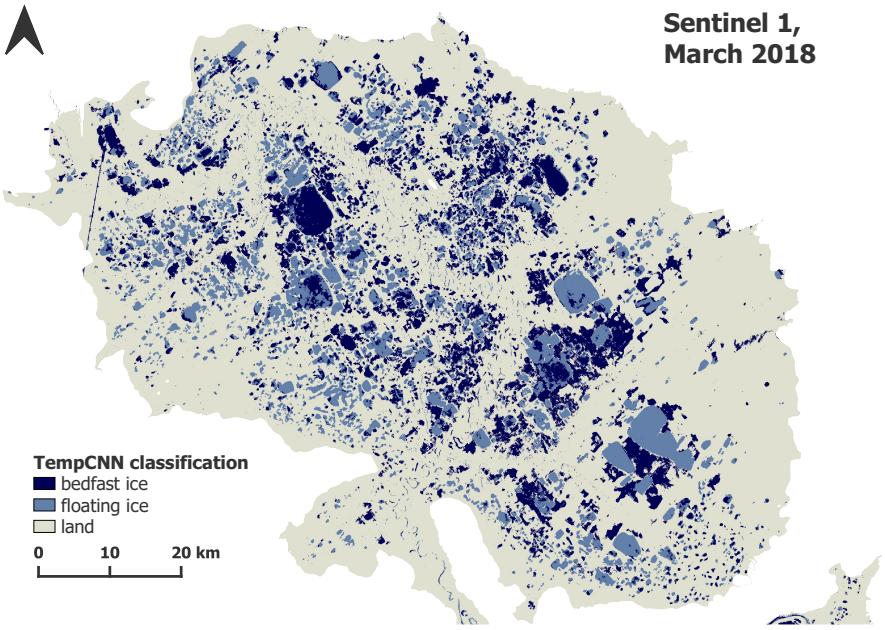


Figure A.4: TempCNN classication output for Sentinel 1, March 2018, OCF, Yukon Canada.

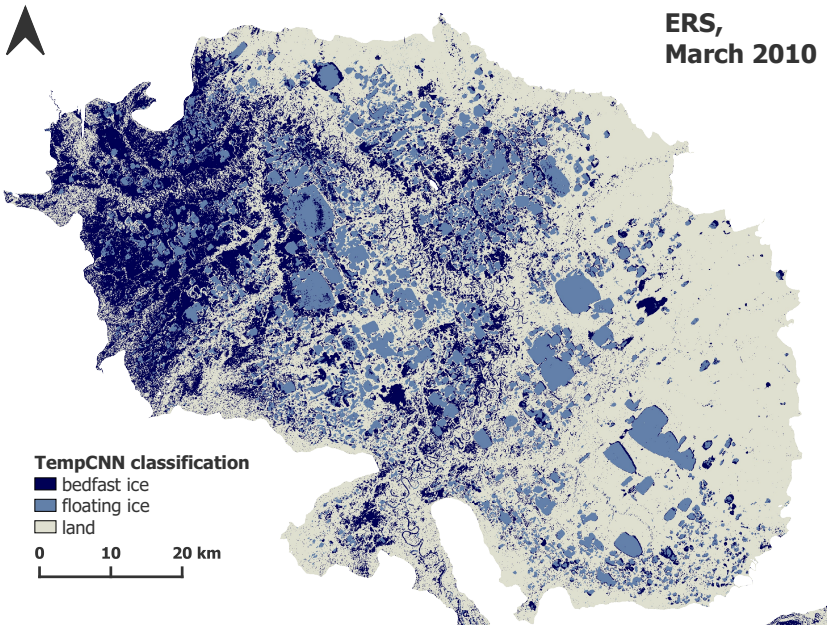


Figure A.5: TempCNN classication output for ERS, March 2010, OCF, Yukon Canada.

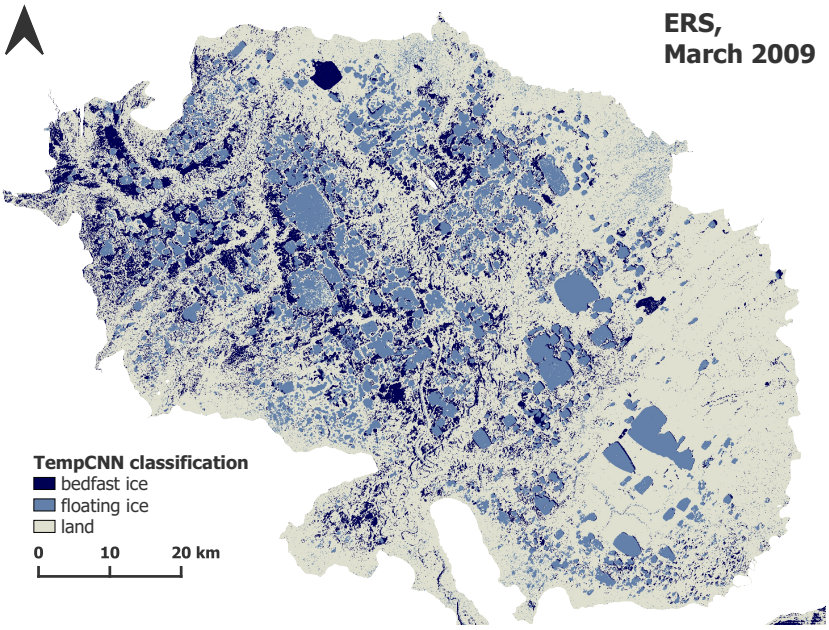


Figure A.6: TempCNN classication output for ERS, March 2009, OCF, Yukon Canada.

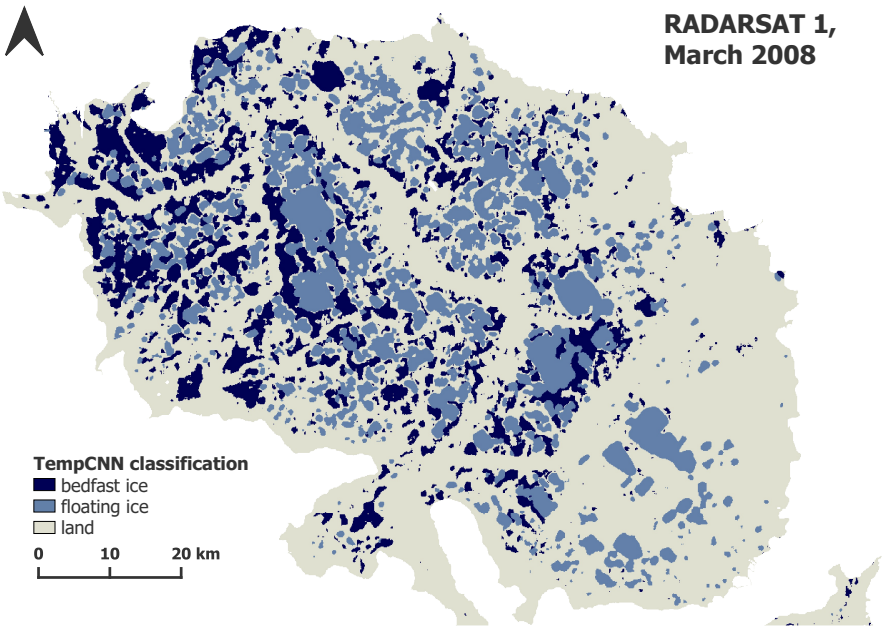


Figure A.7: TempCNN classication output for RADARSAT 1, March 2008, OCF, Yukon Canada.

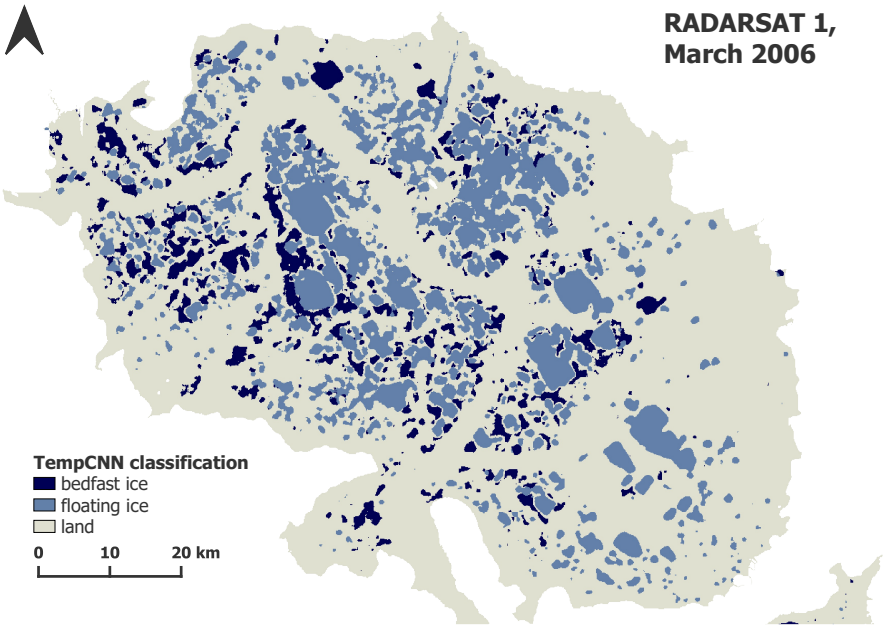


Figure A.8: TempCNN classication output for RADARSAT 1, March 2006, OCF, Yukon Canada.

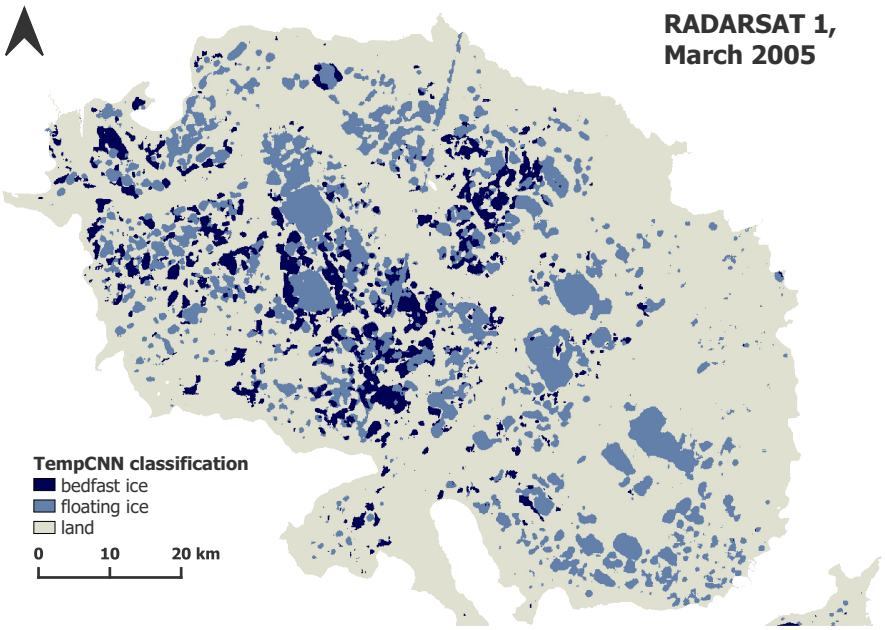


Figure A.9: TempCNN classication output for RADARSAT 1, March 2005, OCF, Yukon Canada.

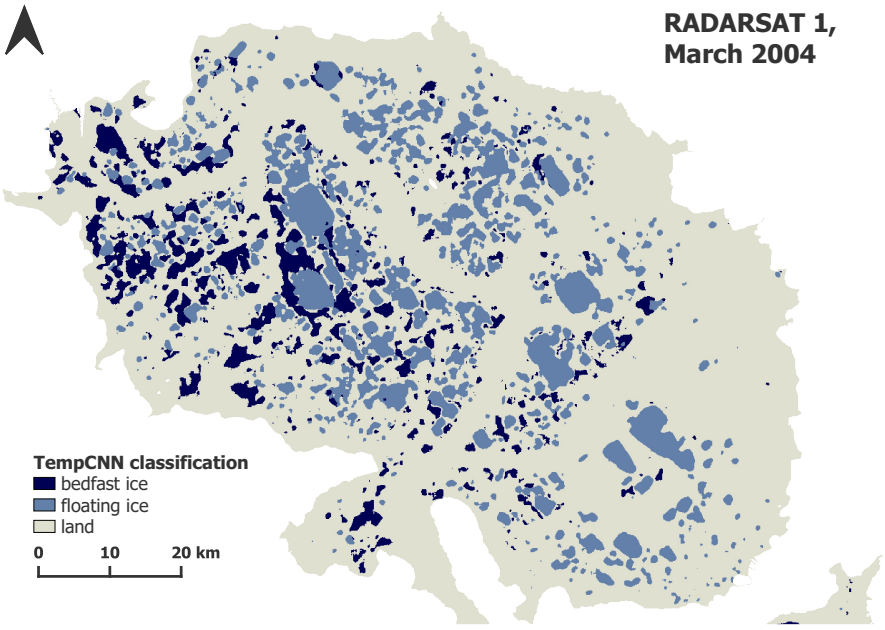


Figure A.10: TempCNN classication output for RADARSAT 1, March 2004, OCF, Yukon Canada.

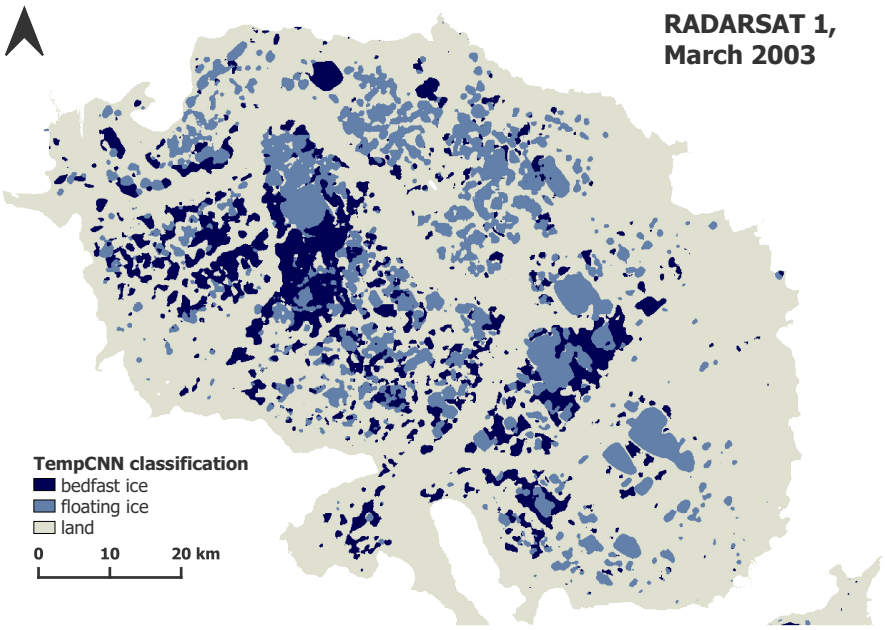


Figure A.11: TempCNN classication output for RADARSAT 1, March 2003, OCF, Yukon Canada.

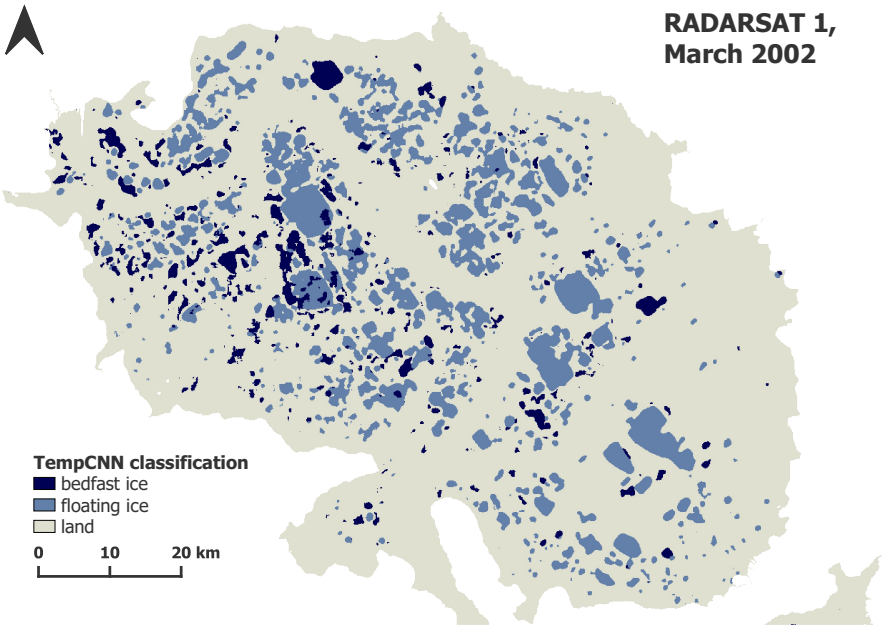


Figure A.12: TempCNN classication output for RADARSAT 1, March 2002, OCF, Yukon Canada.

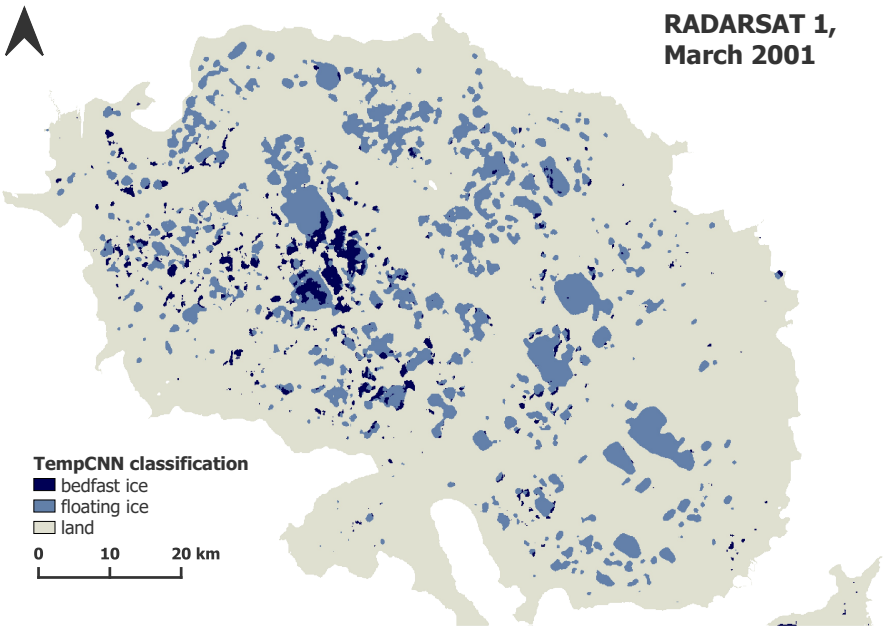


Figure A.13: TempCNN classication output for RADARSAT 1, March 2001, OCF, Yukon Canada.

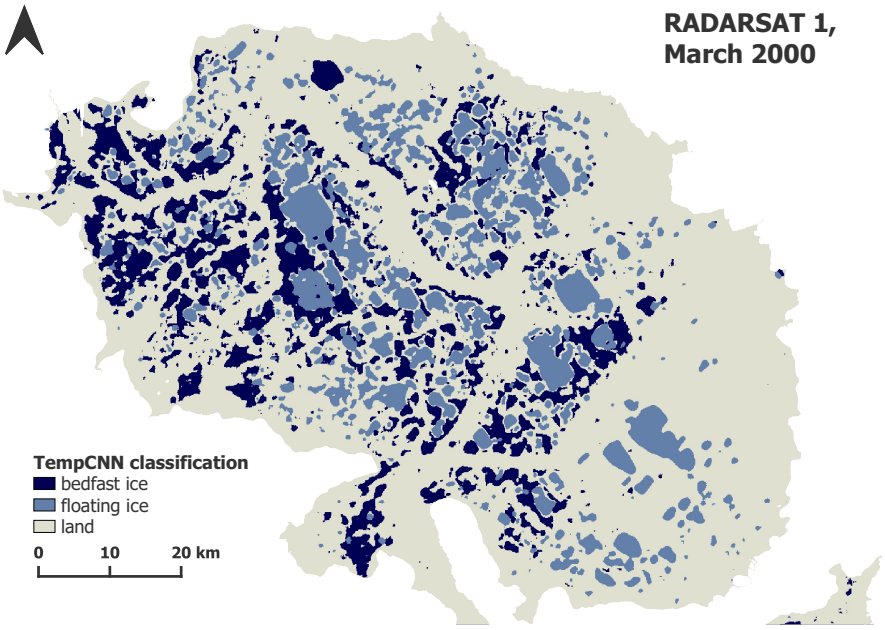


Figure A.14: TempCNN classication output for RADARSAT 1, March 2000, OCF, Yukon Canada.

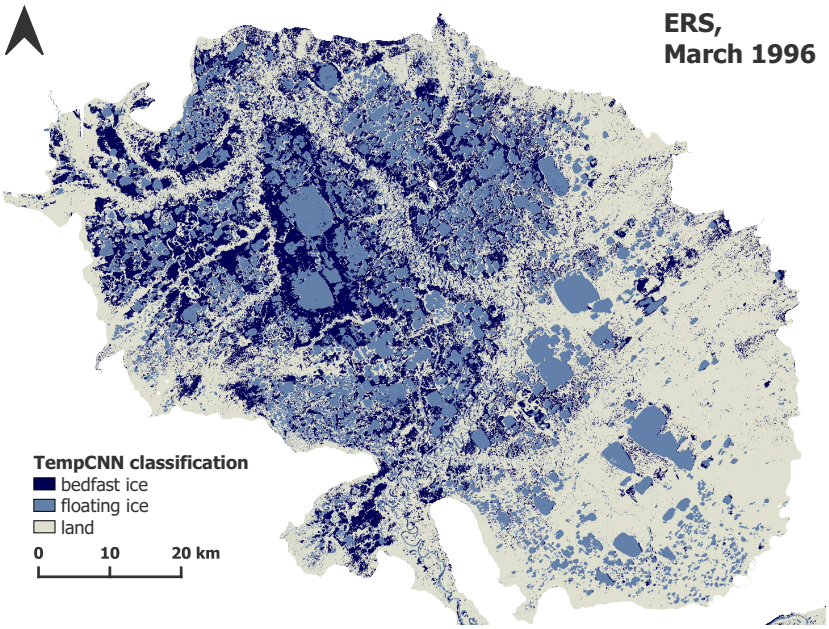


Figure A.15: TempCNN classication output for ERS, March 1996, OCF, Yukon Canada.

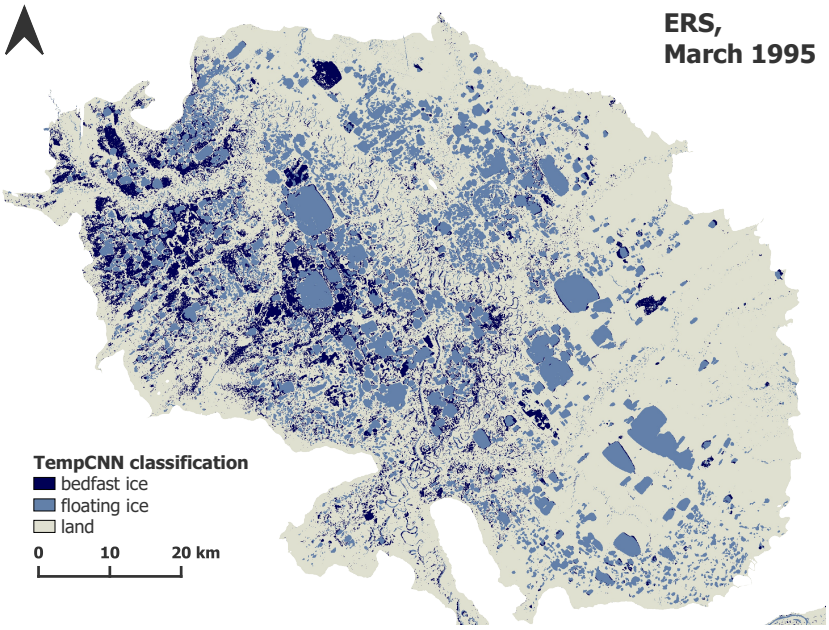


Figure A.16: TempCNN classication output for ERS, March 1995, OCF, Yukon Canada.

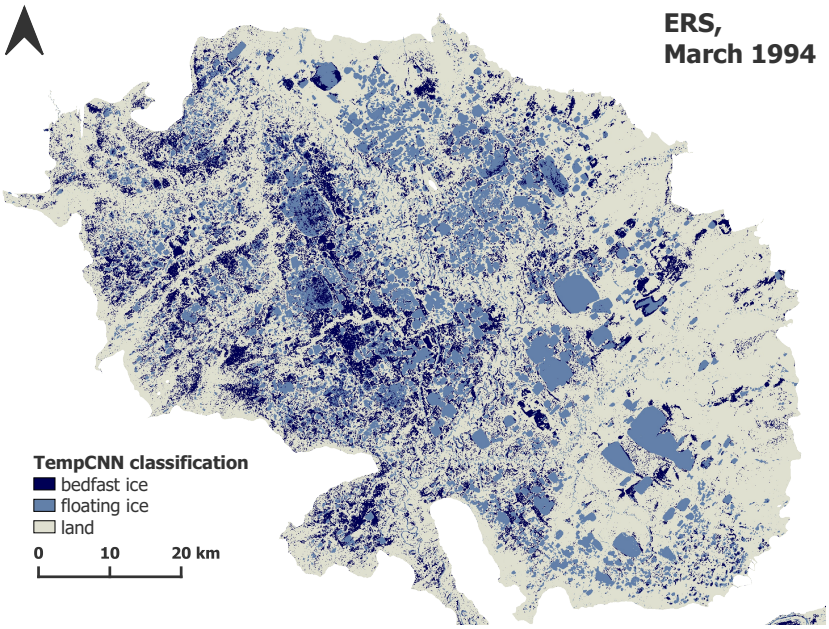


Figure A.17: TempCNN classication output for ERS, March 1994, OCF, Yukon Canada.

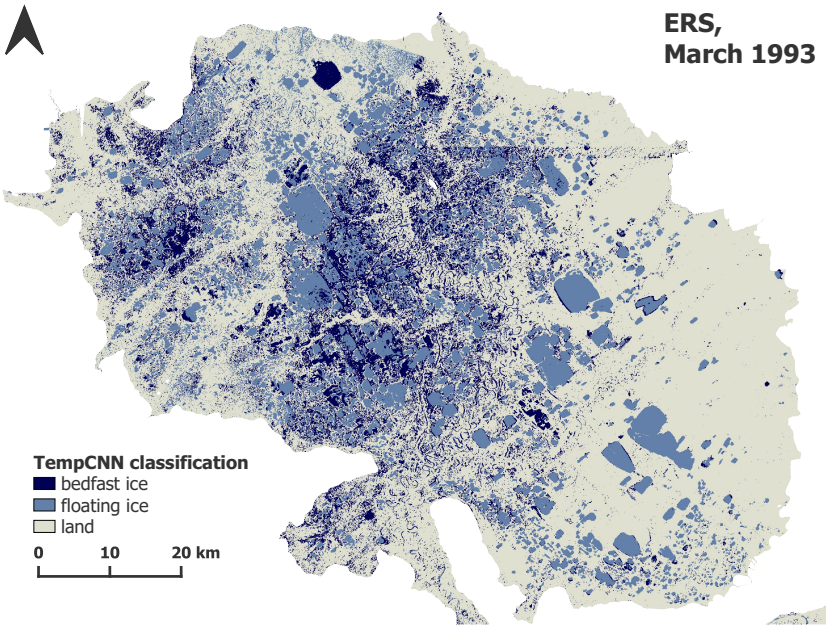


Figure A.18: TempCNN classication output for ERS, March 1993, OCF, Yukon Canada.